

Computational Configurational Mechanics

vom Fachbereich Maschinenbau und Verfahrenstechnik
der Technischen Universität Kaiserslautern
zur Verleihung des akademischen Grades
Doktor-Ingenieur (Dr.-Ing.)
genehmigte Dissertation

von Dipl.-Ing. Ralf Denzer
aus Kaiserslautern

| | |
|----------------|--|
| Hauptreferent: | Prof. Dr.-Ing. Paul Steinmann |
| Korreferenten: | Prof. Dr. rer. nat. Braun Prof. Dr.-Ing. Dietmar Groß |
| Vorsitzender: | Prof. Dr.-Ing. Gerd Maurer |
| Dekan: | Prof. Dr.-Ing. Paul Steinmann |

| | |
|-------------------------|------------------|
| Tag der Einreichung: | 12. Januar 2005 |
| Tag der mündl. Prüfung: | 22. Februar 2005 |

Kaiserslautern, Februar 2006
D 386

Vorwort

Die vorliegende Arbeit entstand während meiner Tätigkeit als wissenschaftlicher Mitarbeiter am Lehrstuhl für Technische Mechanik (LTM) an der Technischen Universität Kaiserslautern. Die finanzielle Unterstützung seitens der Deutschen Forschungsgemeinschaft (DFG) im Rahmen des Forschungsprojektes STE 544/14-1 mit dem Titel *‘Theorie und Numerik materieller Kräfte in der Defektmechanik’* ermöglichte erst diese Arbeit.

Besonders möchte ich meinem akademischen Lehrer Prof. Dr.-Ing. Paul Steinmann für die Anregung zu dieser Arbeit, seine intensive und konsequente wissenschaftliche Förderung sowie die Übernahme des Hauptreferates danken. Herrn Prof. Dr.-Ing. Paul Steinmann verdanke ich meine Ausbildung auf den Feldern der Kontinuumsmechanik und der numerische Mechanik. Weiterhin danke ich den Herren Prof. Dr. rer. nat. Braun und Prof. Dr.-Ing. Dietmar Groß für zahlreiche wertvolle Anregungen und Hinweise sowie insbesondere für die Übernahme der Korreferate sowie Herrn Prof. Dr.-Ing. Gerd Maurer für den Vorsitz.

Allen Mitarbeitern des LTM danke ich für die angenehme und freundliche Arbeitsatmosphäre und für die freundliche Zusammenarbeit. Besonders möchte ich Frau Jeblick für ihre Unterstützung bei allen Problemen des universitären Lebens danken. Nicht vergessen möchte ich Dr.-Ing. Franz Josef Barth, Dr.-Ing. Tina Liebe, JP Dr.-Ing. Ellen Kuhl, Dr.-Ing. Andreas Menzel, Dipl.-Ing. Jürgen Glaser und Dr.-Ing. Julia Mergheim für zahlreiche Anmerkungen zu dieser Arbeit.

Kaiserslautern, Februar 2006

Ralf Denzer

Zusammenfassung

Diese Arbeit stellt einen Beitrag zur Theorie und Numerik materieller Kräfte der Kontinuumsmechanik dar. Im Gegensatz zu physikalischen Kräften wirken materielle Kräfte in der sogenannten materiellen Mannigfaltigkeit bzw. im materiellen Raum. Dabei repräsentieren Sie die Tendenz von Defekten wie beispielsweise Risse oder Einschlüsse sich relativ zu dem sie umgebenden Material zu bewegen. Materielle Kräfte eignen sich somit insbesondere für eine Bewertung von Defekten und den oftmals damit verbundenen Singularitäten in festen Körpern.

Konzeptionell untersucht die übliche räumliche Formulierung der Kontinuumsmechanik die Antwort auf Variationen räumlicher Plazierungen ‘physikalischer Partikel’ gegenüber dem umgebenden Raum. Demgegenüber wird in der materiellen Formulierung der Kontinuumsmechanik die Antwort auf Variationen materieller Plazierungen ‘physikalischer Partikel’ gegenüber dem umgebenden Material betrachtet. Die erste Betrachtungsweise führt dabei auf die üblichen räumlichen (newtonschen, mechanischen) Kräfte, die ‘physikalische Partikel’ durch den umgebenden Raum treiben, während die letztere Betrachtungsweise auf materielle (eshelbysche, Konfigurations-) Kräfte führt, die ‘physikalische Partikel’ durch das umgebende Material treiben.

Die Betrachtung von materiellen Kräften geht auf die Arbeiten von Eshelby [27, 29] zurück, der als erster Kräfte untersuchte, die auf Defekte wirken. Die in der materiellen Impulsbilanz auftauchenden materiellen Spannungen werden daher oftmals auch als Eshelby Spannungen bezeichnet. Basierend auf dem Konzept der materiellen Kräfte stellt die Analyse von verschiedenen Defekten, wie z.B. Rissen, Versetzungen, Einschlüsse, Phasengrenzen und ähnlichem, hinsichtlich ihrer Tendenz, sich gegenüber dem umgebenden Material zu bewegen, einen aktiven Zweig der Kontinuumsmechanik und -physik dar.

Die theoretische Seite der Arbeit umfasst die Aufarbeitung und Formulierung der materiellen Bilanzaussagen für konservative und insbesondere nichtkonservative Problemstellungen, die sich aus der Betrachtung des inversen Deformationsproblems ergeben. Basierend auf diesen theoretischen Arbeiten sowie aufgrund der Verwendung der Finite Element Methode zur Lösung des direkten Deformationsproblems bietet sich eine Galerkin Diskretisierung der schwachen Form der materiellen Bilanzaussagen an. Hieraus resultiert eine Finite Element Methode, die Methode der Materiellen Kräfte, deren Knotengrößen diskreten materiellen Einzelkräften entsprechen. Ein Hauptziel auf der numerischen Seite war es daher, die Implementierung verschiedener konservativer und insbesondere nicht-

konservativer Problemstellungen zu realisieren und anhand unterschiedlicher Beispiele die Kinetik von Defekten numerisch zu untersuchen.

Als konservative Problemstellung wird die geometrisch nichtlineare Hyperelastizität diskutiert. Hierbei zeigt sich eine Dualität zwischen der materiellen Formulierung der Kontinuumsmechanik und der üblichen räumlichen Formulierung. Es zeigt sich, daß das in der Bruchmechanik häufig verwendete J -Integral, das zur Bewertung von Rissen herangezogen wird, einer materiellen Einzelkraft entspricht, die an der Reißspitze angreift und sozusagen den Ri durch das Material treiben mchte. Gngige numerische Verfahren zur Berechnung des J -Integralwertes, wie z.B. Gebietsintegrale, lassen sich im Rahmen der Theorie Materieller Krfte somit als Gleichgewichtsbetrachtungen von materiellen Krften in der materiellen Konfiguration interpretieren. Als Modellbeispiele wurden Risse in hyperelastischen Materialien untersucht. Es wurde hierbei auch die Spezialisierung auf den geometrisch linearen Fall durchgefhrt, um einen Vergleich mit bereits bekannten Ergebnissen aus der geometrisch linearen Fliebruchmechanik (Ramberg-Osgood Stoffgesetz) durchzufhren. Anhand von numerischen Simulationen konnte eine gute bereinstimmung zwischen der Methode der materiellen Krften und den klassischen Verfahren zur Berechnung des J -Integralwertes dargestellt werden. Im geometrisch nichtlinearen Fall konnte weiterhin gezeigt werden, da die materielle Einzelkraft, die an einer Reißspitze wirkt, ein gut geeignetes Riabknickkriterium ist.

Fr nichtkonservative Systeme wurden folgende Problemstellungen diskutiert:

- gekoppelte Problemstellungen der Thermomechanik
- gekoppelte Problemstellungen der Kontinuumsschdigungsmechanik
- geometrisch nichtlineare Plastomechanik
- geometrisch lineare Einkristallplastizitt
- geometrisch lineare von Mises Plastizitt

In all diesen Problemstellungen treten lokale nderungen von Inhomogenitten in Materialien auf. Diese knnen auf elegante Weise mit zustzlich auftretenden materiellen Volumenkrften charakterisiert werden. Verursacht werden diese durch inhomogene Feldverlufe in den zustzlichen Zustandsvariablen (z.B. Temperatur, Schdigungsparameter oder interne plastische Variablen). Eine der numerischen Hauptziele dieser Arbeit war nun, diese Gradienten numerisch zu berechnen um damit die materiellen Volumenkrfte ermitteln zu knnen.

Hierzu wurden im wesentlichen zwei Lsungsstrategien verfolgt. Erstens wurde die entsprechende Zustandsvariable als zustzlicher Freiheitsgrad auf ‘Knoten-Ebene’ in der FE-Diskretisierung eingefhrt (Thermomechanik, Kontinuumsschdigungsmechanik und Einkristallplastizitt). Dabei mssen in Falle der Kontinuumsschdigungsmechanik und der Einkristallplastizitt die Kuhn-Tucker-Bedingungen auf ‘Knoten-Ebene’ erfllt werden,

was durch die Verwendung eines ‘active set search’-Algorithmus gelöst wurde. Nach der numerischen Lösung der Problemstellung können die Gradienten durch Standardmethoden der FE berechnet werden. Im Rahmen der zweiten Lösungsstrategie wurden die Zustandsvariablen klassisch als interne Variablen auf ‘Integrationspunkt-Ebene’ eingeführt (Einkristallplastizität und von Mises Plastizität) und dann mit einer L_2 -Projektion auf die Knoten-Ebene projiziert. Somit kann die Berechnung der Gradienten wieder mit Standardmethoden erfolgen. Der Vorteil dieser Methode ist der geringere numerische Aufwand, da die Kuhn-Tucker-Bedingungen nur lokal auf ‘Integrationspunkt-Ebene’ erfüllt werden müssen.

Anhand numerischer Beispiele wurde die Effizienz und die Zuverlässigkeit der entwickelten Methoden aufgezeigt. Insbesondere ist es hiermit möglich, materielle Kräfte für den Fall nichtkonservativer, d.h. dissipativer Reißprobleme oder auch Problemstellungen mit Einschlüssen in dissipativer Materialien zu berechnen.

Contents

| | |
|--|-----------|
| Zusammenfassung | 1 |
| 1 Introduction | 9 |
| 2 Hyperelasticity | 15 |
| 2.1 Duality in kinematics | 15 |
| 2.1.1 Spatial motion problem | 15 |
| 2.1.2 Material motion problem | 16 |
| 2.1.3 Spatial and material motion problem | 17 |
| 2.2 Duality in balance of momentum | 17 |
| 2.2.1 Spatial motion problem | 17 |
| 2.2.2 Material motion problem | 18 |
| 2.3 J -Integral from equilibrium of material forces | 20 |
| 2.4 Virtual work and discretization | 21 |
| 2.4.1 Spatial motion problem | 21 |
| 2.4.2 Material motion problem | 23 |
| 2.4.3 Material Force Method for J -integral evaluation | 25 |
| 2.5 The geometrically linear case | 27 |
| 2.6 Examples | 28 |
| 2.6.1 Crack in a Ramberg-Osgood material | 28 |
| 2.6.2 Single Edged Tension specimen | 35 |
| 2.6.3 Crack kinking | 38 |
| 3 Thermo-Hyperelasticity | 45 |
| 3.1 Kinematics | 45 |
| 3.1.1 Spatial motion problem | 45 |
| 3.1.2 Material motion problem | 46 |
| 3.1.3 Spatial vs. material motion kinematics | 47 |
| 3.1.4 Spatial motion problem | 47 |
| 3.1.5 Material motion problem | 48 |
| 3.1.6 Spatial vs. material quantities | 49 |
| 3.2 Weak form | 49 |

| | | |
|----------|---|------------|
| 3.2.1 | Spatial motion problem | 50 |
| 3.2.2 | Material motion problem | 51 |
| 3.2.3 | Spatial vs. material test functions | 52 |
| 3.2.4 | Spatial and material forces | 52 |
| 3.2.5 | Material Force Method | 52 |
| 3.3 | Discretization | 53 |
| 3.3.1 | Spatial motion problem | 54 |
| 3.3.2 | Material motion problem | 55 |
| 3.3.3 | Adiabatic thermo-hyperelasticity | 57 |
| 3.4 | Examples | 57 |
| 3.4.1 | Bi-material bar | 59 |
| 3.4.2 | Specimen with crack | 60 |
| 4 | Hyperelasticity Coupled with Damage | 65 |
| 4.1 | Hyperelasticity coupled to isotropic damage | 65 |
| 4.1.1 | Spatial motion problem | 65 |
| 4.1.2 | Material motion problem | 67 |
| 4.1.3 | Spatial versus material motion problem | 67 |
| 4.2 | Weak Form | 68 |
| 4.2.1 | Spatial motion problem | 68 |
| 4.2.2 | Material motion problem | 69 |
| 4.3 | Discretization | 70 |
| 4.3.1 | Spatial motion problem | 70 |
| 4.3.2 | Material motion problem | 71 |
| 4.3.3 | Discretized format of J-integral: Material Force Method | 72 |
| 4.4 | Numerical examples | 73 |
| 4.4.1 | Specimen with elliptic hole | 73 |
| 4.4.2 | Specimen with center crack | 79 |
| 4.4.3 | MBL-specimen | 80 |
| 5 | Plasticity | 83 |
| 5.1 | Kinematics | 83 |
| 5.2 | Material motion balance of momentum | 84 |
| 5.3 | Single Crystal Plasticity | 86 |
| 5.3.1 | Essential kinematics of crystal-plasticity | 86 |
| 5.3.2 | Standard dissipative materials | 87 |
| 5.3.3 | Numerical solution strategies | 88 |
| 5.3.4 | Examples | 90 |
| 5.4 | Von Mises plasticity | 102 |
| 6 | Outlook | 111 |

| | | |
|----------|--|------------|
| A | Notation | 113 |
| B | Ramberg-Osgood Material – Linearization | 115 |
| C | Thermo-Hyperelasticity – Linearization | 119 |
| D | Single Crystal Plasticity – Numerical Solution Strategies | 121 |
| | D.1 Node point based approach | 121 |
| | D.2 Integration point based approach | 123 |

Chapter 1

Introduction

In contrast to the spatial motion setting, the material motion setting of continuum mechanics is concerned with the response to variations of material placements of particles with respect to the ambient material. The material motion point of view is thus extremely prominent when dealing with defect mechanics to which it has originally been introduced by Eshelby [27, 28] more than half a century ago. Its primary unknown, the material deformation map is governed by the material motion balance of momentum, i.e. the balance of material forces on the material manifold in the sense of Eshelby.

Material (configurational) forces are concerned with the response to variations of material placements of 'physical particles' with respect to the ambient material. Opposed to that, the common spatial (mechanical) forces in the sense of Newton are considered as the response to variations of spatial placements of 'physical particles' with respect to the ambient space. Material forces as advocated by Maugin [59, 60] are especially suited for the assessment of general defects as inhomogeneities, interfaces, dislocations and cracks, where the material forces are directly related to the classical J -Integral in fracture mechanics, see also Gross & Seelig [31]. Another classical example of a material — or rather configurational — force is emblemized by the celebrated Peach–Koehler force, see e.g. the discussion in Steinmann [98].

Classically, the assessment of hyperelastic fracture mechanics problems is based on the evaluation of the J -integral, see Cherepanov [16] and Rice [80]. Thereby, the J -integral basically integrates the normal projection of the so-called Eshelby stress over a surface/line enclosing the crack tip. For hyperelastic problems without material inhomogeneities, the J -integral possesses the computationally attractive property of integration-path-independence. Nevertheless the approach of the J -integral possesses some possible drawbacks, e.g., the additional definition of an integration surface/line or the necessary projection of the Eshelby stress from the quadrature points to the integration surface/line. This obviously demands non-standard Finite Element data structures, see Shih & Needleman [86, 87]. Moreover, the J -integral is essentially restricted to fracture mechanics problems. An assessment of general defects in structures, as inhomogeneities, dislocations or interfaces is not possible.

We therefore aim for a theoretical and computational set-up which circumvents the difficulties mentioned above. To this end, we consider the formulation of the geometrically nonlinear balance equations of continuum mechanics on the material manifold. Our developments are based heavily on the exposition of the continuum mechanics of inhomogeneities as comprehensively outlined by Maugin [56, 58] and Gurtin [32] or Kienzler & Herrmann [38]. Thereby, the essential ingredient is the notion of the so-called Eshelby stresses and the material (or rather configurational) forces in the spirit of Eshelby, that are opposed to the standard spatial forces. The new approach then consists in a straightforward Galerkin discretization of the corresponding balance of (pseudo) momentum equation proposed by Steinmann et al. [99, 95]. Thereby it turns out that the resulting scheme resembles approaches like e.g. those advocated by Braun [12] or Li & Needleman [48]. The resulting node point quantities, which we shall denote material node point forces, are demonstrated to be of the same qualitative and quantitative importance for the assessment of a fracture mechanics problem as the classical J -integral, see also Steinmann [94, 99], and for additional applications see Müller et al. [72], Müller & Maugin [73] and Kolling et al. [39].

One aim of this work is to discuss a further improvement of the Material Force Method concerning the reliability and accuracy of the evaluation of the vectorial J -integral. For comparison purposes this is validated by a classical fracture mechanics problem formulated in a modified boundary layer style and using the Ramberg-Osgood material type.

Another main goal of this work is to formulate the theory and numerics of non-conservative systems like thermomechanical problems, continuum damage mechanics and plasticity.

In thermomechanical problems the coupling between the mechanical and the thermal response is twofold. On the one hand, we typically encounter thermally induced stresses, i.e., the deformation of the structure strongly depends on the temperature field it is subjected to. On the other hand, large deformations induce structural heating, a phenomenon which is classically referred to as Gough–Joule effect. Traditionally, thermodynamic effects are characterized in the spatial motion context within the framework of rational thermodynamics, see e.g. Truesdell & Toupin [106], Coleman & Noll [18], Truesdell & Noll [105] or the recent textbooks of Silhavy [88], Maugin [61], Haupt [35] or Liu [53]. Conceptually speaking, the spatial setting of continuum thermodynamics considers the response to variations of spatial placements of particles with respect to the ambient space. In a computational context, the basic concern is the evaluation of the spatial motion balance of momentum and energy, whereby the former essentially represents the equilibrium of spatial forces in the sense of Newton. The resulting coupled system of equations defines the evolution of the spatial deformation map and the temperature field. In a finite element context, first attempts towards a numerical solution of finite thermo–elasticity date back to the early work of Oden [74]. A detailed analysis of different staggered solution techniques based on an isothermal or an adiabatic split can be found in Armero & Simo [5]. A comparison with a fully monolithic solution technique has been carried out by Miehe [65], [66], [67] and Simo [91]. In the present work, we shall focus on a simultaneous solution of

the balance of momentum and energy, which has also been documented by Simo & Miehe [92], Reese & Govindjee [78], Reese & Wriggers [79], Reese [77] or Ibrahimbegovic, Chorfi & Gharzeddine [37]. However, in contrast to the above mentioned references, we shall restrict ourselves to the thermo–hyperelastic case in the sequel.

The evolution of the deformation field and the temperature field is typically accompanied with the local rearrangement of material inhomogeneities which can be characterized elegantly within the material motion context, see e.g. the recent contributions by Steinmann [96], [97] and Kuhl & Steinmann [46], [45]. From a computational point of view, the material version of the balance of momentum is particularly attractive since it renders additional information without requiring the solution of a completely new system of equations. Rather, it can be understood as a mere postprocessing step once the spatial motion problem has been solved. Due to its computational efficiency, the material force method has been applied to a number of different problem classes such as thermomechanics by Shih, Moran & Nakamura [85]. Since the resulting discrete material forces typically indicate a potential energy increase upon replacement of the material node point positions, spurious material forces can be utilized to improve the finite element mesh. To this end, Kuhl, Askes & Steinmann [42, 7] analyzed the staggered and the fully coupled solution of the spatial and the material motion balance of momentum introducing both the spatial and the material motion map as primary unknowns. Within the present contribution, however, we shall restrict ourselves to a purely postprocessing–based analysis of the material motion problem. Nevertheless, for the class of inelastic problems considered herein, an additional contribution in the material motion momentum source has to be taken into account. In the context of thermodynamics, this additional term can basically be expressed as a function of the temperature gradient and the entropy density. The elaboration of the influence of the temperature field on the material forces thus constitutes the one main objective of the present work.

Also a concern of this work is to establish a theoretical and computational link between defect mechanics and continuum damage mechanics with the use of the Material Force Method. In the present work we combine an internal variable approach towards damage mechanics with the material force concept. Thereby distributed material volume forces that are conjugated to the damage field arise. Thus the Galerkin discretization of the damage variable as an independent field becomes necessary in addition to the deformation field. An early attempt to set up a mixed finite element formulation, whereby an internal strain-like variable is discretized in addition to the displacement field was provided by Pinsky [76]. An alternative proposal based on a complementary mixed finite element formulation, whereby the loading condition is enforced in weak sense at the element level is due to Simo, Kennedy & Taylor [89]. Likewise, a two-field finite element formulation for elasticity coupled to damage was proposed by Florez-Lopez et al. [30]. Here, consequently, we set up on the one hand the classical balance of momentum and on the other hand a constitutive subproblem corresponding to the Kuhn-Tucker conditions, which are enforced in a weak sense in a coupled fashion. The coupled problem will be

solved using a monolithic solution strategy. The resulting material node point quantities, which we shall denote discrete material node point forces are demonstrated to be closely related to the classical J -integral in fracture mechanics problems.

Furthermore, we focus on material format of the quasi-static balance of momentum of a geometrically nonlinear problem involving elasto-plasticity. Our derivation is motivated by the work of Epstein and Maugin [23, 25, 24], Maugin [56] and Cleja-Tigoiu and Maugin [17].

As an example we consider in particular the modeling of (associated) geometrically linear crystal-plasticity; for an overview see e.g. Asaro [6], the monographs by Besseling and van der Giessen [11] and Phillips [75] and references cited therein, or Vidoli and Sciarra [107] where an alternative multi-field approach is advocated. The underlying numerical formulation is later on applied to single-slip crystal-plasticity with only one possibly active sliding parameter; for detailed discussions on the general algorithmic formulation we refer the reader to Cuitiño and Ortiz [20], Steinmann and Stein [100], Miehe [69, 70] and Miehe and Schröder [71]. This specific assumption, however, enables us to consider a rather concise framework and thereby allows to focus on the one concern of this contribution, namely to elaborate two different numerical approaches within a general finite element setting:

On the one hand, the active sliding parameter is treated as an internal variable. With this field available on the ‘integration point level’, standard interpolation techniques can be applied such that the slip parameter is L_2 -projected to the node points of the finite element mesh, see e.g. Zienkiewicz and Taylor [109]. It is then straightforward to compute the corresponding spatial gradient which is a key ingredient to the material force method. Apparently, loading and unloading conditions, i.e. the Kuhn-Tucker conditions, are incorporated at the ‘integration point level’. In the sequel, this approach is denoted as ‘integration point based’.

On the other hand, the sliding parameter is introduced as an additional degree of freedom. Again, the corresponding spatial gradient represents one of the essential fields for the application of the material force method. In contrast to the previous formulation the computation of this gradient field can conveniently be performed by application of standard finite element techniques. However, loading and unloading conditions, i.e. the Kuhn-Tucker conditions, are now introduced at the ‘node point level’ which results in an active set search borrowed from convex nonlinear programming, compare e.g. the monographs by Luenberger [55], Bazaraa et al. [9] or Bertsekas [10]. We will refer to this approach as ‘node point based’ in the progression of this work.

A comparison of different numerical approaches for the integration point based — and node point based — framework in the context of open system mechanics is given in Kuhl et al. [44] where, however, neither an active set search nor any additional projection algorithms for a mass-flux-free integration point based formulation are needed since the computation of material volume forces is not in the main focus of that contribution (but of [45]). Nevertheless, the spatial gradient of the, say, internal variable is of importance

for the computation of the underlying material forces. As an interesting side aspect, these gradient terms are typically introduced into the concept of higher-order gradient — or rather non-local — continua. Especially crystalline solids have been explored within that setting, see e.g. Kosevich [40] and Kröner [41] and references cited therein, Anthony and Azirhi [4], Steinmann [93], Menzel and Steinmann [64], Acharya and Bassani [1], Davini [21], Cermelli and Gurtin [13, 14], Svendsen [102] and others and e.g. Svedberg [101, paperE] and Liebe et al. [50] for inelastic and geometrically nonlinear numerical applications as based on the finite element method. Based on the results of crystal-plasticity we additionally formulate the material force method for geometrically linear von Mises type plasticity model.

The present work is mainly divided in four parts. In the first part we will introduce the basic notions of the mechanics and numerics of material forces for a quasi-static conservative mechanical system. In this case the internal potential energy density per unit volume characterizes a hyperelastic material behaviour. In the first numerical example we discuss the reliability of the material force method to calculate the vectorial J -integral of a crack in a Ramberg-Osgood type material under mode I loading and superimposed T -stresses. Secondly, we study the direction of the single material force acting as the driving force of a kinked crack in a geometrically nonlinear hyperelastic Neo-Hooke material.

In the second part we focus on material forces in the case of geometrically nonlinear thermo-hyperelastic material behaviour. Therefore we adapt the theory and numerics to a transient coupled problem, and elaborate the format of the Eshelby stress tensor as well as the internal material volume forces induced by the gradient of the temperature field. We study numerically the material forces in a bimaterial bar under tension load and the time dependent evolution of material forces in a cracked specimen.

The third part discusses the material force method in the case of geometrically nonlinear isotropic continuum damage. The basic equations are similar to those of the thermo-hyperelastic problem but we introduce an alternative numerical scheme, namely an active set search algorithm, to calculate the damage field as an additional degree of freedom. With this at hand, it is an easy task to obtain the gradient of the damage field which induces the internal material volume forces. Numeric examples in this part are a specimen with an elliptic hole with different semi-axis, a center cracked specimen and a cracked disc under pure mode I loading.

In the fourth part of this work we elaborate the format of the Eshelby stress tensor and the internal material volume forces for geometrically nonlinear multiplicative elastoplasticity. Concerning the numerical implementation we restrict ourselves to the case of geometrically linear single slip crystal plasticity and compare here two different numerical methods to calculate the gradient of the internal variable which enters the format of the internal material volume forces. The two numerical methods are firstly, a node point based approach, where the internal variable is addressed as an additional degree of freedom, and secondly, a standard approach where the internal variable is only available at the integration points level. Here a least square projection scheme is enforced to calculate

the necessary gradients of this internal variable. As numerical examples we discuss a specimen with an elliptic inclusion and an elliptic hole respectively and, in addition, a crack under pure mode I loading in a material with different slip angles. Here we focus on the comparison of the two different methods to calculate the gradient of the internal variable.

As a second class of numerical problems we elaborate and implement a geometrically linear von Mises plasticity with isotropic hardening. Here the necessary gradients of the internal variables are calculated by the already mentioned projection scheme. The results of a crack in a material with different hardening behaviour under various additional T -stresses are given.

Chapter 2

Hyperelasticity

To set the stage and in order to introduce terminology and notation, we briefly reiterate some key issues pertaining to the geometrically nonlinear kinematics of the quasi-static spatial and material motion problem. This chapter based on the work which was partially published in [22].

2.1 Duality in kinematics

2.1.1 Spatial motion problem

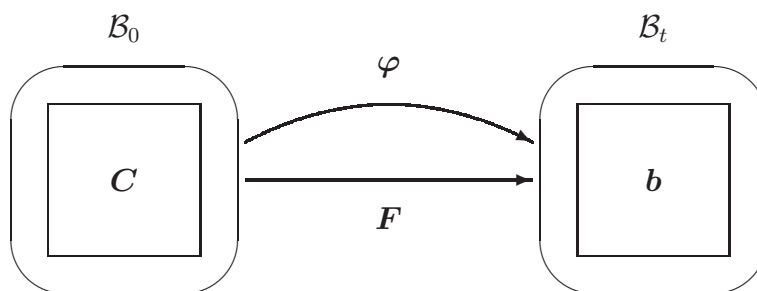


Figure 2.1. Kinematics of the spatial motion problem

In the spatial motion problem in fig. 2.1, the placement \boldsymbol{x} of a ‘physical particle’ in the spatial configuration \mathcal{B}_t is described by the nonlinear spatial motion deformation map

$$\boldsymbol{x} = \boldsymbol{\varphi}(\boldsymbol{X}) \tag{2.1}$$

in terms of the placement \boldsymbol{X} of the same ‘physical particle’ in the material configuration \mathcal{B}_0 . The spatial motion deformation gradient, i.e. the linear tangent map associated to the spatial motion deformation map, together with its determinant are then given by

$$\mathbf{F} = \nabla_{\mathbf{X}}\varphi(\mathbf{X}) \quad \text{and} \quad J = \det \mathbf{F}. \quad (2.2)$$

Finally, typical strain measures are defined over the cotangent space to \mathcal{B}_0 and the tangent space to \mathcal{B}_t by the right and left spatial motion Cauchy-Green strain tensors, respectively

$$\mathbf{C} = \mathbf{F}^t \cdot \mathbf{g} \cdot \mathbf{F} \quad \text{and} \quad \mathbf{b} = \mathbf{F} \cdot \mathbf{G}^{-1} \cdot \mathbf{F}^t. \quad (2.3)$$

Hereby \mathbf{C} can be interpreted as the spatial motion pull back of the covariant spatial metric \mathbf{g} and \mathbf{b} as the push forward of the contravariant material metric \mathbf{G}^{-1} .

2.1.2 Material motion problem

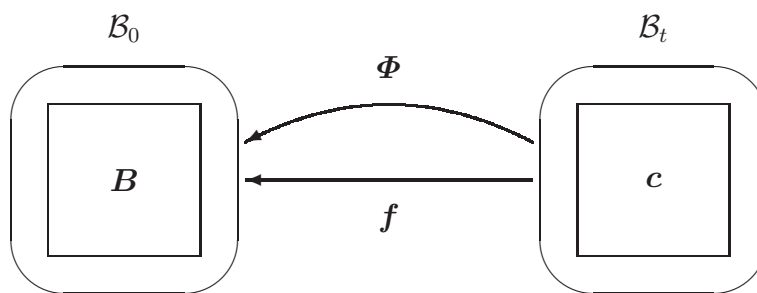


Figure 2.2. Kinematics of the material motion problem

In the material motion problem in fig. 2.2 the placement \mathbf{X} of a ‘physical particle’ in the material configuration \mathcal{B}_0 is described by the nonlinear material motion deformation map

$$\mathbf{X} = \Phi(\mathbf{x}) \quad (2.4)$$

in terms of the placement \mathbf{x} of the same ‘physical particle’ in the spatial configuration \mathcal{B}_t . The material motion deformation gradient, i.e. the linear tangent map associated to the material motion deformation map, together with its determinant are then given by

$$\mathbf{f} = \nabla_{\mathbf{x}}\Phi(\mathbf{x}) \quad \text{and} \quad j = \det \mathbf{f}. \quad (2.5)$$

Finally, typical strain measures are defined over the cotangent space to \mathcal{B}_t and the tangent space to \mathcal{B}_0 as the right and left material motion Cauchy-Green strain tensors, respectively

$$\mathbf{c} = \mathbf{f}^t \cdot \mathbf{G} \cdot \mathbf{f} \quad \text{and} \quad \mathbf{B} = \mathbf{f} \cdot \mathbf{g}^{-1} \cdot \mathbf{f}^t \quad (2.6)$$

Analog to the spatial motion problem \mathbf{c} can be interpreted as the material motion pull back of the covariant material metric tensor \mathbf{G} and \mathbf{B} by the push forward of the contravariant spatial metric \mathbf{g}^{-1} .

2.1.3 Spatial and material motion problem

The direct and inverse motion description are linked together by the identity maps in \mathcal{B}_t and \mathcal{B}_0

$$\text{id}_{\mathcal{B}_t} = \varphi \circ \Phi(\mathbf{x}) = \varphi(\Phi(\mathbf{x})) \quad \text{and} \quad \text{id}_{\mathcal{B}_0} = \Phi \circ \varphi(\mathbf{X}) = \Phi(\varphi(\mathbf{X})) \quad (2.7)$$

whereby \circ denotes the composition of two functions.

In addition the direct and inverse deformation gradients \mathbf{F} and \mathbf{f} are related by

$$\mathbf{F}^{-1} = \mathbf{f} \circ \varphi(\mathbf{X}) = \mathbf{f}(\varphi(\mathbf{X})) \quad \text{and} \quad \mathbf{f}^{-1} = \mathbf{F} \circ \Phi(\mathbf{x}) = \mathbf{F}(\Phi(\mathbf{x})). \quad (2.8)$$

Without danger of confusion we make no distinction between \mathbf{F}^{-1} and \mathbf{f} in the spatial motion problem or \mathbf{f}^{-1} and \mathbf{F} in the material motion problem, respectively, in our further definitions.

Furthermore, the spatial Cauchy-Green strain tensors \mathbf{C} and \mathbf{b} and the corresponding material Cauchy-Green strain tensors \mathbf{c} and \mathbf{B} are related via their inverses.

$$\mathbf{C}^{-1} = \mathbf{B} \quad \text{and} \quad \mathbf{b}^{-1} = \mathbf{c} \quad (2.9)$$

2.2 Duality in balance of momentum

In the sequel, we shall derive the appropriate formats of the balance of momentum and emphasize the formal duality of spatial and material forces acting on arbitrary subdomains of a body with the corresponding quasi-static equilibrium conditions.

Thereby, in order to introduce the relevant concepts, we merely consider a conservative mechanical system. In this case, the internal potential energy density W_τ per unit volume in \mathcal{B}_τ with $\tau = 0, t$ characterizes the hyperelastic material response and is commonly denoted as stored energy density. Moreover, an external potential energy density V_τ characterizes the conservative loading. Then the conservative mechanical system is essentially characterized by the total potential energy density per unit volume $U_\tau = W_\tau + V_\tau$.

2.2.1 Spatial motion problem

For the spatial motion problem the quasi-static balance of momentum reads

$$-\text{Div} \mathbf{\Pi}^t = \mathbf{b}_0 \quad \implies \quad -\text{div} \boldsymbol{\sigma}^t = \mathbf{b}_t. \quad (2.10)$$

The two-point description stress $\mathbf{\Pi}^t$ and the spatial description stress $\boldsymbol{\sigma}^t$, see fig. 2.3, which are called the spatial motion first Piola-Kirchhoff and Cauchy stresses, have been introduced here. For the present case of a conservative mechanical system, they can be derived by means of the potential energy density as

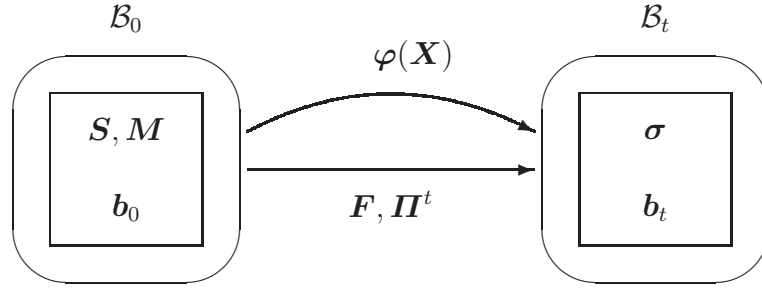


Figure 2.3. Kinetics of the spatial motion problem

$$\mathbf{\Pi}^t = \partial_{\mathbf{F}} U_0 \quad \Longrightarrow \quad \boldsymbol{\sigma}^t = j \mathbf{\Pi}^t \cdot \mathbf{F}^t = U_t \mathbf{I} - \mathbf{f}^t \cdot \partial_{\mathbf{f}} U_t. \quad (2.11)$$

Thereby the second expression in eq. 2.11 denotes the energy-momentum format of the spatial motion Cauchy stress. For the sake of conciseness and without danger of confusion, we omitted the explicit indication of the spatial or material parametrization.

Moreover, distributed volume forces \mathbf{b}_τ per unit volume follow from the explicit spatial gradient of the total potential energy density

$$\mathbf{b}_0 = -\partial_{\mathbf{x}} U_0 \quad \Longrightarrow \quad \mathbf{b}_t = j \mathbf{b}_0 \quad (2.12)$$

In addition, the spatial motion stresses $\mathbf{S}^t = \mathbf{f} \cdot \mathbf{\Pi}^t$ and $\mathbf{M}^t = \mathbf{F}^t \cdot \mathbf{\Pi}^t$ in material description are defined for completeness. Here, \mathbf{S} and \mathbf{M} denote the second Piola-Kirchhoff and the Mandel stress in the spatial motion problem, respectively.

We now observe an arbitrary subdomain \mathcal{V}_t with boundary $\partial\mathcal{V}_t$ of the spatial configuration \mathcal{B}_t . The subdomain is loaded along $\partial\mathcal{V}_t$ by spatial description surface tractions in terms of the spatial description Cauchy stress $\boldsymbol{\sigma}$ (projected by the spatial surface normal \mathbf{n}) and within \mathcal{V}_t by spatial description volume forces \mathbf{b}_t , e.g. gravity. Then we may define the resultant spatial description surface and volume forces acting on \mathcal{V}_t as

$$\mathfrak{t}_{sur} = \int_{\partial\mathcal{V}_t} \boldsymbol{\sigma}^t \cdot \mathbf{n} \, da \quad \text{and} \quad \mathfrak{t}_{vol} = \int_{\mathcal{V}_t} \mathbf{b}_t \, dv \quad (2.13)$$

Finally, the statement of quasi-static equilibrium of spatial forces for the subdomain with spatial configuration \mathcal{V}_t is simply written as

$$\mathfrak{t}_{sur} + \mathfrak{t}_{vol} = \mathbf{0} \quad (2.14)$$

The local format of eq. 2.14 coincides with eq. 2.10.

2.2.2 Material motion problem

For the material motion problem, the quasi-static balance of momentum reads

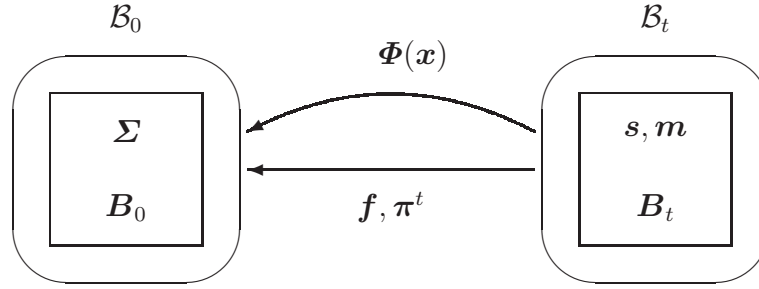


Figure 2.4. Kinetics of the material motion problem

$$-\text{Div}\boldsymbol{\Sigma}^t = \mathbf{B}_0 \quad \Leftarrow \quad -\text{div}\boldsymbol{\pi}^t = \mathbf{B}_t. \quad (2.15)$$

The two-point description stress $\boldsymbol{\pi}^t$ and the material description stress $\boldsymbol{\Sigma}^t$, see fig. 2.4, which may be called the material motion first Piola-Kirchhoff and Cauchy stresses, have been introduced here. For the present case of a conservative mechanical system, they follow from the potential energy density as

$$\boldsymbol{\Sigma}^t = J\boldsymbol{\pi}^t \cdot \mathbf{f}^t = U_0\mathbf{I} - \mathbf{F}^t \cdot \partial_{\mathbf{F}}U_0 \quad \Leftarrow \quad \boldsymbol{\pi}^t = \partial_{\mathbf{f}}U_t \quad (2.16)$$

Thereby, the first expression in eq. 2.16 denotes the energy-momentum format of the material motion Cauchy stress, which is commonly denoted as the Eshelby stress. For the sake of conciseness and without danger of confusion, we again omitted the explicit indication of the spatial or material parametrization.

Moreover, distributed volume forces \mathbf{B}_τ per unit volume follow from the explicit material gradient of the potential energy density with respect to the material coordinates

$$\mathbf{B}_0 = J\mathbf{B}_t \quad \Leftarrow \quad \mathbf{B}_t = -\partial_{\mathbf{X}}U_t. \quad (2.17)$$

Corresponding to the spatial motion problem, we can also define the second Piola-Kirchhoff and the Mandel stress in spatial description for completeness. We thus obtain $\mathbf{s}^t = \mathbf{F} \cdot \boldsymbol{\pi}^t$ and $\mathbf{m}^t = \mathbf{f}^t \cdot \boldsymbol{\pi}^t$, respectively, in the material motion problem.

We now observe an arbitrary subdomain \mathcal{V}_0 with boundary $\partial\mathcal{V}_0$ of the material configuration \mathcal{B}_0 . The subdomain is loaded along $\partial\mathcal{V}_0$ by surface tractions in terms of the material Cauchy stress $\boldsymbol{\Sigma}$ (projected by the material surface normal \mathbf{N}) and within \mathcal{V}_0 by material volume forces \mathbf{B}_0 , stemming e.g. from material inhomogeneities. We may then define the resultant material description surface and volume forces acting on \mathcal{V}_0 as

$$\mathfrak{f}_{sur} = \int_{\partial\mathcal{V}_0} \boldsymbol{\Sigma}^t \cdot \mathbf{N} \, dA \quad \text{and} \quad \mathfrak{f}_{vol} = \int_{\mathcal{V}_0} \mathbf{B}_0 \, dV. \quad (2.18)$$

Finally, the statement of quasi-static equilibrium of material forces for the subdomain with material configuration \mathcal{V}_0 is simply written as

$$\mathfrak{F}_{sur} + \mathfrak{F}_{vol} = \mathbf{0}. \quad (2.19)$$

Again the local format of eq. 2.19 coincides with eq. 2.15.

2.3 J -Integral from equilibrium of material forces

In order to highlight the notion of material forces, we shall relate this concept to the familiar J -integral in fracture mechanics. To this end, we consider an arbitrary subdomain \mathcal{V}_0 of the material configuration \mathcal{B}_0 , see fig. 2.5. The boundary $\partial\mathcal{V}_0$ is thereby assumed to be decomposed into a regular and a singular part $\partial\mathcal{V}_0 = \partial\mathcal{V}_0^r \cup \partial\mathcal{V}_0^s$ with $\emptyset = \partial\mathcal{V}_0^r \cap \partial\mathcal{V}_0^s$. The singular part of $\partial\mathcal{V}_0$ denotes a crack tip in this case.

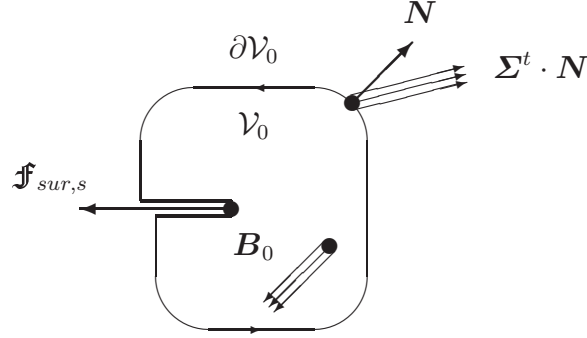


Figure 2.5. Arbitrary subdomain with regular and singular part of its boundary

For nonvanishing material description volume forces $\mathbf{B}_0 \neq \mathbf{0}$ within \mathcal{V}_0 , eq. 2.19 renders the following relation between the material description surface and volume forces

$$\int_{\partial\mathcal{V}_0} \boldsymbol{\Sigma}^t \cdot \mathbf{N} \, dA = - \int_{\mathcal{V}_0} \mathbf{B}_0 \, dV. \quad (2.20)$$

After decomposing the boundary $\partial\mathcal{V}_0$ into a regular and a singular boundary part, the resulting material force acting on the singular boundary is given by

$$\mathfrak{F}_{sur,s} := \int_{\partial\mathcal{V}_0^s} \boldsymbol{\Sigma}^t \cdot \mathbf{N} \, dA = - \int_{\partial\mathcal{V}_0^r} \boldsymbol{\Sigma}^t \cdot \mathbf{N} \, dA - \int_{\mathcal{V}_0} \mathbf{B}_0 \, dV \quad (2.21)$$

Please note that this material force coincides with a vectorial generalization of the J -integral as originally proposed by Rice¹ [80] modulo a change of sign which stems from the integration along the regular part instead of integration along the singular part of $\partial\mathcal{V}_0$.

¹Rice proposed in his work the first component as the J -integral.

$$-\mathfrak{F}_{sur,s} = \mathfrak{F} = \lim_{\partial\mathcal{V}_0^r \rightarrow 0} \int_{\partial\mathcal{V}_0^r} \boldsymbol{\Sigma}^t \cdot \mathbf{N} \, dA \quad (2.22)$$

Issues of path dependence of the J -integral can now easily be discussed based on straightforward material equilibrium considerations.

2.4 Virtual work and discretization

In the following, the quasi-static balances of momentum for the spatial and the material motion problem will be recast in their weak or rather variational form. The variational formats of the quasi-static balances of momentum readily lead to a straightforward Galerkin discretization. As a result, discrete spatial and material node point (surface) forces are obtained.

2.4.1 Spatial motion problem

The pointwise statement in eq. 2.10 for the solution of the spatial motion problem is multiplied by a test function (spatial virtual displacement) \mathbf{w} under the necessary smoothness and boundary assumptions to render the virtual work expression

$$\underbrace{\int_{\partial\mathcal{B}_t} \mathbf{w} \cdot \boldsymbol{\sigma}^t \cdot \mathbf{n} \, da}_{\mathfrak{w}^{sur}} = \underbrace{\int_{\mathcal{B}_t} \nabla_x \mathbf{w} : \boldsymbol{\sigma}^t \, dv}_{\mathfrak{w}^{int}} - \underbrace{\int_{\mathcal{B}_t} \mathbf{w} \cdot \mathbf{b}_t \, dv}_{\mathfrak{w}^{vol}} \quad \forall \mathbf{w}. \quad (2.23)$$

Whereby \mathfrak{w}^{sur} denotes the spatial variation of the total bulk potential energy due to its complete dependence on the spatial position, whereas the contributions \mathfrak{w}^{int} and \mathfrak{w}^{vol} denote the spatial variations of the total bulk potential energy due to its implicit and explicit dependence on the spatial position, respectively.

The quasi-static equilibrium of spatial forces in eq. 2.14 is recovered, if arbitrary uniform spatial virtual displacements $\mathbf{w} = \boldsymbol{\theta}$ are selected for the evaluation of eq. 2.23

$$\boldsymbol{\theta} \cdot \left[\int_{\partial\mathcal{B}_t} \boldsymbol{\sigma}^t \cdot \mathbf{n} \, da + \int_{\mathcal{B}_t} \mathbf{b}_t \, dv \right] = 0 \quad \forall \boldsymbol{\theta} \quad (2.24)$$

The domain is discretized in n_{el} elements with $\mathcal{B}_0^h = \cup_{e=1}^{n_{el}} \mathcal{B}_0^e$ and $\mathcal{B}_t^h = \cup_{e=1}^{n_{el}} \mathcal{B}_t^e$ as shown in fig. 2.6. The geometry in \mathcal{B}_t and \mathcal{B}_0 is interpolated from the positions $\boldsymbol{\varphi}_n$ and \mathbf{X}_n of the n_{en} nodes by shape functions N^n on each element, with $n \in [1, n_{en}]$ denoting the local node numbering

$$\boldsymbol{\varphi}^h|_{\mathcal{B}_t^e} = \sum_{n=1}^{n_{en}} N^n \boldsymbol{\varphi}_n \quad \text{and} \quad \mathbf{X}^h|_{\mathcal{B}_0^e} = \sum_{n=1}^{n_{en}} N^n \mathbf{X}_n. \quad (2.25)$$

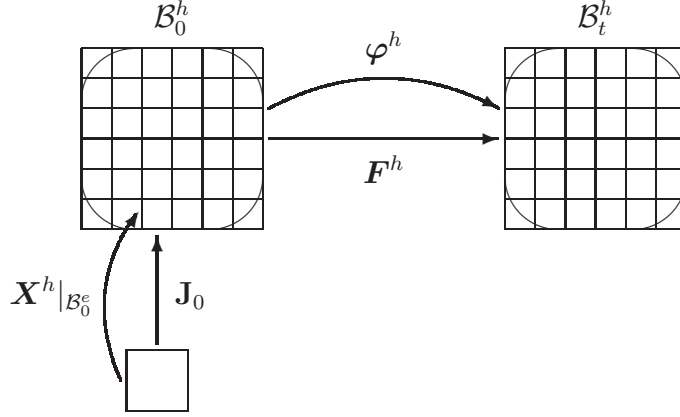


Figure 2.6. Discretization of the spatial motion problem

Thus, the elementwise discretization of the virtual spatial displacement field \mathbf{w} into nodal values \mathbf{w}_n which are interpolated as well by the shape functions N^n in the spirit of an isoparametric expansion, renders the representation

$$\mathbf{w}^h|_{\mathcal{B}_t^e} = \sum_{n=1}^{n_{en}} N^n \mathbf{w}_n \quad (2.26)$$

Furthermore, the elementwise Jacobi matrix

$$\mathbf{J}_0 = \nabla_{\xi} \mathbf{X}^h|_{\mathcal{B}_0^e} = \sum_{n=1}^{n_{en}} \mathbf{X}_k \otimes \nabla_{\xi} N_X^k \quad (2.27)$$

is needed to compute the material gradients $\nabla_X \{\bullet\} = \nabla_{\xi} \{\bullet\} \cdot \mathbf{J}_0^{-1}$ by the chain rule.

The corresponding gradients of the virtual spatial displacement field are given in each element by

$$\nabla_X \mathbf{w}^h|_{\mathcal{B}_t^e} = \sum_{n=1}^{n_{en}} \mathbf{w}_n \otimes \nabla_X N^n \quad \text{and} \quad \nabla_x \mathbf{w}^h|_{\mathcal{B}_t^e} = \sum_{n=1}^{n_{en}} \mathbf{w}_n \otimes \nabla_x N^n \quad (2.28)$$

Lastly, based on the above discretizations, the corresponding deformation gradient \mathbf{F} takes the elementwise format

$$\mathbf{F}^h|_{\mathcal{B}_0^e} = \sum_k \varphi_k \otimes \nabla_X N_{\varphi}^k \quad (2.29)$$

The elementwise expansions for the internal and the volume contributions therefore read

$$\mathfrak{w}_e^{int} = \sum_{n=1}^{n_{en}} \mathbf{w}_n \cdot \int_{\mathcal{B}_t^e} \boldsymbol{\sigma}^t \cdot \nabla_x N^n \, dv \quad \text{and} \quad \mathfrak{w}_e^{vol} = \sum_{n=1}^{n_{en}} \mathbf{w}_n \cdot \int_{\mathcal{B}_t^e} \mathbf{b}_t N^n \, dv \quad (2.30)$$

Finally, considering the arbitrariness of the spatial virtual node point displacements \mathbf{w}_n , the global discrete spatial node point forces characterizing external spatial surface loads are computed as

$$\mathbf{t}_{sur}^h = \mathbf{A}_{e=1}^{n_{el}} \int_{\mathcal{B}_t^e} [\boldsymbol{\sigma}^t \cdot \nabla_x N^n - \mathbf{b}_t N^n] dv \quad (2.31)$$

In conclusion of these considerations, the discrete spatial node point (surface) forces are thus energetically conjugated to variations of the spatial node point positions.

2.4.2 Material motion problem

The pointwise statement in eq. 2.15 for the solution of the material motion problem is multiplied by a test function (material virtual displacement) \mathbf{W} under the necessary smoothness and boundary assumptions to render the virtual work expression

$$\underbrace{\int_{\partial \mathcal{B}_0} \mathbf{W} \cdot \boldsymbol{\Sigma}^t \cdot \mathbf{N} dA}_{\mathfrak{B}^{sur}} = \underbrace{\int_{\mathcal{B}_0} \nabla_X \mathbf{W} : \boldsymbol{\Sigma}^t dV}_{\mathfrak{B}^{int}} - \underbrace{\int_{\mathcal{B}_0} \mathbf{W} \cdot \mathbf{B}_0 dV}_{\mathfrak{B}^{vol}} \quad \forall \mathbf{W}. \quad (2.32)$$

Whereby \mathfrak{B}^{sur} denotes the material variation of the total bulk potential energy due to its complete dependence on the material position, whereas the contributions \mathfrak{B}^{int} and \mathfrak{B}^{vol} denote the material variations of the total bulk potential energy due to its implicit and explicit dependence on the material position, respectively.

The quasi-static equilibrium of material forces in eq. 2.19 is recovered if arbitrary uniform material virtual displacements $\mathbf{W} = \boldsymbol{\Theta}$ are selected for the evaluation of eq. 2.32

$$\boldsymbol{\Theta} \cdot \left[\int_{\partial \mathcal{B}_0} \boldsymbol{\Sigma}^t \cdot \mathbf{N} dA + \int_{\mathcal{B}_0} \mathbf{B}_0 dV \right] = 0 \quad \forall \boldsymbol{\Theta}. \quad (2.33)$$

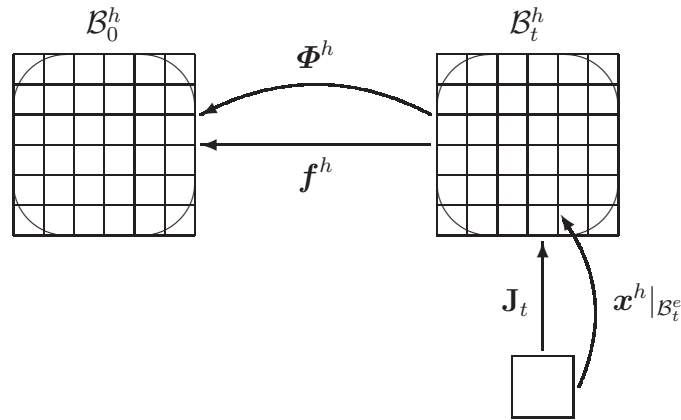


Figure 2.7. Discretization of the material motion problem

Next the domain is discretized in n_{el} elements with $\mathcal{B}_t^h = \cup_{e=1}^{n_{el}} \mathcal{B}_t^e$ and $\mathcal{B}_0^h = \cup_{e=1}^{n_{el}} \mathcal{B}_0^e$, see fig. 2.7. On each element the geometry in \mathcal{B}_0 and \mathcal{B}_t is interpolated from the positions Φ_n and \mathbf{x}_n of the n_{en} nodes by shape functions N^n , with $n \in [1, n_{en}]$ denoting the local node numbering

$$\Phi^h|_{\mathcal{B}_0^e} = \sum_{n=1}^{n_{en}} N^n \Phi_n \quad \text{and} \quad \mathbf{x}^h|_{\mathcal{B}_t^e} = \sum_{n=1}^{n_{en}} N^n \mathbf{x}_n. \quad (2.34)$$

The elementwise discretization of the virtual material displacement field \mathbf{W} into nodal values \mathbf{W}_n , which are interpolated as well by the shape functions N^n in the spirit of an isoparametric expansion, renders the representation

$$\mathbf{W}^h|_{\mathcal{B}_0^e} = \sum_{n=1}^{n_{en}} N^n \mathbf{W}_n. \quad (2.35)$$

Thereby, the shape functions render a globally C^0 -continuous interpolation by assembling all elementwise expansions. Furthermore, the elementwise Jacobi matrix

$$\mathbf{J}_t = \nabla_\xi \mathbf{x}^h|_{\mathcal{B}_t^e} = \sum_{n=1}^{n_{en}} \mathbf{x}_k \otimes \nabla_\xi N_x^k \quad (2.36)$$

is needed to compute the gradients $\nabla_x \{\bullet\} = \nabla_\xi \{\bullet\} \cdot \mathbf{J}_t^{-1}$ by chain rule.

Corresponding gradients of the virtual material displacement field are given in each element by

$$\nabla_x \mathbf{W}^h|_{\mathcal{B}_0^e} = \sum_{n=1}^{n_{en}} \mathbf{W}_n \otimes \nabla_x N^n \quad \text{and} \quad \nabla_X \mathbf{W}^h|_{\mathcal{B}_0^e} = \sum_{n=1}^{n_{en}} \mathbf{W}_n \otimes \nabla_X N^n. \quad (2.37)$$

Lastly, based on the above discretizations, the corresponding gradients \mathbf{f} and $\nabla_x \mathbf{W}$ take the elementwise format

$$\mathbf{f}^h|_{\mathcal{B}_t^e} = \sum_k \Phi_k \otimes \nabla_x N_\Phi^k. \quad (2.38)$$

Thereby the elementwise expansions for the internal and the volume contributions read

$$\mathfrak{B}_e^{int} = \sum_{n=1}^{n_{en}} \mathbf{W}_n \cdot \int_{\mathcal{B}_0^e} \Sigma^t \cdot \nabla_X N^n \, dV \quad \text{and} \quad \mathfrak{B}_e^{vol} = \sum_{n=1}^{n_{en}} \mathbf{W}_n \cdot \int_{\mathcal{B}_0^e} \mathbf{B}_0 N^n \, dV. \quad (2.39)$$

Finally, considering the arbitrariness of the material virtual node point displacements \mathbf{W}_n , the global discrete material node point forces characterizing external material surface loads are computed as

$$\mathfrak{f}_{sur}^h = \mathbf{A}_{e=1}^{n_{el}} \int_{\mathcal{B}_0^e} [\Sigma^t \cdot \nabla_X N^n - \mathbf{B}_0 N^n] \, dV. \quad (2.40)$$

In conclusion of these considerations, the discrete material node point (surface) forces are thus energetically conjugated to variations of the material node point positions.

In summary, the Material Force Method advocated in this contribution is based essentially on eq. 2.40. The additional computational steps pertaining to the Material Force Method are then:

- Compute material motion stress and volume force at quadrature points
- Perform standard numerical quadrature

Thus, the method simply consists of the determination of the discrete material node point forces corresponding to the material motion problem which are trivially computable after the spatial motion problem has been solved. In particular, no additional data structures or subroutines are necessary.

2.4.3 Material Force Method for J -integral evaluation

For the sake of simplicity and without loss of generality, we shall consider cases with vanishing material volume forces \mathbf{B}_0 . Recall that the discrete material node point force given by eq. 2.40, acting on a node representing the crack tip is equal to the vectorial J -integral. The accuracy of the numerical evaluation strongly depends on the accuracy of the Eshelby stress in the vicinity of the crack tip. Due to the singular behaviour of the spatial motion stresses and strains near the crack tip, the accuracy of $\boldsymbol{\Sigma}$ is often insufficient within a finite element setting.

In special cases, it is possible to overcome this problem by introducing special crack tip elements, like e.g. [8], but this is restricted to problems where the type of the singularity in the strain field is a priori known, like e.g. linear elastic crack problems.

For an improvement of the method proposed in eq. 2.40, we consider in general a given subdomain \mathcal{V}_0 in the material configuration \mathcal{V}_0 which encloses the crack tip with the boundary decomposed in a regular part $\partial\mathcal{V}_0^r$ and a singular part $\partial\mathcal{V}_0^s$ as shown in fig. 2.8. We propose to evaluate the vectorial J -integral by the summation of all discrete material node point forces in a given finite subdomain \mathcal{V}_0 except those which are associated with the regular boundary $\partial\mathcal{V}_0^r$

$$\mathfrak{J} = - \sum_{n=1}^{\bar{n}_{np}} \mathbf{A}_{e=1}^{nel} \int_{\mathcal{B}_0^e} [\boldsymbol{\Sigma}^t \cdot \nabla_X N^n] dV, \quad (2.41)$$

where \bar{n}_{np} is the number of all nodes lying in the subdomain $\mathcal{V}_0 \setminus \partial\mathcal{V}_0^r$.

Within a finite element setting, the discrete singular material node point (surface) force $\mathfrak{F}_{sur,s}^h$ is in balance with the discrete material node point (surface) force $\mathfrak{F}_{sur,r}^h$ on the regular boundary $\partial\mathcal{V}_0^r$ and the spurious discrete internal material node point (surface) forces $\mathfrak{F}_{sur,i}^h$. Consequently, the singular material (surface) force $\mathfrak{F}_{sur,s}$ is approximated by

$$\mathfrak{F}_{sur,s} \approx -\mathfrak{F}_{sur,r}^h = \mathfrak{F}_{sur,s}^h + \mathfrak{F}_{sur,i}^h \quad (2.42)$$

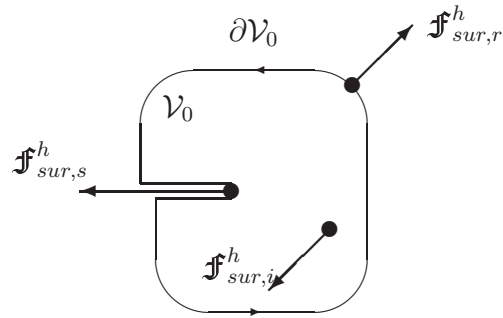


Figure 2.8. Balance of discrete material node point (surface) forces

This proposal is motivated by the occurrence of spurious discrete internal material node point (surface) forces $\mathfrak{F}_{sur,i}^h$ in the case of a poor approximation of the singular stress and strain fields in the vicinity of the crack tip caused by e.g. biquadratic P2 elements, as shown in fig. 2.9a. Whereas in the case of a good approximation of the singular behaviour by S2s elements [8] those spurious material node point forces almost vanish, see fig. 2.9b.

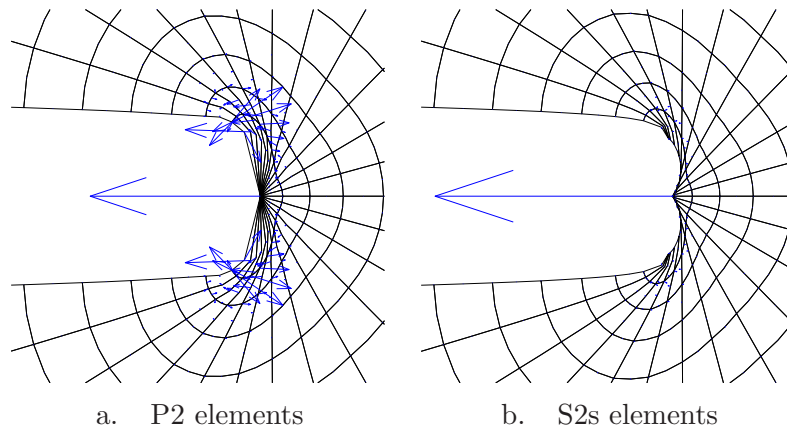


Figure 2.9. Material forces in the vicinity of the crack tip

Our proposal is strongly related to the domain integral method introduced by Li et al. [48] and Shih et al. [85]. They introduced a sufficiently smooth function, say $\bar{W} \in H^1(\mathcal{V}_0)$, which takes the value one on $\partial\mathcal{V}_0^s$ and zero on $\partial\mathcal{V}_0^r$ and obtain for the evaluation of the J -integral

$$J = - \int_{\partial\mathcal{V}_0^r \cup \partial\mathcal{V}_0^s} \bar{W} \mathbf{e}_{\parallel} \cdot \boldsymbol{\Sigma}^t \cdot \mathbf{N} \, dA = - \int_{\partial\mathcal{V}_0} \bar{W} \cdot \boldsymbol{\Sigma}^t \cdot \mathbf{N} \, dA \quad \text{with } \bar{W} = \begin{cases} 1 & \text{on } \partial\mathcal{V}_0^s \\ 0 & \text{on } \partial\mathcal{V}_0^r \end{cases} \quad (2.43)$$

The application of the Gauss theorem and integration by parts as well as a subsequent standard Galerkin discretization of the preselected integration domain into \bar{n}_{el} elements with $\mathcal{V}_0^h = \cup_{e=1}^{\bar{n}_{el}} \mathcal{B}_{0e}$ and the selection of a prescribed virtual material displacement $\bar{\mathbf{W}}^h = \sum_{n=1}^{n_{en}} N^n \bar{\mathbf{W}}_n$ then renders the algorithmic version of the domain integral method

$$J = - \sum_{n=1}^{\bar{n}_{np}} \mathbf{A}_{e=1}^{n_{el}} \bar{\mathbf{W}}_n \cdot \int_{\mathcal{B}_0^e} [\boldsymbol{\Sigma}^t \cdot \nabla_X N^n] dV \quad (2.44)$$

It is thus obvious that the proposed Material Force Method in eq. 2.41 projected to \mathbf{e}_{\parallel} is equivalent to the domain integral method eq. 2.44 if we choose

$$\bar{\mathbf{W}}_n = \begin{cases} \mathbf{e}_{\parallel} & \text{if } n \in \mathcal{V}_0^h \setminus \partial \mathcal{V}_0^{hr} \\ \mathbf{0} & \text{if } n \in \partial \mathcal{V}_0^{hr} \end{cases} \quad (2.45)$$

So this special function could be interpreted as a 'plateau'-function in \mathcal{V}_0^h . Although Shih et al. [85] observed that there is no significant influence of the choice of the virtual material displacement function $\bar{\mathbf{W}}_n$ on the results, we prefer our approach based on the notion of equilibrium of material forces. Nevertheless, the Material Force Method does not restrict the evaluation to the \mathbf{e}_{\parallel} -direction. Vectorial material force quantities clearly contain more information than scalar ones.

2.5 The geometrically linear case

Until now we have formulated our problem in a geometrically nonlinear setting. But from a historical point of view the Eshelby stress and the corresponding material forces were introduced by Eshelby [27] in geometrically linear setting. Furthermore, the (scalar-valued) J -integral, which is a commonly used fracture parameter in fracture mechanics, was introduced by Cherepanov [16] and Rice [80] also for a geometrically linear setting. Therefore, we now elaborate the format of the Eshelby stress tensor for this case.

We start with the balance of linear momentum

$$\operatorname{div} \boldsymbol{\sigma}^t + \mathbf{b} = \mathbf{0} \quad (2.46)$$

and pre-multiply this with the displacement gradient $\mathbf{h} = \nabla \mathbf{u}$.

$$\mathbf{h}^t \cdot \operatorname{div} \boldsymbol{\sigma}^t + \mathbf{h}^t \cdot \mathbf{b} = \operatorname{div}(\mathbf{h}^t \cdot \boldsymbol{\sigma}^t) - \nabla \mathbf{h}^t : \boldsymbol{\sigma}^t + \mathbf{h}^t \cdot \mathbf{b} = \mathbf{0} \quad (2.47)$$

Next we use the compatibility of \mathbf{h}

$$\nabla \mathbf{h}^t : \boldsymbol{\sigma}^t = \boldsymbol{\sigma}^t : \nabla \mathbf{h} \quad (2.48)$$

and the hyperelastic character of the stress $\boldsymbol{\sigma}^t = \mathbf{d}_{\mathbf{h}} W$, whereby W is the stored energy density of an elastic material, so that we get

$$\boldsymbol{\sigma}^t : \nabla \mathbf{h} = d_{\mathbf{h}} W : \nabla \mathbf{h} = \operatorname{div}(W\mathbf{I}) - \partial_{\mathbf{x}} W \quad (2.49)$$

Assembling all the terms we can identify the material motion quasi-static balance of momentum

$$\operatorname{div}(W\mathbf{I} - \mathbf{h}^t \cdot \boldsymbol{\sigma}^t) + \mathbf{B} = \mathbf{0} \quad (2.50)$$

and thus we identify the corresponding Eshelby stress tensor $\boldsymbol{\Sigma}^t$ and the volume force \mathbf{B} as

$$\boldsymbol{\Sigma}^t = W\mathbf{I} - \mathbf{h}^t \cdot \boldsymbol{\sigma}^t \quad \text{and} \quad \mathbf{B} = -\mathbf{h}^t \cdot \mathbf{b} - \partial_{\mathbf{x}} W \quad (2.51)$$

The weak form and the discretization applies in an analog manner to the geometrically non-linear case as given in the previous sections, so that it is not necessary to repeat it here.

In the next section we discuss the numerical performance and reliability of the proposed Material Force Method in a first example for a straight crack in a geometrically linear but non-linear elastic Ramberg-Osgood type material. The second example discusses the kinking behaviour of a straight crack in a geometrically non-linear setting under mixed mode loading.

2.6 Examples

2.6.1 Crack in a Ramberg-Osgood material

For comparison purposes, we consider a geometrically linear setting of a ‘Modified Boundary Layer’-formulation (MBL-formulation) [81] of a straight, traction free crack in a nonlinear elastic material of the Ramberg-Osgood type. Thereby the one-dimensional stress-strain relation is given by

$$\frac{\epsilon}{\epsilon_0} = \frac{\sigma}{\sigma_0} + \alpha \left[\frac{\sigma}{\sigma_0} \right]^n \quad (2.52)$$

whereby σ_0 and ϵ_0 are the ‘yield’ stress and strain, respectively, $n > 1$ is the strain hardening exponent and α is a dimensionless material constant. The first term of the right hand side describes a linear elastic material behaviour with a Young’s modulus $E = \sigma_0/\epsilon_0$ whereas the second part provides a nonlinear response. Although eq. 2.52 describes a nonlinear elastic material behaviour, it is often misleadingly addressed as a (deformation) ‘plasticity’ model. A 3d generalization of this model is given in appendix B. The MBL-formulation is based on an isolated treatment of the crack tip region which is independent of the surrounding specimen, see fig. 2.10a & b. Under ‘Small Scale Yielding’ (SSY) conditions this region is chosen in such a way that a small crack tip ‘yield’ zone, dominated by the nonlinear part of eq. 2.52, is surrounded by a large elastic boundary layer mainly controlled by the elastic part of eq. 2.52. We define the ‘yield’ or ‘plastic’

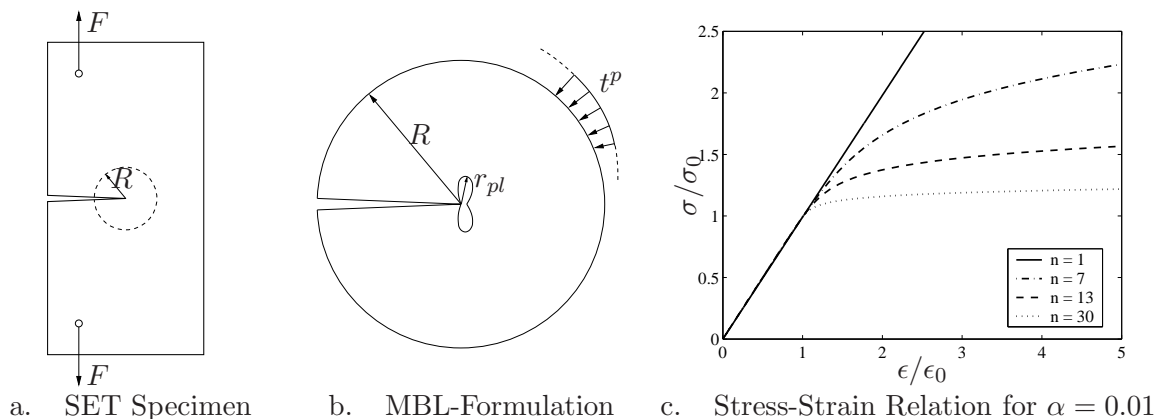


Figure 2.10. Single Edged Tension specimen, equivalent MBL-formulation and Ramberg-Osgood stress-strain relation for $\alpha = 0.01$

zone near the crack tip by that region where the equivalent von Mises stress σ_v exceeds the ‘yield’ stress σ_0 .

In this work, we apply the first two terms of the asymptotic linear elastic stress series near a crack tip given by Williams [108] as

$$\boldsymbol{\sigma} = \frac{K_I}{\sqrt{2\pi r}} \mathbf{f}(\theta) + T \mathbf{e}_1 \otimes \mathbf{e}_1. \quad (2.53)$$

Here K_I denotes the stress intensity factor, T the T -stress which is a uniform normal stress acting parallel to the crack faces and $\mathbf{f}(\theta)$ are given functions depending only on the angle θ measured counterclockwise from the positive x -axis. In all simulations, we kept K_I constant and varied the T -stress. Under SSY-conditions, the linear elastic relation for the J -integral

$$J_{appl} = K_I^2 / E' \quad (2.54)$$

with $E' = E/[1 - \nu^2]$ for plane strain holds. To ensure SSY-conditions in the MBL-formulation we discretized a circular area around the crack tip with a radius R at least 50 times larger than the maximum size of the ‘plastic’ zone.

As known from the classical HRR-solution [36, 82], the singular strain field $\boldsymbol{\epsilon} \propto r^{-n/[n+1]}$ near the crack tip can be approximated by special crack tip elements derived from second order serendipity elements which covers a combination of $1/\sqrt{r}$ and $1/r$ terms, see Barsoum [8]. The ‘plastic’ zone is discretized by approximately 8 second order serendipity finite elements along the ligament.

We varied the T -stress in the range of $\tau = T/\sigma_0 = \pm 0.1, 0.3, 0.5, 0.7, 0.9$ as the hardening parameter we choose $n = 1, 7, 13, 30$ and set the material parameter $\alpha = 0.01$. The resulting one-dimensional stress-strain behaviour defined by eq. 2.52 is shown in fig. 2.10c. Since the T -stress has no influence on the value of the J -integral as shown by Rice [81] this was used as a benchmark to check the accuracy of the J -integral within the numerical

evaluation.

Discussion of the deformation near the crack tip and plastic zones

Although there is no influence of the T -stress on the J -integral, the deformation near the crack tip and especially the size and shape of the ‘plastic’ zone is strongly controlled by this quantity. The deformation behaviour is depicted in fig. 2.11 and the ‘plastic’ zones are shown in fig. 2.12².

To quantify the influence of the T -stress on the deformation behaviour, the crack tip opening displacement δ_t (CTOD) introduced by Tracy [103] was calculated for the hardening parameters $n = 30, 13, 7$ as given in fig. 2.13. There is a significant influence of the T -stress on the crack opening behaviour especially for larger values of n whereas a negative T -stress leads to a larger crack opening in comparison to the equivalent positive T -stress.

The size and shape of the ‘plastic’ zone is strongly driven by the T -stress whereas the hardening exponent n has much less influence. At $\tau = 0$, the maximal expansion of the ‘plastic’ zone is $50 J/\sigma_0$ under an angle of $\theta = 76^\circ$ relative to the ligament. The expansion along the ligament is about $10J/\sigma_0$ and it is $40J/\sigma_0$ perpendicular to the ligament. A negative T -stress leads to an increasing size of the ‘plastic’ zone up to $800J/\sigma_0$ at 55° for $\tau = -0.9$. In contrast to this the expansion of the ‘plastic’ zone along the ligament is almost unaffected by a negative T -stress. Whereas a large positive T -stress $\tau = 0.9$ in combination with a lower hardening parameter, $n = 7$ leads to an additional ‘plastic’ appendix in front of the crack tip. A positive T -stress initially leads to a reduction of the size of the ‘plastic’ zone. At $\tau \approx 0.25$, the maximum expansion $40J/\sigma_0$ could be found under an angle of $\pm 90^\circ$. With increasing T -stress, the size of the ‘plastic’ zone also increases and the maximum expansion is shifted to greater angles. At $\tau = 0.9$, it resides at $\pm 130^\circ$ with a length of $190J/\sigma_0$. Furthermore it is observed that the expansion of the ‘plastic’ zone under an angle of $\pm 90^\circ$ is constant.

An overall negative T -stress leads to a large ‘plastic’ zone which is bent over the ligament. In contrast to this, a positive T -stress causes less extended ‘plastic’ zones which are rotated in the direction of the crack faces.

J -Integral results

For the evaluation of the J -integral within the MBL-formulation under SSY-conditions, we choose 3 different methods. First, we take the single material force acting on the crack tip defined by eq. 2.40. Second, we use the improved material force method defined by

²The distinct vertex which is observed in the base of the deformed crack tip especially for large hardening exponents n is due to the use of the special crack tip elements. In the case we use standard biquadratic triangular finite elements in the vicinity of the crack tip the profile of the deformed crack tip is in good agreement with those of the analytical near field solution, see e.g. [31].

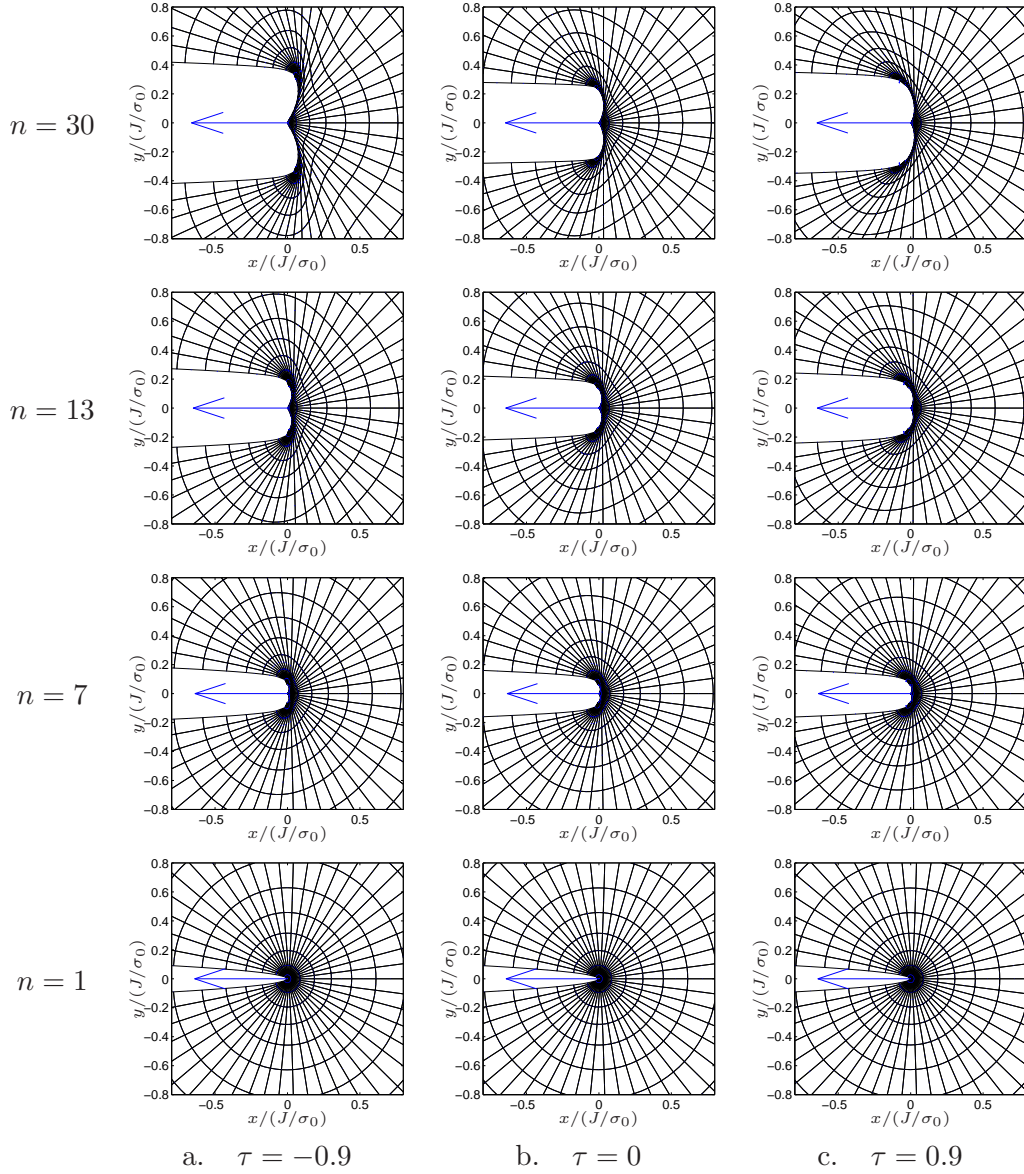


Figure 2.11. Material node forces near the crack tip for different hardening exponents n and T -stresses τ

eq. 3.51 and third, we apply a classical line integral method, see e.g. [86], using Eshelby stresses projected to those nodes defining a circular integration path around the crack tip. The projected nodal Eshelby stress Σ^p is thereby computed by a L_2 -projection, i.e. by minimizing the mean root square error

$$\int_{B_0} \frac{1}{2} [\Sigma^p - \Sigma^h]^2 dV \rightarrow \text{Min} \quad \rightsquigarrow \quad \int_{B_0} \delta \Sigma^p : [\Sigma^p - \Sigma^h] dV = 0 \quad (2.55)$$

with $\Sigma^p|_{B_0^c} = \sum_{n=1}^{n_{en}} N^n \Sigma_n^p$, the shape functions N^n and the non-smooth finite element solution Σ^h and after using a diagonalization technique, we conceptually obtain

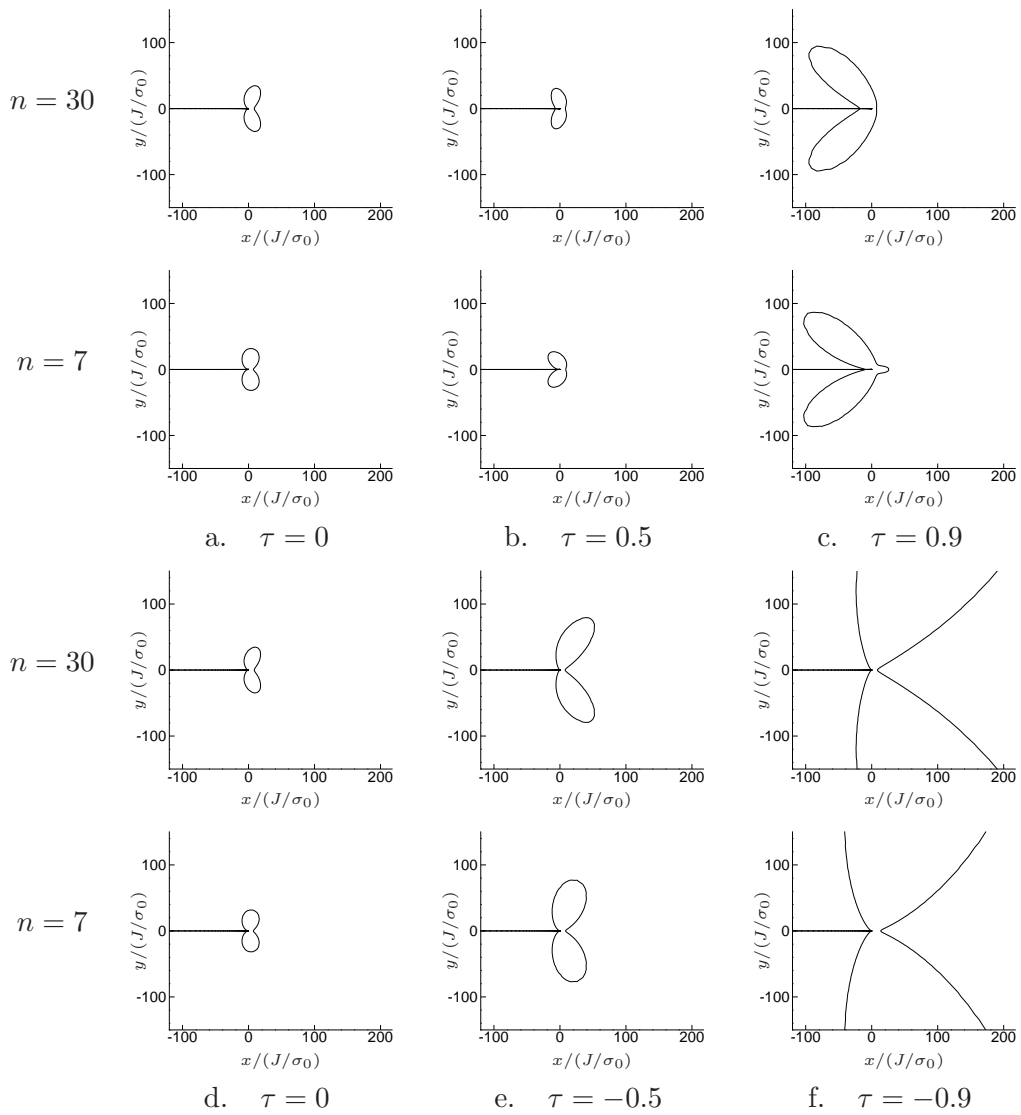


Figure 2.12. 'Plastic' zones near the crack tip for negative and positive T -stresses and hardening parameter $n = 30, 7$.

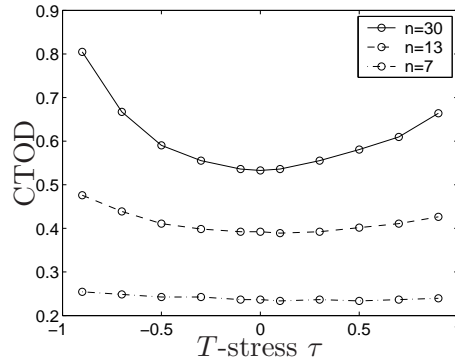


Figure 2.13. Crack tip Opening Displacement (CTOD) for hardening parameter $n = 30, 13, 7$

$$\Sigma_m^p = \left[\mathbf{A}_{e=1}^{n_{el}} \int_{\mathcal{B}_0^e} N^m N^n dV \right]^{-1} \mathbf{A}_{e=1}^{n_{el}} \int_{\mathcal{B}_0^e} N^n \Sigma^h dV. \quad (2.56)$$

The first 15 rings of finite elements which surround the crack tip were selected as the integration domain for the Material Force Method in eq. 2.41. The regular boundary of this domain was chosen as the integration path for the classical line integral method.

The results for the different methods are given in fig. 2.14. It is observed that the J -integral evaluation by the improved Material Force Method renders the most accurate values. The deviation for large T -stress, especially $\tau = \pm 0.9$, is caused by the slightly nonlinear behaviour of the Ramberg-Osgood-Law for $\epsilon < \epsilon_0$ which is controlled by the material parameter α and the hardening exponent n . Secondly the SSY-conditions could only be approximately fulfilled in a finite domain. The single material force acting on the crack tip shows the largest deviation from the applied one but the error is still less than 4%. The reason is that only the elements directly connected to the crack tip are used for its computation and these elements do not capture the correct singular behaviour of the stress and strain field near the crack tip. The classical line integral method based on the projected nodal Eshelby stress typically underestimates the applied J -value by 1% which is caused by the applied projection algorithm. For the special case $n = 1$ (linear elastic material behaviour), the Material Force Method provides results with an error of less than 0.01%.

Next, we studied the dependence of the Material Force Method on the size of the integration domain. We therefore varied the number of rings of finite elements defining the integration domain from 0^3 to 10. It is observed, see fig. 2.15, that the Material Force Method converges within 3 to 4 rings of elements to the applied J -value with an error of less than 0.2% even in the case where we use non singular biquadratic P2 elements in the vicinity of the crack tip.

³⁰ rings of elements is equivalent with the discrete material node point force acting on the crack tip.

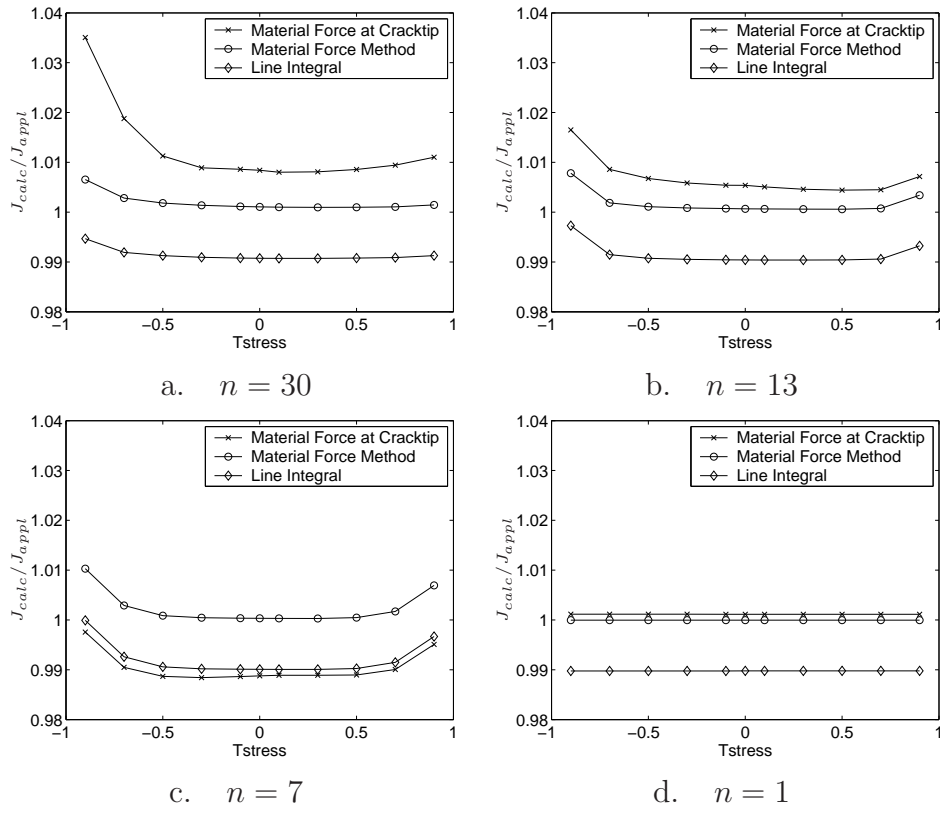


Figure 2.14. J -integral evaluated by different methods.

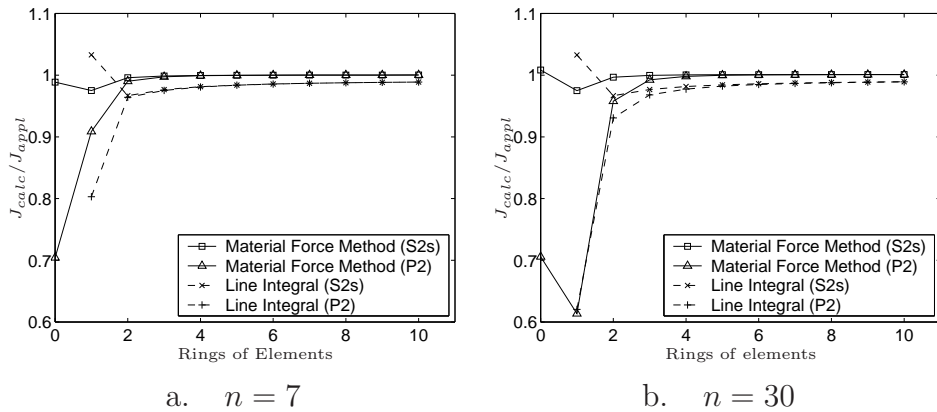


Figure 2.15. Convergence of different J -integral evaluation methods.

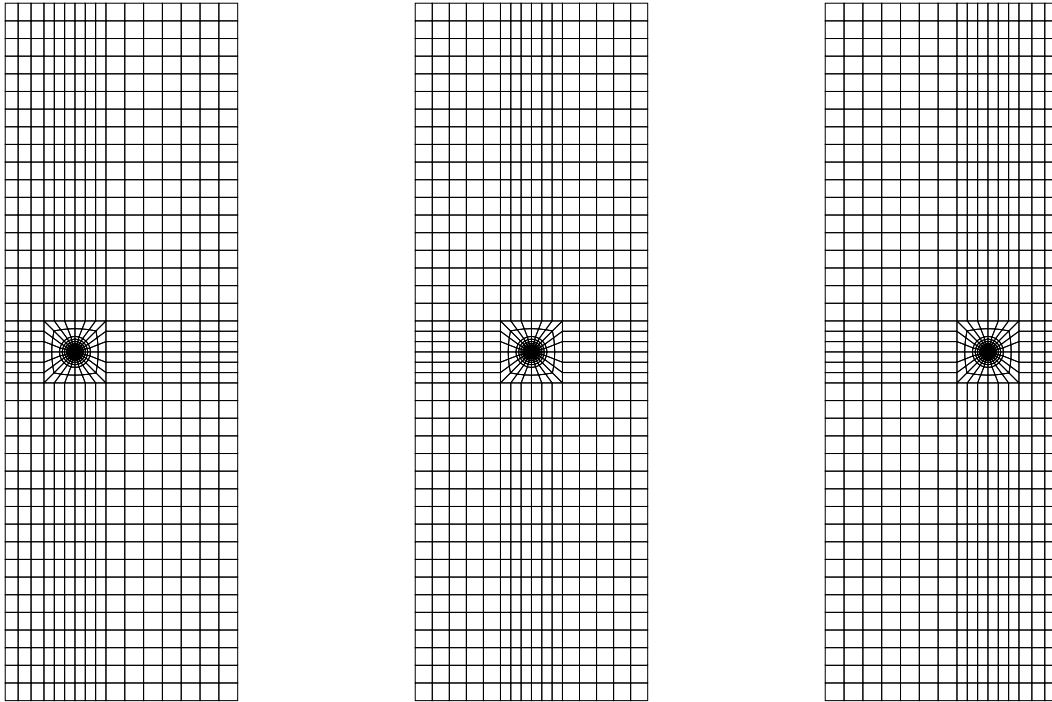


Figure 2.16. Undeformed SET specimen with ratio $a/W = 0.3, 0.5, 0.7$.

2.6.2 Single Edged Tension specimen

In this example study the material forces at a crack tip of a Single Edged Tension specimen (SET). We choose a height to width ratio of $H/W = 3$ and three different ratios of the crack length to width of the specimen $a/W = 0.3, 0.5$ and 0.7 , as shown in fig. 2.16. The specimens are discretized by 1152 biquadratic finite elements and the mesh is strongly refined in the vicinity of the crack tip. The material behaviour is modeled by a compressible Neo-Hooke material with an Young's modulus $E = 72000$ MPa and a Poisson's ratio $\nu = 0.3$. The specimen are loaded at the bottom and top surfaces by a vertical traction load. The corresponding deformed configurations and the calculated discrete material forces are given in fig. 2.17. Although we choose elastic material parameters which roughly belongs to an aluminium alloy, we are aware of the fact that a real aluminium specimen will not undergo these large elastic deformation.

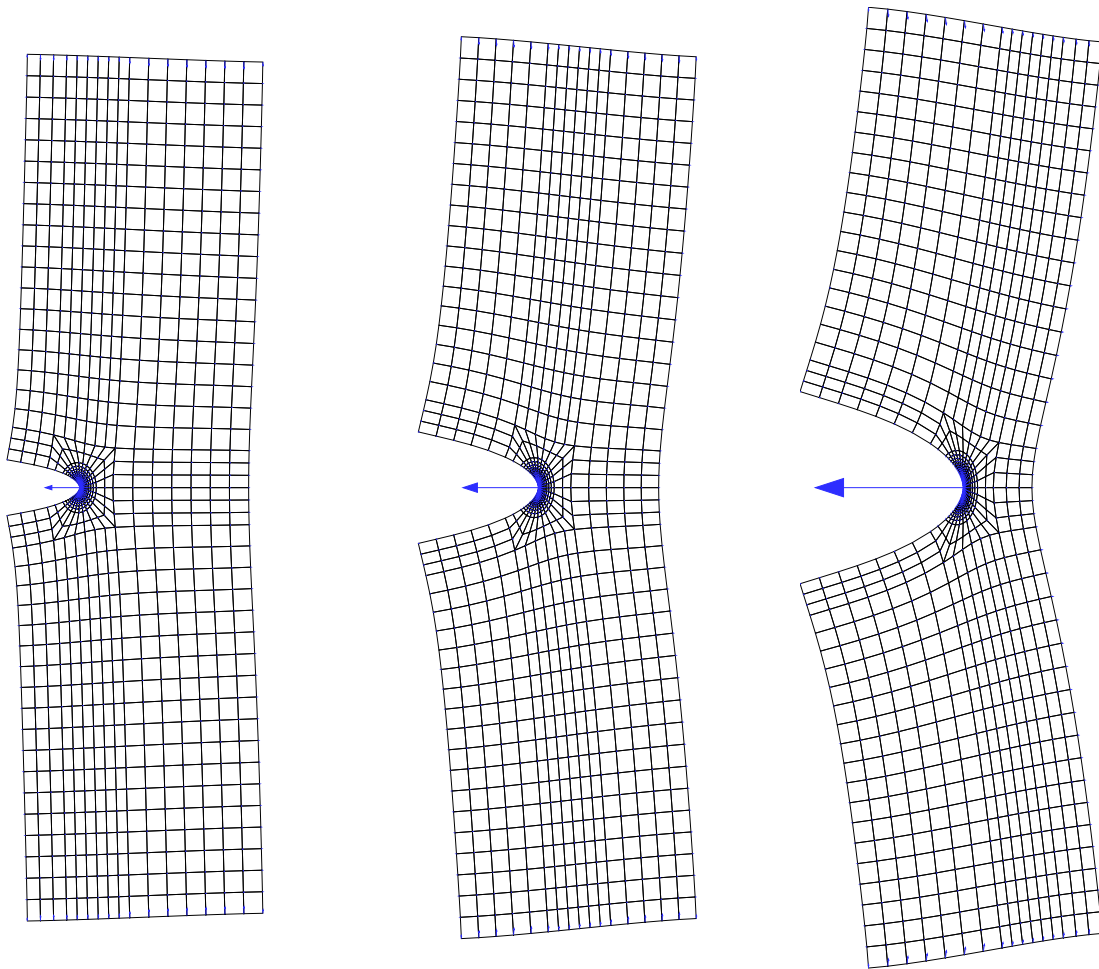


Figure 2.17. Deformed SET specimen with ratio $a/W = 0.3, 0.5, 0.7$.

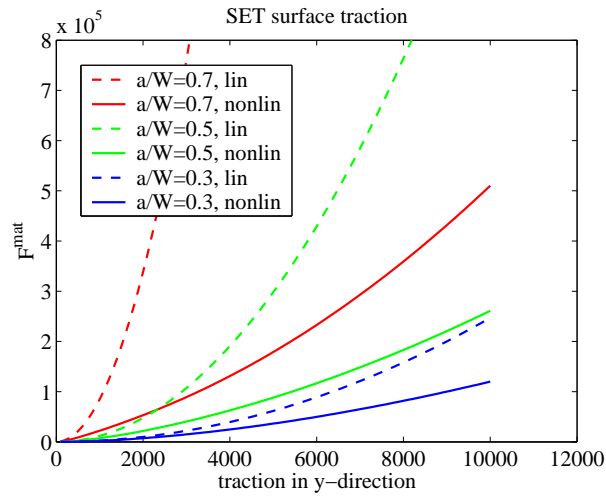


Figure 2.18. Single material force for geometrically linear and nonlinear simulations.

Next we compare the numerical results from the geometrically nonlinear problem with those from the corresponding linear problem, i.e. we use a linear elastic material law. For both cases we calculate the single material force acting at the crack tip with the Material Force Method, see eq. 2.41. As the integration domain we choose the first 20 rings of finite elements starting with the crack tip node. The results for the ratios $a/W = 0.3, 0.5, 0.7$ are illustrated in fig. 2.18. For all three cases the geometrically linear problems overestimates the material force considerably in comparison to the geometrically nonlinear problem.

2.6.3 Crack kinking

Real structures with cracks are frequently subjected to all kind of stresses acting on them simultaneously. Therefore, not only the investigation of cracks exposed to normal stresses (mode I) is of great interest but also the fracture prediction for cracks under superimposed normal and shear loading (mixed mode) or pure shear loading (mode II) is necessary. Under mixed mode load it is observed, that a straight crack changes its path more or less suddenly which is often called crack kinking. This phenomena is widely discussed in the literature. We refer to the classical studies of Cotterell and Rice [19], Leblond [47], Amestoy and Leblond [3] which are based on the asymptotic solution of the stress fields of a curved or kinked crack in a linear elastic body. An other interesting theoretical work for kinking and curving of cracks was published by Gurtin and Podio-Guidugli [33] based on the material force acting at the crack tip. Recently, Adda-Bedia [2] compares the path predictions of kinked cracks in brittle material with experimental findings and we also want to mention the interesting experimental work of Richard [83].

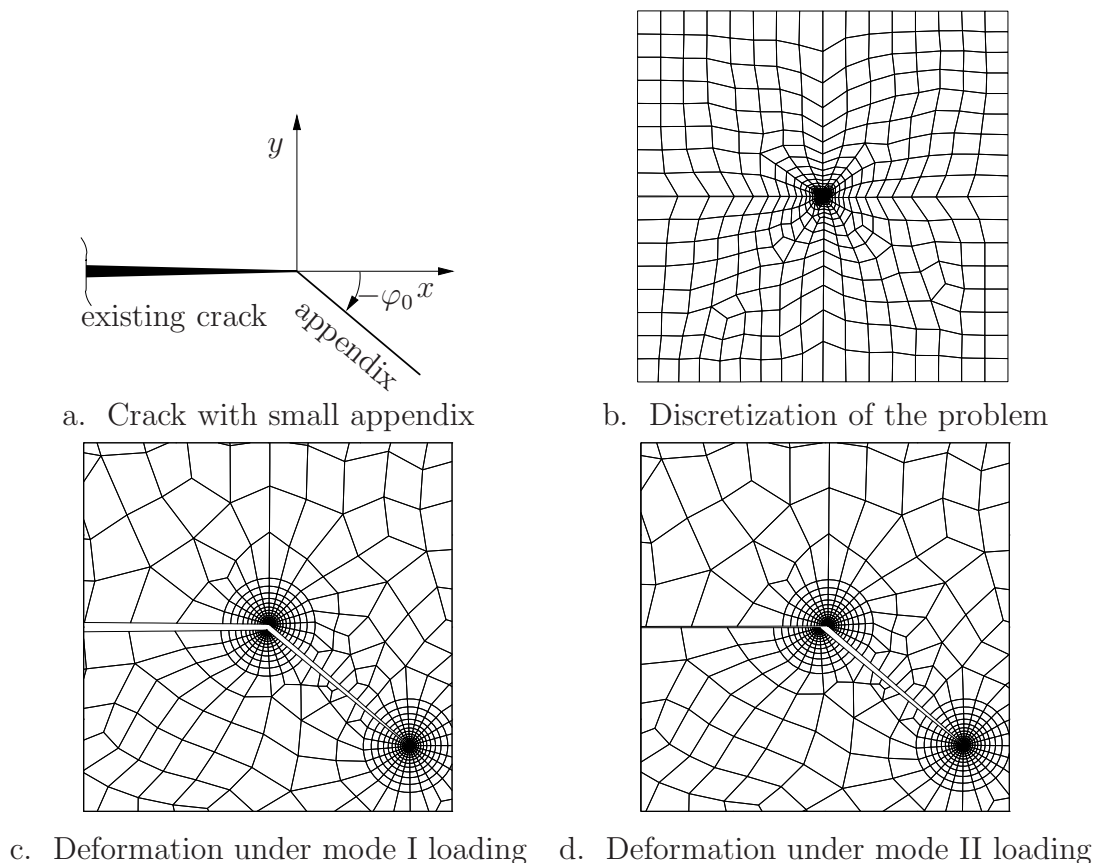


Figure 2.19. Discretization of a kinked crack.

In this section we want to numerically study the influence of a kinked crack under mixed mode load conditions on the single material force acting at the crack tip. A straight

traction free crack is extended by a small appendix crack under a certain angle φ_0 as depicted in fig. 2.19a. The problem is discretized by 1755 S2 elements and 24 P2 elements which are directly connected to the crack tip node as shown in figures 2.19b.–d. The mesh is strongly refined towards the crack tip. The overall dimension of the plate is 200 by 200 whereas the edge length of the elements at the crack tip is 0.03. The length of the appendix l_{apx} is chosen 100 times smaller than the crack length a , i.e. $l_{apx}/a = 1/100$. The deformation behaviour in the vicinity of the kinked crack for mode I and mode II loading and a kink angle of $\varphi_0 = 40^\circ$ can be seen in figures 2.19c. and d.

To ensure mixed mode loading we use again a 'modified boundary layer' formulation and applied the asymptotic stress field of the linear elastic solution of a straight crack as boundary conditions. This reads

$$\mathbf{t}^p = \boldsymbol{\sigma}^{asympt} \cdot \mathbf{n} = \left[\frac{K_I}{\sqrt{2\pi r}} \mathbf{f}_I(\varphi) + \frac{K_{II}}{\sqrt{2\pi r}} \mathbf{f}_{II}(\varphi) \right] \cdot \mathbf{n}$$

where K_I, K_{II} are the Stress Intensity Factor (SIF) for mode I and mode II loading, $\mathbf{f}_I(\varphi), \mathbf{f}_{II}(\varphi)$ are given function and \mathbf{n} is the outer normal of the boundary.

The material is modelled by a geometrically nonlinear compressible Neo-Hooke material with the following stored energy density function W_0

$$W_0 = \frac{\lambda}{2} \ln^2 J + \frac{\mu}{2} [\mathbf{b} - \mathbf{I}] : \mathbf{I} - \mu \ln J \quad (2.57)$$

where λ, μ are the Lamé parameters which are chosen in such a way, that the Young's modulus $E = 71600$ MPa and the Poisson ratio $\nu = 0.33$ is encountered.

The calculated discrete material forces acting at the kinked crack tip for pure mode I, mixed mode ($K_{II}/K_I = 0.5$) and pure mode II loading are given in the figure 2.20 to 2.22. Under mode I loading and a kink angle of $\varphi_0 = 0^\circ$, i.e. a straight crack, the material force is collinear to the ligament of the crack. The more the kink angle varies from the straight crack the more we observe a deviation between the kink direction and the direction of the material force. It seems that the material force wants to 'drive' the kinked crack back to the ligament of the initial crack. This is in agreement with a common crack kink criteria which assumes, that the path taken by the crack to be one for which the local stress field at the tip is of mode I type, i.e. the material force is collinear with the crack path, see Cotterell and Rice [19] or Richard [83]. Additionally we find, that with increasing kink angle the length of the material force decreases.

For mixed mode loading, e.g. we choose $K_{II}/K_I = 0.5$, see fig. 2.21, we see already for the straight crack a relatively large deviation of the kink direction and direction of the material force. This could be interpreted, that the material force tries to kink the crack in a certain direction. With increasing kink angle we find an angle of $\varphi_0 \approx -55^\circ$ where the kink direction and the direction of the material force are collinear. For larger angles the material force shows the tendency to 'drive' the crack back to this direction.

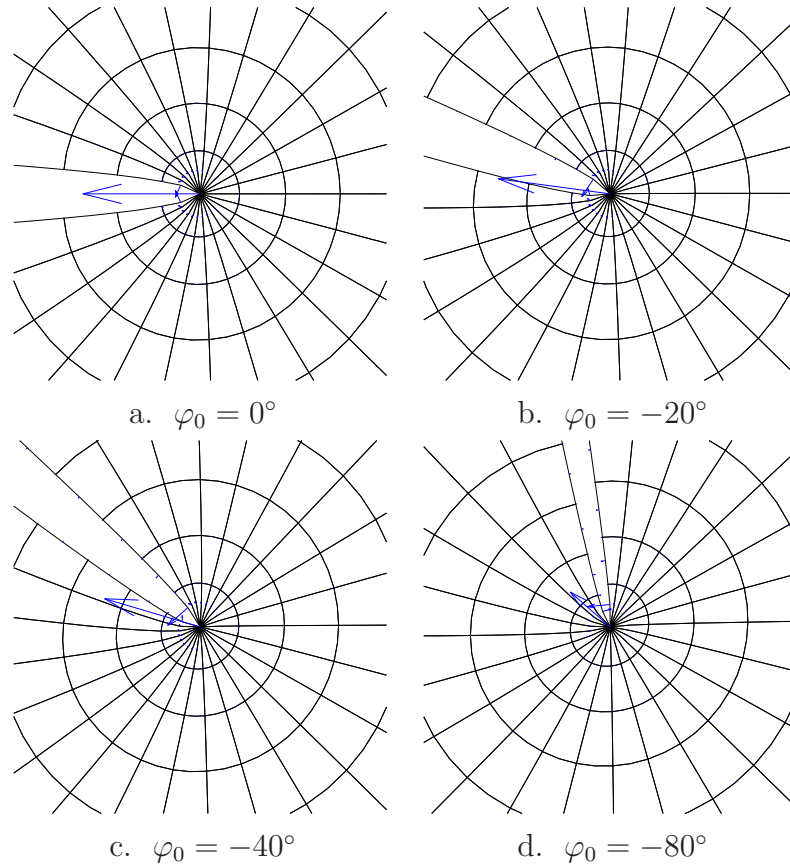


Figure 2.20. Material forces in the vicinity of the kinked crack tip for pure mode I loading.

The results for pure mode II loading are depicted in fig. 2.22. Even for a straight crack the material force shows the clear tendency to 'drive' the crack out of the ligament. This result is in contrast to the geometrically linear theory, see e.g. Richard [83], which predicts no tendency of the vectorial J -integral to kink the crack. We want to critically point out, that a pure mode II deformation mode seems to be physically impossible. The pure mode II is based on the assumption of an antisymmetric displacement field in a symmetrically cracked specimen. But the symmetry of the specimen, at least in a geometrically non-linear sense, must vanish if we apply a antisymmetric displacement field. So the geometrically non-linear theory omits this paradoxon. For a kink angle of $\varphi_0 \approx -76^\circ$ we found the collinear case of the material force and the kink direction, which is in good agreement with experimental results of the kink angle, see e.g. Richard [83].

To interpret the material forces acting at a kinked crack tip more clearly, we introduce a simplified illustration of the results as depicted in fig. 2.23 for various mixed mode loading conditions. We inverted the direction of the calculated material force, so that we graphically see the driving direction. The dashed lines are those directions, were the kink direction and the direction of the material force are collinear.

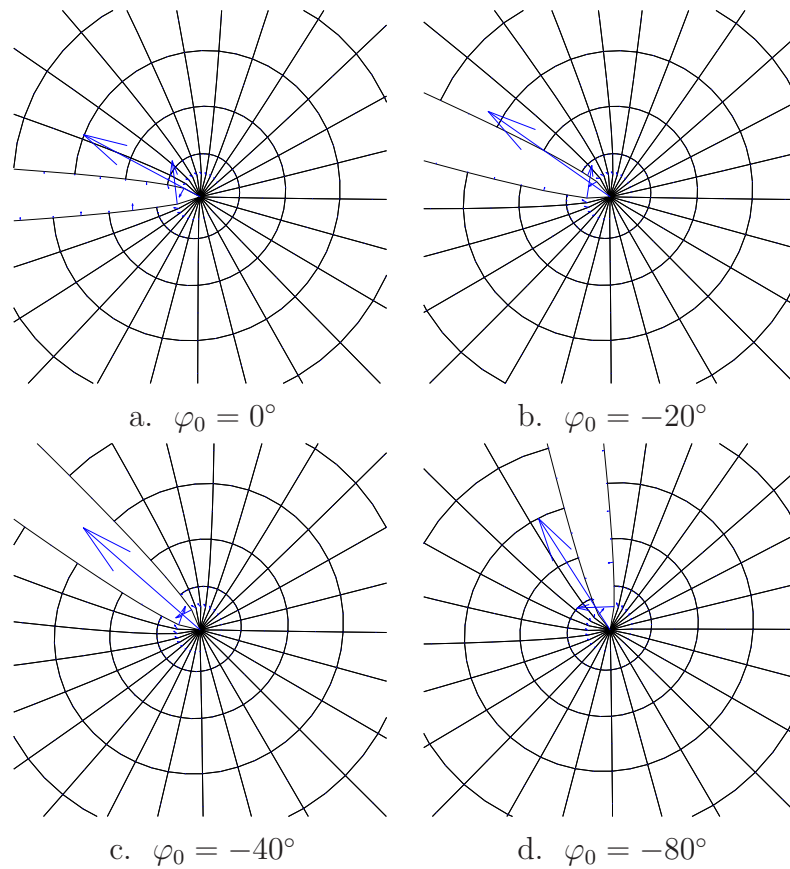


Figure 2.21. Material forces in the vicinity of the kinked crack tip for mixed mode loading ($K_{II}/K_I = 0.5$).

With this results at hand we compare the predicted kink angles by the material force method with some common kink criteria known from the literature, as depicted in fig. 2.24. These are the maximal hoop stress criterion by Erdogan and Shih, the energy density criterion by Shih et al. and a criterion of stress intensity factors for a kinked crack with length $l_{apx} \rightarrow 0$ by Amestoy et al. see e.g. Richard [83] for a discussion. All of them are based on the analytical field solution of the linear fracture mechanics. The results of the material force method for the kinking direction of a crack under mixed mode load are in good agreement with these classical kink criteria.

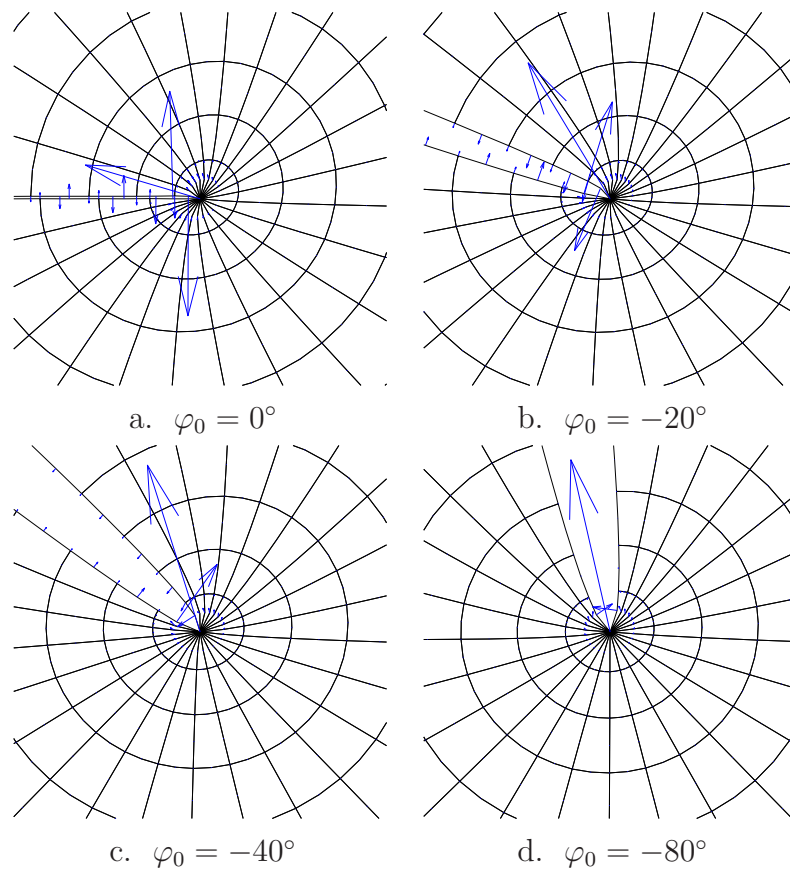


Figure 2.22. Material forces in the vicinity of the kinked crack tip for pure mode II loading.

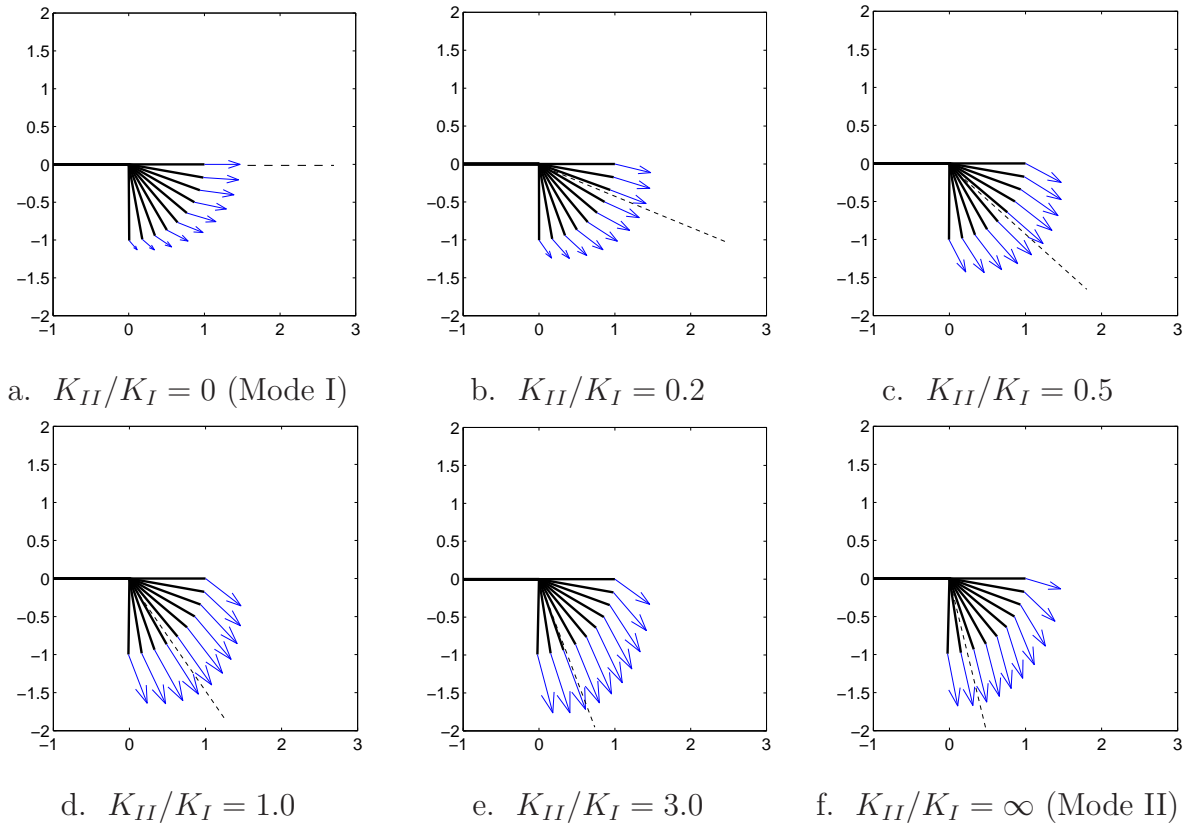


Figure 2.23. Simplified illustration of the material forces acting at a kinked crack tip

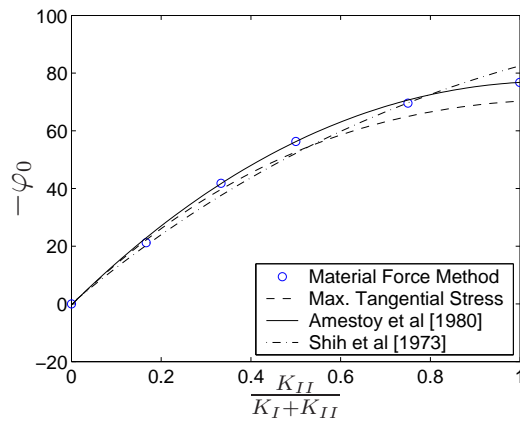


Figure 2.24. Predicted kink angles φ_0 of various criterions

Chapter 3

Thermo-Hyperelasticity

The theoretical and numerical results given in this chapter are based on our work published in [43].

3.1 Kinematics

Because we now take also transient, i.e. time dependent, behaviour into account we shall briefly review the underlying geometrically nonlinear kinematics of the spatial and the material motion problem within this framework. While the classical spatial motion problem is based on the idea of following physical particles from a fixed material position \mathbf{X} through the ambient space, the material motion problem essentially characterizes the movement of physical particles through the ambient material at fixed spatial position \mathbf{x} .

3.1.1 Spatial motion problem

Let \mathcal{B}_0 denote the material configuration occupied by the body of interest at time t_0 . The spatial motion problem is thus characterized through the nonlinear spatial deformation map

$$\mathbf{x} = \varphi(\mathbf{X}, t) : \quad \mathcal{B}_0 \rightarrow \mathcal{B}_t \quad (3.1)$$

assigning the material placement $\mathbf{X} \in \mathcal{B}_0$ of a physical particle to its spatial placement $\mathbf{x} \in \mathcal{B}_t$. The related spatial deformation gradient \mathbf{F}

$$\mathbf{F} = \nabla_{\mathbf{X}} \varphi(\mathbf{X}, t) : \quad T\mathcal{B}_0 \rightarrow T\mathcal{B}_t \quad (3.2)$$

defines the linear tangent map from the material tangent space $T\mathcal{B}_0$ to the tangent space $T\mathcal{B}_t$ while its Jacobian will be denoted as $J = \det \mathbf{F} > 0$. We shall introduce the right Cauchy–Green strain tensor $\mathbf{C} = \mathbf{F}^t \cdot \mathbf{g} \cdot \mathbf{F}$, i.e. the spatial motion pull back of the spatial metric \mathbf{g} as a typical strain measure of the spatial motion problem. In what follows, the material time derivative of an arbitrary quantity $\{\bullet\}$ at fixed material placement \mathbf{X} will be denoted as $D_t\{\bullet\} = \partial_t\{\bullet\}|_{\mathbf{X}}$. Accordingly, the spatial velocity \mathbf{v} can be introduced as

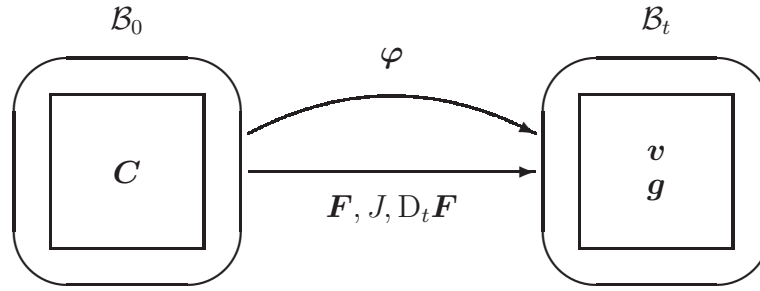


Figure 3.1. Spatial motion problem: Kinematics

the material time derivative of the spatial motion map as $\mathbf{v} = D_t \boldsymbol{\varphi}(\mathbf{X}, t)$. The gradient and the divergence of an arbitrary quantity $\{\bullet\}$ with respect to the material placement will be denoted as $\nabla_{\mathbf{X}}$ and Div , respectively.

3.1.2 Material motion problem

Likewise, let \mathcal{B}_t denote the spatial configuration occupied by the body of interest at time t . Guided by arguments of duality, we can introduce the material deformation map $\boldsymbol{\Phi}$

$$\mathbf{X} = \boldsymbol{\Phi}(\mathbf{x}, t) : \quad \mathcal{B}_t \rightarrow \mathcal{B}_0 \quad (3.3)$$

defining the mapping of the spatial placement of a physical particle $\mathbf{x} \in \mathcal{B}_t$ to its material placement $\mathbf{X} \in \mathcal{B}_0$. Correspondingly, the material deformation gradient \mathbf{f}

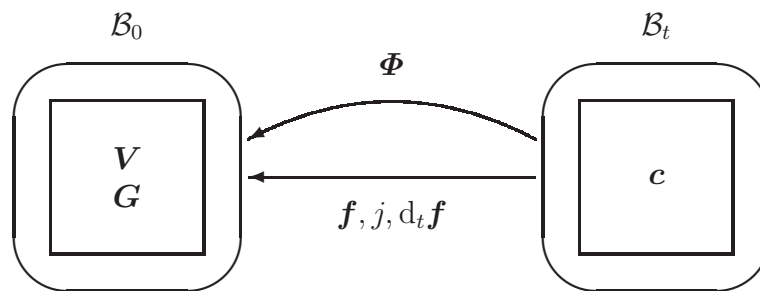


Figure 3.2. Material motion problem: Kinematics

$$\mathbf{f} = \nabla_{\mathbf{x}} \boldsymbol{\Phi}(\mathbf{x}, t) : \quad T\mathcal{B}_t \rightarrow T\mathcal{B}_0 \quad (3.4)$$

defines the related linear tangent map from the spatial tangent space $T\mathcal{B}_t$ to the material tangent space $T\mathcal{B}_0$ with the related material Jacobian $j = \det \mathbf{f} > 0$. In complete analogy to the spatial motion case, we can introduce the material motion right Cauchy

Green strain tensor $\mathbf{c} = \mathbf{f}^t \cdot \mathbf{G} \cdot \mathbf{f}$, i.e. the material motion pull back of the material metric \mathbf{G} . To clearly distinguish between the spatial and the material motion problem, we shall denote the spatial time derivative of a quantity $\{\bullet\}$ at fixed spatial placements \mathbf{x} as $d_t\{\bullet\} = \partial_t\{\bullet\}|_x$. It defines the material velocity \mathbf{V} as the spatial time derivative of the material motion map $\mathbf{V} = d_t\Phi(\mathbf{x}, t)$. Moreover, let ∇_x and div denote the gradient and divergence of an arbitrary quantity $\{\bullet\}$ with respect to the spatial placement.

3.1.3 Spatial vs. material motion kinematics

The spatial and the material motion problem are related through the identity maps in \mathcal{B}_0 and \mathcal{B}_t while the corresponding deformation gradients are simply related via their inverses as $\mathbf{F}^{-1} = \mathbf{f}(\varphi(\mathbf{X}, t), t)$ and $\mathbf{f}^{-1} = \mathbf{F}(\Phi(\mathbf{x}, t), t)$. Moreover, the spatial and the material velocity are related via the following fundamental relations $\mathbf{V} = -\mathbf{f} \cdot \mathbf{v}$ and $\mathbf{v} = -\mathbf{F} \cdot \mathbf{V}$ which can be derived from the total differentials of the spatial and material identity map in a straightforward way, see e.g. Maugin [56] or Steinmann [97]. Recall, that the material and spatial time derivative of any scalar- or vector-valued function $\{\bullet\}$ are related through the Euler theorem as $D_t\{\bullet\} = d_t\{\bullet\} + \nabla_x\{\bullet\} \cdot \mathbf{v}$ and $d_t\{\bullet\} = D_t\{\bullet\} + \nabla_X\{\bullet\} \cdot \mathbf{V}$. Moreover, the material and the spatial time derivative of a volume specific scalar- or vector-valued function $\{\bullet\}_0 = \rho_0\{\bullet\}$ and $\{\bullet\}_t = \rho_t\{\bullet\}$ characterized in terms of the material and spatial density ρ_0 and ρ_t are related through the spatial and material motion version of Reynold's transport theorem as $j D_t\{\bullet\}_0 = d_t\{\bullet\}_t + \text{div}(\{\bullet\}_t \otimes \mathbf{v})$ and $J d_t\{\bullet\}_t = D_t\{\bullet\}_0 + \text{Div}(\{\bullet\}_0 \otimes \mathbf{V})$.

3.1.4 Spatial motion problem

For the spatial motion problem, the balance of momentum balances the rate of change of the spatial momentum $\mathbf{p}_0 = \rho_0 \mathbf{g} \cdot \mathbf{v}$ which is nothing but the material velocity \mathbf{v} weighted by the material density ρ_0 with the momentum flux $\mathbf{\Pi}^t$, i.e. the first Piola-Kirchhoff stress tensor, and the momentum source \mathbf{b}_0 .

$$D_t \mathbf{p}_0 = \text{Div} \mathbf{\Pi}^t + \mathbf{b}_0 \quad (3.5)$$

Recall, that in general, the momentum source \mathbf{b}_0 consists of an external and an internal contribution as $\mathbf{b}_0 = \mathbf{b}_0^{ext} + \mathbf{b}_0^{int}$. The second fundamental balance equation in thermo-mechanics is the balance of energy, which can be stated in the following entropy-based format.

$$\theta D_t S_0 = -\text{Div} \mathbf{Q} + \mathcal{Q}_0 + D_0 - D_0^{con} \quad (3.6)$$

In the above equation, S_0 denotes the material entropy density while \mathbf{Q} and \mathcal{Q}_0 are the material heat flux vector and the material heat source, respectively. Moreover, D_0 denotes the material dissipation power, which can be understood as the sum of a convective and a local part, as $D_0 = D_0^{con} + D_0^{loc}$. Following the standard argumentation in classical rational

thermodynamics, we shall assume the convective part $D_0^{con} = -\mathbf{Q} \cdot \nabla_X \ln \theta \geq 0$ to be non-negative throughout and the local part $D_0^{loc} = 0$ to vanish identically, thus guaranteeing that $D_0 \geq 0$. In what follows, we shall consider a hyperelastic material characterized through the free energy density $\Psi_0 = \Psi_0(\mathbf{F}, \theta; \mathbf{X})$ being a function of the spatial motion deformation gradient \mathbf{F} and the absolute temperature θ with a possible explicit dependence of the material placement \mathbf{X} . The evaluation of the spatial motion version of the Clausius–Planck inequality thus renders the definition of the first Piola–Kirchhoff stress tensor \mathbf{I}^t and the material entropy density S_0 as thermodynamically conjugate variables to the spatial motion deformation gradient \mathbf{F} and the absolute temperature θ . Moreover, it turns out that the internal forces \mathbf{b}_0^{int} of the spatial motion problem vanish identically, compare e.g. Steinmann [97].

$$\mathbf{I}^t = D_{\mathbf{F}} \Psi_0 \quad S_0 = -D_{\theta} \Psi_0 \quad \mathbf{b}_0^{int} = \mathbf{0} \quad (3.7)$$

The material time derivative of the entropy density S_0 can thus be expressed in the following format, $D_t S_0 = D_{\theta} S_0 D_t \theta - D_{\theta} \mathbf{I}^t : D_t \mathbf{F}$. With these results at hand, we can recast the entropy-based balance of energy (3.6) in its more familiar temperature-based format,

$$c_0 D_t \theta = -\text{Div } \mathbf{Q} + \mathcal{Q}_0 + \mathcal{Q}_0^{mech} \quad (3.8)$$

with the specific material heat capacity at constant deformation $c_0 = \theta D_{\theta} S_0$ and the thermomechanical coupling term $\mathcal{Q}_0^{mech} = \theta D_{\theta} \mathbf{I}^t : D_t \mathbf{F}$ which is typically responsible for the so-called Gough–Joule effect.

3.1.5 Material motion problem

Conceptually speaking, the balance of momentum of the material motion problem follows from a complete projection of the classical momentum balance (3.5) onto the material manifold. It balances the time rate of change of the material motion momentum $\mathbf{P}_0 = \rho_0 \mathbf{C} \cdot \mathbf{V}$ with the material motion momentum flux $\boldsymbol{\pi}^t - T_t \mathbf{F}^t$ and momentum source $\mathbf{B}_t + \partial_{\Phi} T_t$.

$$j D_t \mathbf{P}_0 = \text{div} (\boldsymbol{\pi}^t - T_t \mathbf{F}^t) + \mathbf{B}_t + \partial_{\Phi} T_t \quad (3.9)$$

Note, that in the transient case, the classical static material momentum flux $\boldsymbol{\pi}^t$ has to be modified by the correction term $T_t \mathbf{F}^t$ in terms of the kinetic energy density $T_t = \rho_t \mathbf{V} \cdot \mathbf{C} \cdot \mathbf{V} / 2$. Likewise, the material volume force $\mathbf{B}_t = \mathbf{B}_t^{ext} + \mathbf{B}_t^{int}$ which typically consists of an external and an internal contribution contains an additional transient term $\partial_{\Phi} T_t$. The balance of energy of the material motion problem can be stated in the following entropy-based format,

$$j \theta D_t S_0 = -\text{div } \mathbf{q} + \mathcal{Q}_t + D_t - D_t^{con} \quad (3.10)$$

with \mathbf{q} and \mathcal{Q}_t denoting the spatial heat flux vector and heat source, respectively. The spatial dissipation D_t consists of a convective and a local contribution $D_t = D_t^{con} + D_t^{loc}$

with $D_t^{con} = -\mathbf{q} \cdot \nabla_x \ln \theta \geq 0$ and $D_t^{loc} = 0$ vanishing identically, such that $D_t \geq 0$ is a priori guaranteed for the hyperelastic materials considered in the sequel. Next, we introduce the free energy density $\Psi_t = \Psi_t(\mathbf{f}, \theta, \Phi)$ as a function of the material motion deformation gradient \mathbf{f} , the absolute temperature θ and the material placement Φ . The evaluation of the material motion version of the Clausius–Planck inequality according to Steinmann [97] renders the definition of the material motion momentum flux $\boldsymbol{\pi}^t$ as thermodynamically conjugate variable to the material motion deformation gradient \mathbf{f} , the entropy density S_0 as conjugate variable to the temperature θ and a definition of the internal forces \mathbf{B}_t^{int} which are generally different from zero in the material setting.

$$\boldsymbol{\pi}^t = d_{\mathbf{f}} \Psi_t \quad S_0 = -D_\theta \Psi_0 \quad \mathbf{B}_t^{int} = S_t \nabla_X \theta - \partial_{\Phi} \Psi_t \quad (3.11)$$

Similar to the spatial motion problem, the balance of energy (3.10) can be cast into its more familiar temperature–based format

$$c_t D_t \theta = -\operatorname{div} \mathbf{q} + \mathcal{Q}_t + \mathcal{Q}_t^{mech} \quad (3.12)$$

by making use of the above–derived definitions.

3.1.6 Spatial vs. material quantities

While the material motion version of the balance of momentum follows from a complete projection of its spatial motion counterpart onto the material manifold, the material motion version of the balance of energy is simply related to its spatial version through a multiplication with the related jacobian. We can thus set up the following relations between the spatial and material motion momentum and the corresponding flux and source terms.

$$\begin{aligned} \mathbf{P}_0 &= -\mathbf{F}^t \cdot \mathbf{p}_0 \\ \boldsymbol{\pi}^t &= -j \mathbf{F}^t \cdot \boldsymbol{\Pi}^t \cdot \mathbf{F}^t + j \Psi_0 \mathbf{F}^t \\ \mathbf{B}_t &= -j \mathbf{F}^t \cdot \mathbf{b}_0 + j S_0 \nabla_X \theta - j \partial_{\Phi} \Psi_0 \end{aligned} \quad (3.13)$$

The related transformation formulae for the scalar– and vector–valued quantities of the balance of energy simply follow from the appropriate weighting with the jacobian $c_t = j c_0$, $\mathcal{Q}_t = j \mathcal{Q}_0$, $\mathcal{Q}_t^{mech} = j \mathcal{Q}_0^{mech}$, $D_t = j D_0$ and from the corresponding Piola transform as $\mathbf{q} = j \mathbf{Q} \cdot \mathbf{f}^{-t}$.

3.2 Weak form

As a prerequisite for the finite element formulation that will be derived in chapter 3.3, we shall reformulate the balance of momentum and energy in their weak format.

3.2.1 Spatial motion problem

The weak form of the spatial motion problem is based on the global residual statements of the balance of momentum (3.5) and the temperature-based version of the balance of energy (3.8),

$$\begin{aligned} \mathbf{r}^\varphi(\theta, \boldsymbol{\varphi}) &= \mathbf{f}_{dyn}^\varphi - \mathbf{f}_{sur}^\varphi - \mathbf{f}_{vol}^\varphi = \mathbf{0} \\ \mathbf{r}^\theta(\theta, \boldsymbol{\varphi}) &= \mathbf{f}_{dyn}^\theta - \mathbf{f}_{sur}^\theta - \mathbf{f}_{vol}^\theta = 0 \end{aligned} \quad (3.14)$$

whereby the dynamic, the surface and the volume contribution expand in the following expressions.

$$\begin{aligned} \mathbf{f}_{dyn}^\varphi &= \int_{\mathcal{B}_0} D_t \mathbf{p}_0 \, dV & \mathbf{f}_{sur}^\varphi &= \int_{\partial \mathcal{B}_0} \boldsymbol{\Pi}^t \cdot \mathbf{N} \, dA & \mathbf{f}_{vol}^\varphi &= \int_{\mathcal{B}_0} \mathbf{b}_0 \, dV \\ \mathbf{f}_{dyn}^\theta &= \int_{\mathcal{B}_0} c_0 D_t \theta \, dV & \mathbf{f}_{sur}^\theta &= \int_{\partial \mathcal{B}_0} -\mathbf{Q} \cdot \mathbf{N} \, dA & \mathbf{f}_{vol}^\theta &= \int_{\mathcal{B}_0} \mathcal{Q}_0 + \mathcal{Q}_0^{mech} \, dV \end{aligned} \quad (3.15)$$

The residual statements (3.14) are supplemented by appropriate boundary conditions for the mechanical and the thermal fields. For the deformation problem (3.14)₁, the boundary $\partial \mathcal{B}_0$ is decomposed into disjoint parts as $\partial \mathcal{B}_0^\varphi \cup \partial \mathcal{B}_0^t = \partial \mathcal{B}_0$ and $\partial \mathcal{B}_0^\varphi \cap \partial \mathcal{B}_0^t = \emptyset$. Correspondingly, for the temperature problem (3.14)₂, the equivalent decomposition renders the disjoint boundary contributions $\partial \mathcal{B}_0^\theta \cup \partial \mathcal{B}_0^q = \partial \mathcal{B}_0$ and $\partial \mathcal{B}_0^\theta \cap \partial \mathcal{B}_0^q = \emptyset$. Dirichlet boundary conditions are prescribed for the deformation $\boldsymbol{\varphi}$ and the temperature θ on $\partial \mathcal{B}_0^\varphi$ and $\partial \mathcal{B}_0^\theta$, whereas Neumann boundary conditions can be introduced for the momentum flux $\boldsymbol{\Pi}^t$ and the heat flux \mathbf{Q} on $\partial \mathcal{B}_0^t$ and $\partial \mathcal{B}_0^q$ in terms of the outward normal \mathbf{N} .

$$\begin{aligned} \boldsymbol{\varphi} &= \bar{\boldsymbol{\varphi}} & \text{on } \partial \mathcal{B}_0^\varphi & & \boldsymbol{\Pi}^t \cdot \mathbf{N} &= \bar{\mathbf{t}} & \text{on } \partial \mathcal{B}_0^t \\ \theta &= \bar{\theta} & \text{on } \partial \mathcal{B}_0^\theta & & \mathbf{Q} \cdot \mathbf{N} &= \bar{q} & \text{on } \partial \mathcal{B}_0^q \end{aligned} \quad (3.16)$$

By testing the local residual statements corresponding to (3.14)₁ and (3.14)₂ and the related Neumann boundary conditions (3.16)₂ and (3.16)₄ with the vector- and scalar-valued test functions \mathbf{w} and ϑ , respectively, we can derive the corresponding weak forms

$$\begin{aligned} \mathbf{g}^\varphi(\mathbf{w}; \theta, \boldsymbol{\varphi}) &= \mathbf{w}_{dyn}^\varphi + \mathbf{w}_{int}^\varphi - \mathbf{w}_{sur}^\varphi - \mathbf{w}_{vol}^\varphi = 0 & \forall \mathbf{w} & \text{ in } H_1^0(\mathcal{B}_0) \\ \mathbf{g}^\theta(\vartheta; \theta, \boldsymbol{\varphi}) &= \mathbf{w}_{dyn}^\theta + \mathbf{w}_{int}^\theta - \mathbf{w}_{sur}^\theta - \mathbf{w}_{vol}^\theta = 0 & \forall \vartheta & \text{ in } H_1^0(\mathcal{B}_0) \end{aligned} \quad (3.17)$$

provided that the related fields fulfill the necessary smoothness and boundary assumptions. By interpreting the vector-valued test function \mathbf{w} as the spatial virtual displacements $\delta \boldsymbol{\varphi}$, equation (3.17)₁ can be identified as the virtual work expression of the spatial motion problem with the dynamic, the internal, the surface and the volume parts of the virtual work given in the familiar form.

$$\begin{aligned} \mathbf{w}_{dyn}^\varphi &= \int_{\mathcal{B}_0} \mathbf{w} \cdot D_t \mathbf{p}_0 \, dV & \mathbf{w}_{int}^\varphi &= \int_{\mathcal{B}_0} \nabla_X \mathbf{w} : \boldsymbol{\Pi}^t \, dV \\ \mathbf{w}_{sur}^\varphi &= \int_{\partial \mathcal{B}_0^t} \mathbf{w} \cdot \boldsymbol{\Pi}^t \cdot \mathbf{N} \, dA & \mathbf{w}_{vol}^\varphi &= \int_{\mathcal{B}_0} \mathbf{w} \cdot \mathbf{b}_0 \, dV \end{aligned} \quad (3.18)$$

Accordingly, the scalar-valued test function ϑ can be interpreted as the virtual temperature $\delta\theta$. The dynamic, the internal, the surface and the volume contribution to the virtual temperature problem thus expand into the following expressions.

$$\begin{aligned} w_{dyn}^\theta &= \int_{\mathcal{B}_0} \vartheta c_0 D_t \theta \, dV & w_{int}^\theta &= \int_{\mathcal{B}_0} -\nabla_X \vartheta \cdot \mathbf{Q} \, dV \\ w_{sur}^\theta &= \int_{\partial \mathcal{B}_0^q} -\vartheta \mathbf{Q} \cdot \mathbf{N} \, dA & w_{vol}^\theta &= \int_{\mathcal{B}_0} \vartheta [\mathcal{Q}_0 + \mathcal{Q}_0^{mech}] \, dV \end{aligned} \quad (3.19)$$

3.2.2 Material motion problem

Guided by arguments of duality, the global residual statements of the balance of momentum and energy of the material motion problem can be introduced in complete analogy to their spatial motion counterparts.

$$\begin{aligned} \mathbf{R}^\Phi &= \mathfrak{F}_{dyn}^\Phi - \mathfrak{F}_{sur}^\Phi - \mathfrak{F}_{vol}^\Phi = \mathbf{0} \\ R^\theta &= \mathfrak{F}_{dyn}^\theta - \mathfrak{F}_{sur}^\theta - \mathfrak{F}_{vol}^\theta = 0 \end{aligned} \quad (3.20)$$

The dynamic, the surface and the internal contribution to both equations can be expressed in the following form.

$$\begin{aligned} \mathfrak{F}_{dyn}^\Phi &= \int_{\mathcal{B}_t} j D_t \mathbf{P}_0 \, dv & \mathfrak{F}_{sur}^\Phi &= \int_{\partial \mathcal{B}_t} [\boldsymbol{\pi}^t - K_t \mathbf{F}^t] \cdot \mathbf{n} \, da & \mathfrak{F}_{vol}^\Phi &= \int_{\mathcal{B}_t} \mathbf{B}_t + \partial_\Phi K_t \, dv \\ \mathfrak{F}_{dyn}^\theta &= \int_{\mathcal{B}_t} c_t D_t \theta \, dv & \mathfrak{F}_{sur}^\theta &= \int_{\partial \mathcal{B}_t} -\mathbf{q} \cdot \mathbf{n} \, da & \mathfrak{F}_{vol}^\theta &= \int_{\mathcal{B}_t} \mathcal{Q}_t + \mathcal{Q}_t^{mech} \, dv \end{aligned} \quad (3.21)$$

Next, Dirichlet and Neumann boundary conditions can be defined for the material motion problem to illustrate the formal duality with the spatial motion problem. For the balance of momentum (3.20)₁, the corresponding parts of the boundary will be introduced as $\partial \mathcal{B}_t^\Phi \cup \partial \mathcal{B}_t^T = \partial \mathcal{B}_t$ and $\partial \mathcal{B}_t^\Phi \cap \partial \mathcal{B}_t^T = \emptyset$ while for the balance of energy (3.20)₂, they read $\partial \mathcal{B}_t^\theta \cup \partial \mathcal{B}_t^Q = \partial \mathcal{B}_t$ and $\partial \mathcal{B}_t^\theta \cap \partial \mathcal{B}_t^Q = \emptyset$. Accordingly, the corresponding boundary conditions can be expressed in the following form.

$$\begin{aligned} \Phi &= \bar{\Phi} & \text{on } \partial \mathcal{B}_t^\Phi & & [\boldsymbol{\pi}^t - K_t \mathbf{F}^t] \cdot \mathbf{n} &= \bar{\mathbf{T}} & \text{on } \partial \mathcal{B}_t^T \\ \theta &= \bar{\theta} & \text{on } \partial \mathcal{B}_t^\theta & & \mathbf{q} \cdot \mathbf{n} &= \bar{Q} & \text{on } \partial \mathcal{B}_t^Q \end{aligned} \quad (3.22)$$

By testing the pointwise statements of the material momentum and energy balance and the related Neumann boundary conditions with the vector- and scalar-valued test functions \mathbf{W} and ϑ , we obtain the weak forms of the material motion problem.

$$\begin{aligned} \mathbf{G}^\Phi(\mathbf{W}; \theta, \Phi) &= W_{dyn}^\Phi + W_{int}^\Phi - W_{sur}^\Phi - W_{vol}^\Phi = 0 & \forall \mathbf{W} & \text{ in } H_1^0(\mathcal{B}_t) \\ \mathbf{G}^\theta(\vartheta; \theta, \Phi) &= W_{dyn}^\theta + W_{int}^\theta - W_{sur}^\theta - W_{vol}^\theta = 0 & \forall \vartheta & \text{ in } H_1^0(\mathcal{B}_t) \end{aligned} \quad (3.23)$$

Note, that by interpreting the test function \mathbf{W} as the material virtual displacement $\mathbf{W} = \delta\Phi$, equation (3.23)₁ can be interpreted as the material counterpart of the classical virtual work expression (3.17)₁. Accordingly, W_{dyn}^Φ and W_{int}^Φ denote the dynamic and

the internal virtual work, while W_{sur}^Φ and W_{vol}^Φ are the corresponding surface and volume contributions.

$$\begin{aligned} W_{dyn}^\Phi &= \int_{\mathcal{B}_t} \mathbf{W} \cdot j D_t \mathbf{P}_0 \, dv & W_{int}^\Phi &= \int_{\mathcal{B}_t} \nabla_x \mathbf{W} : [\boldsymbol{\pi}^t - K_t \mathbf{F}^t] \, dv \\ W_{sur}^\Phi &= \int_{\partial \mathcal{B}_t^F} \mathbf{W} \cdot [\boldsymbol{\pi}^t - K_t \mathbf{F}^t] \cdot \mathbf{n} \, da & W_{vol}^\Phi &= \int_{\mathcal{B}_t} \mathbf{W} \cdot [\mathbf{B}_t + \partial_{\boldsymbol{\Phi}} K_t] \, dv \end{aligned} \quad (3.24)$$

Furthermore, the dynamic, the internal, the surface and the volume contribution to the weak form of the energy balance (3.23)₂ expand into the following formats.

$$\begin{aligned} W_{dyn}^\theta &= \int_{\mathcal{B}_t} \vartheta c_t D_t \theta \, dv & W_{int}^\theta &= \int_{\mathcal{B}_t} -\nabla_x \vartheta \cdot \mathbf{q} \, dv \\ W_{sur}^\theta &= \int_{\partial \mathcal{B}_t^Q} -\vartheta \mathbf{q} \cdot \mathbf{n} \, da & W_{vol}^\theta &= \int_{\mathcal{B}_t} \vartheta [\mathcal{Q}_t + \mathcal{Q}_t^{mech}] \, dv \end{aligned} \quad (3.25)$$

3.2.3 Spatial vs. material test functions

While the scalar-valued test function ϑ testing the balance of energy is identical for the spatial and the material motion problem, the vector-valued test functions \mathbf{w} and \mathbf{W} are related by the fundamental relations $\mathbf{w} = -\mathbf{W} \cdot \mathbf{F}^t$ and $\mathbf{W} = -\mathbf{w} \cdot \mathbf{f}^t$ which can be verified easily by transforming the virtual work statements of the spatial and the material motion problem (3.17)₂ and (3.23)₂ into one another.

3.2.4 Spatial and material forces

Note, that equations (3.15)₁ define the different contributions to the spatial forces \mathbf{f}^φ representing the traditional forces in the sense of Newton. These are generated by variations relative to the ambient space at fixed material position \mathbf{X} . On the contrary, equations (3.21)₁ define material forces \mathfrak{F}^Φ in the sense of Eshelby which are generated by variations relative to the ambient material at fixed spatial position \mathbf{x} . These material forces represent important measures in the mechanics of material inhomogeneities.

3.2.5 Material Force Method

Recall, that for the spatial motion problem, the surface and the volume contributions to the weak forms (3.17), namely w_{sur}^φ and w_{vol}^φ for the deformation problem and w_{sur}^θ and w_{vol}^θ for the temperature problem typically represent given quantities which define the primary unknowns φ and θ . Once the spatial motion problem is solved, the dynamic term W_{dyn}^Φ , the internal virtual work W_{int}^Φ and the volume contribution W_{vol}^Φ to the material momentum balance can be computed directly. Correspondingly, the material surface forces \mathfrak{F}_{sur}^Φ furnish the primary unknown of the material motion problem. Their numerical evaluation has been advocated as Material Force Method by Steinmann, Ackermann & Barth [99], see also Denzer, Barth & Steinmann [22], Kuhl & Steinmann [46] or Liebe, Denzer & Steinmann [49].

3.3 Discretization

Equations (3.17) and (3.23) define the weak forms of the initial boundary value problem of thermo–hyperelasticity for the spatial and the material motion problem. Traditionally, these equations are first discretized in time, typically with finite difference schemes, before a spatial discretization with the finite element method can be carried out. To this end, consider a partition of the time interval of interest \mathcal{T}

$$\mathcal{T} = \bigcup_{n=0}^{n_{step}-1} [t_n, t_{n+1}] \quad (3.26)$$

and focus on the typical subinterval $[t_n, t_{n+1}]$ whereby $\Delta t = t_{n+1} - t_n$ denotes the corresponding actual time increment. Assume, that the primary unknowns, either the spatial or the material deformation $\boldsymbol{\varphi}_n$ or $\boldsymbol{\Phi}_n$ and the temperature θ_n and all derivable quantities are known at time t_n . In what follows, we shall make use of the classical Euler backward integration scheme to advance the solution in time from the known time step t_n to the actual time step t_{n+1} . Consequently, the first order material time derivatives of the spatial and the material momentum \mathbf{p}_0 and \mathbf{P}_0 and the temperature θ can be approximated in the following way.

$$\begin{aligned} D_t \mathbf{p}_0 &= \frac{1}{\Delta t} [\mathbf{p}_{0n+1} - \mathbf{p}_{0n}] \\ D_t \mathbf{P}_0 &= \frac{1}{\Delta t} [\mathbf{P}_{0n+1} - \mathbf{P}_{0n}] \\ D_t \theta &= \frac{1}{\Delta t} [\theta_{n+1} - \theta_n] \end{aligned} \quad (3.27)$$

Moreover, the governing equations can now be reformulated in terms of the unknown spatial deformation $\boldsymbol{\varphi}_{n+1}$ and the temperature θ_{n+1} at time t_{n+1} for the spatial motion problem

$$\begin{aligned} \mathbf{g}_{n+1}^{\varphi}(\mathbf{w}; \theta_{n+1}, \boldsymbol{\varphi}_{n+1}) &= \mathbf{w}_{dyn}^{\varphi} + \mathbf{w}_{int}^{\varphi} - \mathbf{w}_{sur}^{\varphi} - \mathbf{w}_{vol}^{\varphi} = 0 \quad \forall \mathbf{w} \text{ in } H_1^0(\mathcal{B}_0) \\ \mathbf{g}_{n+1}^{\theta}(\vartheta; \theta_{n+1}, \boldsymbol{\varphi}_{n+1}) &= \mathbf{w}_{dyn}^{\theta} + \mathbf{w}_{int}^{\theta} - \mathbf{w}_{sur}^{\theta} - \mathbf{w}_{vol}^{\theta} = 0 \quad \forall \vartheta \text{ in } H_1^0(\mathcal{B}_0) \end{aligned} \quad (3.28)$$

and in terms of the material deformation $\boldsymbol{\Phi}_{n+1}$ and the temperature θ_{n+1} for the material motion problem.

$$\begin{aligned} \mathbf{G}_{n+1}^{\theta}(\vartheta; \theta_{n+1}, \boldsymbol{\Phi}_{n+1}) &= \mathbf{W}_{dyn}^{\theta} + \mathbf{W}_{int}^{\theta} - \mathbf{W}_{sur}^{\theta} - \mathbf{W}_{vol}^{\theta} = 0 \quad \forall \vartheta \text{ in } H_1^0(\mathcal{B}_t) \\ \mathbf{G}_{n+1}^{\Phi}(\mathbf{W}; \theta_{n+1}, \boldsymbol{\Phi}_{n+1}) &= \mathbf{W}_{dyn}^{\Phi} + \mathbf{W}_{int}^{\Phi} - \mathbf{W}_{sur}^{\Phi} - \mathbf{W}_{vol}^{\Phi} = 0 \quad \forall \mathbf{W} \text{ in } H_1^0(\mathcal{B}_t) \end{aligned} \quad (3.29)$$

The semi–discrete weak forms (3.28) and (3.29) lend themselves readily for the spatial discretization within the finite element framework which will be illustrated in the following sections.

3.3.1 Spatial motion problem

Let \mathcal{B}_0 denote the region occupied by the reference configuration of a solid continuum body at time $t = t_0$. In the spirit of the finite element method, this reference domain is discretized in n_{el} elements \mathcal{B}_0^e . The underlying geometry \mathbf{X} is interpolated elementwise by the shape functions N_X^i in terms of the discrete node point positions \mathbf{X}_i of the $i = 1..n_{en}$ element nodes.

$$\mathcal{B}_0 = \bigcup_{e=1}^{n_{el}} \mathcal{B}_0^e \quad \mathbf{X}^h|_{\mathcal{B}_0^e} = \sum_{i=1}^{n_{en}} N_X^i \mathbf{X}_i \quad (3.30)$$

According to the isoparametric concept, we shall interpolate the unknowns $\boldsymbol{\varphi}$ and θ on the element level with the same shape functions N_φ^i and N_θ^j as the element geometry \mathbf{X} . In the spirit of the classical Bubnov–Galerkin technique, similar shape functions are applied to interpolate the test functions \mathbf{w} and ϑ .

$$\begin{aligned} \mathbf{w}^h|_{\mathcal{B}_0^e} &= \sum_{i=1}^{n_{en}} N_\varphi^i \mathbf{w}_i \in H_1^0(\mathcal{B}_0) & \boldsymbol{\varphi}^h|_{\mathcal{B}_0^e} &= \sum_{k=1}^{n_{en}} N_\varphi^k \boldsymbol{\varphi}_k \in H_1(\mathcal{B}_0) \\ \vartheta^h|_{\mathcal{B}_0^e} &= \sum_{j=1}^{n_{en}} N_\theta^j \vartheta_j \in H_1^0(\mathcal{B}_0) & \theta^h|_{\mathcal{B}_0^e} &= \sum_{l=1}^{n_{en}} N_\theta^l \theta_l \in H_1(\mathcal{B}_0) \end{aligned} \quad (3.31)$$

The related gradients of the test functions $\nabla_X \mathbf{w}^h$ and $\nabla_X \vartheta^h$ and the gradients of the primary unknowns $\nabla_X \boldsymbol{\varphi}^h$ and $\nabla_X \theta^h$ thus take the following elementwise interpolation.

$$\begin{aligned} \nabla_X \mathbf{w}^h|_{\mathcal{B}_0^e} &= \sum_{i=1}^{n_{en}} \mathbf{w}_i \otimes \nabla_X N_\varphi^i & \nabla_X \boldsymbol{\varphi}^h|_{\mathcal{B}_0^e} &= \sum_{k=1}^{n_{en}} \boldsymbol{\varphi}_k \otimes \nabla_X N_\varphi^k \\ \nabla_X \vartheta^h|_{\mathcal{B}_0^e} &= \sum_{j=1}^{n_{en}} \vartheta_j \nabla_X N_\theta^j & \nabla_X \theta^h|_{\mathcal{B}_0^e} &= \sum_{l=1}^{n_{en}} \theta_l \nabla_X N_\theta^l \end{aligned} \quad (3.32)$$

Recall, that herein, $\nabla_X \boldsymbol{\varphi}^h|_{\mathcal{B}_0^e}$ denotes the discrete spatial deformation gradient as $\mathbf{F}^h|_{\mathcal{B}_0^e} = \nabla_X \boldsymbol{\varphi}^h|_{\mathcal{B}_0^e}$. With the above–suggested discretizations in time and space, the fully discrete algorithmic balance of momentum and energy of the spatial motion problem takes the following format.

$$\begin{aligned} \mathbf{r}_I^{\varphi h}(\theta_{n+1}^h, \boldsymbol{\varphi}_{n+1}^h) &= \mathbf{f}_{dyn I}^{\varphi h} + \mathbf{f}_{int I}^{\varphi h} - \mathbf{f}_{sur I}^{\varphi h} - \mathbf{f}_{vol I}^{\varphi h} = \mathbf{0} & \forall I = 1, n_{np} \\ \mathbf{r}_J^{\theta h}(\theta_{n+1}^h, \boldsymbol{\varphi}_{n+1}^h) &= \mathbf{f}_{dyn J}^{\theta h} + \mathbf{f}_{int J}^{\theta h} - \mathbf{f}_{sur J}^{\theta h} - \mathbf{f}_{vol J}^{\theta h} = 0 & \forall J = 1, n_{np} \end{aligned} \quad (3.33)$$

Herein, the discrete inertia forces, the internal forces, the surface forces and the volume forces can be expressed as

$$\begin{aligned} \mathbf{f}_{dyn I}^{\varphi h} &= \mathbf{A} \int_{\mathcal{B}_0^e} N_\varphi^i \frac{\mathbf{p}_{0n+1} - \mathbf{p}_{0n}}{\Delta t} dV & \mathbf{f}_{int I}^{\varphi h} &= \mathbf{A} \int_{\mathcal{B}_0^e} \nabla_X N_\varphi^i \cdot \mathbf{II}_{n+1} dV \\ \mathbf{f}_{sur I}^{\varphi h} &= \mathbf{A} \int_{\partial \mathcal{B}_0^e} N_\varphi^i \bar{\mathbf{t}}_{n+1} dA & \mathbf{f}_{vol I}^{\varphi h} &= \mathbf{A} \int_{\mathcal{B}_0^e} N_\varphi^i \mathbf{b}_{0n+1} dV \end{aligned} \quad (3.34)$$

while the dynamic, the internal, the surface and the volume contribution of the balance of energy expand into the following expressions.

$$\begin{aligned} \mathfrak{f}_{dynJ}^{\theta h} &= \mathbf{A}_{e=1}^{n_{el}} \int_{\mathcal{B}_0^e} N_{\theta}^j c_0 \frac{\theta_{n+1} - \theta_n}{\Delta t} dV & \mathfrak{f}_{intJ}^{\theta h} &= \mathbf{A}_{e=1}^{n_{el}} \int_{\mathcal{B}_0^e} \nabla_X N_{\theta}^j \cdot \mathbf{Q}_{n+1} dV \\ \mathfrak{f}_{surJ}^{\theta h} &= \mathbf{A}_{e=1}^{n_{el}} \int_{\partial \mathcal{B}_0^{qe}} -N_{\theta}^j \bar{q}_{n+1} dA & \mathfrak{f}_{volJ}^{\theta h} &= \mathbf{A}_{e=1}^{n_{el}} \int_{\mathcal{B}_0^e} N_{\theta}^j [\mathcal{Q}_{0n+1} + \mathcal{Q}_{0n+1}^{mech}] dV \end{aligned} \quad (3.35)$$

In the above definitions, the operator \mathbf{A} denotes the assembly over all $e = 1, n_{el}$ element contributions at the $i, j = 1, n_{en}$ element nodes to the global node point vectors at all $I, J = 1, n_{np}$ global node points. Equations (3.33) thus represent the coupled nonlinear set of governing equations which is suggested to be solved in a monolithic sense. The corresponding solution procedure in terms of the incremental iterative Newton Raphson scheme is illustrated in the appendix C. Recall, that the discrete spatial surface forces acting on the global node points can be calculated as

$$\mathfrak{f}_{surI}^{\theta h} = \mathbf{A}_{e=1}^{n_{el}} \int_{\mathcal{B}_0^e} N_{\varphi}^i \frac{\mathbf{p}_{0n+1} - \mathbf{p}_{0n}}{\Delta t} + \nabla_X N_{\varphi}^i \cdot \mathbf{\Pi}_{n+1} - N_{\varphi}^i \mathbf{b}_{0n+1} dV \quad (3.36)$$

and are thus energetically conjugate to spatial variations of the node point positions.

3.3.2 Material motion problem

In complete analogy, we can discretize the domain of interest \mathcal{B}_t in n_{el} elements \mathcal{B}_t^e for the material motion problem. Correspondingly, the geometry \mathbf{x} of each element is interpolated from the $i = 1..n_{en}$ node point positions \mathbf{x}_i by the shape functions N_x^i .

$$\mathcal{B}_t = \bigcup_{e=1}^{n_{el}} \mathcal{B}_t^e \quad \mathbf{x}^h|_{\mathcal{B}_t^e} = \sum_{i=1}^{n_{en}} N_x^i \mathbf{x}_i \quad (3.37)$$

By making use of the isoparametric concept, we shall interpolate the primary unknowns Φ and θ with the same shape functions N_{Φ}^i and N_{θ}^j as the element geometry \mathbf{x} . Moreover, the test functions \mathbf{W} and ϑ are discretized with the same shape functions N_{Φ}^i and N_{θ}^j .

$$\begin{aligned} \mathbf{W}^h|_{\mathcal{B}_t^e} &= \sum_{i=1}^{n_{en}} N_{\Phi}^i \mathbf{W}_i \in H_1^0(\mathcal{B}_t) & \Phi^h|_{\mathcal{B}_t^e} &= \sum_{k=1}^{n_{en}} N_{\Phi}^k \Phi_k \in H_1(\mathcal{B}_t) \\ \vartheta^h|_{\mathcal{B}_t^e} &= \sum_{j=1}^{n_{en}} N_{\theta}^j \vartheta_j \in H_1^0(\mathcal{B}_t) & \theta^h|_{\mathcal{B}_t^e} &= \sum_{l=1}^{n_{en}} N_{\theta}^l \theta_l \in H_1(\mathcal{B}_t) \end{aligned} \quad (3.38)$$

Accordingly, the discretization of the gradients of the test functions $\nabla_x \mathbf{W}^h$ and $\nabla_x \vartheta^h$ and the gradients of the primary unknowns $\nabla_x \Phi^h$ and $\nabla_x \theta^h$ takes the following representation.

$$\begin{aligned} \nabla_x \mathbf{W}^h|_{\mathcal{B}_t^e} &= \sum_{i=1}^{n_{en}} \mathbf{w}_i \otimes \nabla_x N_{\Phi}^i & \nabla_x \Phi^h|_{\mathcal{B}_t^e} &= \sum_{k=1}^{n_{en}} \Phi_k \otimes \nabla_x N_{\Phi}^k \\ \nabla_x \vartheta^h|_{\mathcal{B}_t^e} &= \sum_{j=1}^{n_{en}} \vartheta_j \nabla_x N_{\theta}^j & \nabla_x \theta^h|_{\mathcal{B}_t^e} &= \sum_{l=1}^{n_{en}} \theta_l \nabla_x N_{\theta}^l \end{aligned} \quad (3.39)$$

Herein, $\nabla_x \Phi^h$ denotes the discrete material deformation gradient $\mathbf{f}^h|_{\mathcal{B}_t^e} = \nabla_x \Phi^h|_{\mathcal{B}_t^e}$. Consequently, the discrete algorithmic balances of momentum and energy, the material motion counterparts of equations (3.33), take the following representations.

$$\begin{aligned} \mathbf{R}_I^{\Phi h}(\theta_{n+1}^h, \Phi_{n+1}^h) &= \mathfrak{F}_{dyn I}^{\Phi h} + \mathfrak{F}_{int I}^{\Phi h} - \mathfrak{F}_{sur I}^{\Phi h} - \mathfrak{F}_{vol I}^{\Phi h} = \mathbf{0} \quad \forall I = 1, n_{np} \\ \mathbf{R}_J^{\theta h}(\theta_{n+1}^h, \Phi_{n+1}^h) &= \mathfrak{F}_{dyn J}^{\theta h} + \mathfrak{F}_{int J}^{\theta h} - \mathfrak{F}_{sur J}^{\theta h} - \mathfrak{F}_{vol J}^{\theta h} = 0 \quad \forall J = 1, n_{np} \end{aligned} \quad (3.40)$$

The discrete material inertia forces, the internal forces, the surface forces and the volume forces can be expressed as

$$\begin{aligned} \mathfrak{F}_{dyn I}^{\Phi h} &= \mathbf{A} \int_{\mathcal{B}_t^e} N_{\Phi}^i j \frac{\mathbf{P}_{0n+1} - \mathbf{P}_{0n}}{\Delta t} dv & \mathfrak{F}_{int I}^{\Phi h} &= \mathbf{A} \int_{\mathcal{B}_t^e} \nabla_x N_{\Phi}^i \cdot [\boldsymbol{\pi} - K_t \mathbf{F}]_{n+1} dv \\ \mathfrak{F}_{sur I}^{\Phi h} &= \mathbf{A} \int_{\partial \mathcal{B}_t^e} N_{\Phi}^i \bar{\mathbf{T}}_{n+1} da & \mathfrak{F}_{vol I}^{\Phi h} &= \mathbf{A} \int_{\mathcal{B}_t^e} N_{\Phi}^i [\mathbf{B}_t + \partial_{\Phi} K_t]_{n+1} dv \end{aligned} \quad (3.41)$$

while the dynamic, the internal, the surface and the volume contribution of the energy balance take the following format.

$$\begin{aligned} \mathfrak{F}_{dyn J}^{\theta h} &= \mathbf{A} \int_{\mathcal{B}_t^e} N_{\theta}^j c_t \frac{\theta_{n+1} - \theta_n}{\Delta t} dv & \mathfrak{F}_{int J}^{\theta h} &= \mathbf{A} \int_{\mathcal{B}_t^e} \nabla_x N_{\theta}^j \cdot \mathbf{q}_{n+1} dv \\ \mathfrak{F}_{sur J}^{\theta h} &= \mathbf{A} \int_{\partial \mathcal{B}_t^e} N_{\theta}^j \bar{Q}_{tn+1} da & \mathfrak{F}_{vol J}^{\theta h} &= \mathbf{A} \int_{\mathcal{B}_t^e} N_{\theta}^j [\mathcal{Q}_{tn+1} + \mathcal{Q}_{tn+1}^{mech}] dv \end{aligned} \quad (3.42)$$

As a fundamental difference to the spatial motion problem, the Neumann boundary conditions of the material motion problem cannot be considered as given input data. Correspondingly, the discrete material forces acting on the global node points can only be computed in a post processing calculation once the spatial motion problem has been solved. Their definition parallels the definition of the discrete surface forces of the spatial motion problem given in equation (3.36). The discrete material surface forces

$$\mathfrak{F}_{sur I}^{\Phi h} = \mathbf{A} \int_{\mathcal{B}_t^e} N_{\Phi}^i j \frac{\mathbf{P}_{0n+1} - \mathbf{P}_{0n}}{\Delta t} + \nabla_x N_{\Phi}^i \cdot [\boldsymbol{\pi} - K_t \mathbf{F}]_{n+1} - N_{\Phi}^i [\mathbf{B}_t + \partial_{\Phi} K_t]_{n+1} dv \quad (3.43)$$

are thus energetically conjugate to material variations of the node point positions. They are readily computable once the solution to the spatial motion problem has been determined.

Coupled thermo-mechanical problems tend to involve time scales which typically differ by orders of magnitude. Rather than circumventing the problem of potentially ill-conditioned system matrices by making use of staggered solution techniques, we shall consider the balance of momentum (3.33)₁ or (3.40)₁ in a quasi-static sense in the sequel. In other words,

the dynamic contributions which manifest themselves in the $N_\varphi^j[\mathbf{p}_{0n+1} - \mathbf{p}_{0n}]/\Delta t$ term of equation (3.34)₁ and in the $N_{\Phi}^j[\mathbf{P}_{0n+1} - \mathbf{P}_{0n}]/\Delta t$ term of equation (3.41)₁ are assumed to be negligible. Moreover, the dynamic correction to the material motion momentum flux and source, i.e. the $-K_t \mathbf{F}^t$ and the $\partial_{\Phi} K_t$ term in equation (3.41)₂ and (3.41)₄, vanish identically in the quasi-static case.

For the class of quasi-static problems considered in the sequel, the discrete momentum flux $\boldsymbol{\pi}_{n+1}^t$, and the corresponding momentum source \mathbf{B}_{tn+1} that are essentially needed to compute the discrete material node point forces defined in equation (3.43) are related to their spatial motion counterparts $\boldsymbol{\Pi}_{n+1}^t$ and \mathbf{b}_{0n+1} through the following transformation formulae.

$$\begin{aligned}\boldsymbol{\pi}_{n+1}^t &= -j \mathbf{F}_{n+1}^t \cdot \boldsymbol{\Pi}_{n+1}^t \cdot \mathbf{F}_{n+1}^t + j \Psi_{0n+1} \mathbf{F}_{n+1}^t \\ \mathbf{B}_{tn+1} &= -j \mathbf{F}_{n+1}^t \cdot \mathbf{b}_{0n+1} + j S_0 \nabla_X \theta_{n+1} - j \partial_{\Phi} \Psi_{0n+1}\end{aligned}\quad (3.44)$$

3.3.3 Adiabatic thermo-hyperelasticity

Recall, that in general, the computational analysis of adiabatic problems within the spatial setting does not require a \mathcal{C}^0 -continuous interpolation of the temperature field. Since the heat flux \mathbf{Q} and with it a possible explicit dependence on the temperature gradient vanish in the adiabatic case, there is no obvious need to introduce the temperature as a nodal degree of freedom. For the material motion problem, however, the calculation of the material volume forces \mathbf{B}_{tn+1} according to equation (3.44) essentially relies on the temperature gradient $\nabla_X \theta_{n+1}$, irrespective of the incorporation of a heat flux. The above-suggested \mathcal{C}^0 -continuous interpolation of the temperature field is thus mandatory in the context of the material force method.

3.4 Examples

Finally, we turn to the elaboration of the derived thermo-hyperelastic finite element formulation by means of a number of selected examples. To this end, we introduce the following free energy function for thermo-hyperelastic materials,

$$\begin{aligned}\Psi_0 &= \frac{\lambda}{2} \ln^2 J + \frac{\mu}{2} [\mathbf{b} - \mathbf{I}] : \mathbf{I} - \mu \ln J && \text{mechanical part} \\ &- 3\alpha\kappa [\theta - \theta_0] \frac{\ln J}{J} && \text{thermo-mechanical coupling} \\ &+ c_0 [\theta - \theta_0 - \theta \ln \frac{\theta}{\theta_0}] - [\theta - \theta_0] S^\circ && \text{thermal part}\end{aligned}\quad (3.45)$$

whereby the first three terms represent the classical free energy function of Neo-Hooke type characterized through the two Lamé constants λ and μ . The fourth term introduces a thermo-mechanical coupling in terms of the thermal expansion coefficient α weighting the product of the bulk modulus κ and the difference between the current temperature θ and the reference temperature θ_0 . The fifth term finally accounts for the purely thermal

behavior in terms of the specific heat capacity c_0 and the last term defines the absolute entropy density S° at the reference temperature θ_0 . According to the general constitutive equation (3.7), the first Piola–Kirchhoff stress can be derived as thermodynamically conjugate variable to the spatial motion deformation gradient as $\mathbf{\Pi}^t = D_{\mathbf{F}}\Psi_0$ and thus

$$\mathbf{\Pi}^t = [\lambda \ln J - \mu] \mathbf{F}^{-t} + \mu \mathbf{F} - \frac{3\alpha\kappa}{J} [\theta - \theta_0] [1 - \ln J] \mathbf{F}^{-t}. \quad (3.46)$$

Moreover, we assume the material heat flux \mathbf{Q} to obey Fourier’s law

$$\mathbf{Q} = -K_0 \mathbf{G}^{-1} \cdot \nabla_X \theta \quad (3.47)$$

introducing a materially isotropic behavior in terms of the conductivity K_0 , the material metric \mathbf{G} and the material temperature gradient $\nabla_X \theta$. The convective part of the dissipation inequality $D_0^{con} = -\mathbf{Q} \cdot \nabla_X \ln \theta \geq 0$ is thus a priori satisfied for the materially isotropic conductivity being strictly non-negative as $K_0 \geq 0$. With the above definitions at hand, the derivatives of the momentum flux $\mathbf{\Pi}^t$, the resulting thermo–mechanical coupling term \mathcal{Q}_0^{mech} and the heat flux \mathbf{Q} with respect to the deformation gradient \mathbf{F} , the temperature θ and the temperature gradient $\nabla_X \theta$ which are essentially needed to compute the global tangential stiffness matrix according to equation (A3) can be expressed as follows.

$$\begin{aligned} D_{\mathbf{F}} \mathbf{\Pi}^t &= \mu \mathbf{I} \bar{\otimes} \mathbf{I} + \lambda \mathbf{F}^{-t} \otimes \mathbf{F}^{-t} - [\lambda \ln J - \mu] \mathbf{F}^{-t} \underline{\otimes} \mathbf{F}^{-1} \\ D_{\theta} \mathbf{\Pi}^t &= -\frac{3\alpha\kappa}{J} [1 - \ln J] \mathbf{F}^{-t} \\ D_{\mathbf{F}} \mathcal{Q}_0^{mech} &= \theta \frac{3\alpha\kappa}{J^2} [[3 - 2 \ln J] \operatorname{div} \mathbf{v} - [1 - \ln J] D_J(D_t J)] J \mathbf{F}^{-t} \\ D_{\theta} \mathcal{Q}_0^{mech} &= -\frac{3\alpha\kappa}{J} [1 - \ln J] \operatorname{div} \mathbf{v} \\ D_{\nabla_X \theta} \mathbf{Q} &= -K_0 \mathbf{G} \end{aligned} \quad (3.48)$$

The $D_{\mathbf{F}} \mathbf{\Pi}^t$ term of equation (3.48)₁ is typically introduced as the sum of the geometric and the material part of the classical tangential stiffness matrix, where the component representation of the non-standard dyadic products $\bar{\otimes}$ and $\underline{\otimes}$ reads $\{\bullet \bar{\otimes} \circ\}_{ijkl} = \{\bullet\}_{ik} \otimes \{\circ\}_{jl}$ and $\{\bullet \underline{\otimes} \circ\}_{ijkl} = \{\bullet\}_{il} \otimes \{\circ\}_{jk}$. Moreover, we have made use of the following transformation formula $\mathbf{F}^{-t} : D_t \mathbf{F} = \operatorname{div} \mathbf{v}$ in equations (3.48)₃ and (3.48)₄. Recall, that with the temporal discretization based on the traditional Euler backward method as suggested in chapter 3.3, the temperature dependent term $D_J(D_t J)$ of equation (3.48)₃ typically simplifies to $D_J(D_t J) = 1/\Delta t$.

Remark: Isotropic heat flow

Observe, that in the present contribution, we assume the heat flux to be isotropic in the reference configuration as $\mathbf{Q} = -K_0 \mathbf{G}^{-1} \cdot \nabla_X \theta$ or alternatively $\mathbf{q} = -j K_0 \mathbf{b} \cdot \nabla_x \theta$. In the related literature, however, we typically find a spatially isotropic rather than a materially isotropic behavior as $\mathbf{q} = -k_t \mathbf{g}^{-1} \cdot \nabla_x \theta$ which corresponds to an anisotropic behavior in the reference configuration in the context of finite thermo-elasticity as $\mathbf{Q} = -J k_t \mathbf{C}^{-1} \cdot \nabla_X \theta$, see e.g. Miehe [66], [68], Reese & Wriggers [78] or Simo [91].

Remark: Absolute Entropy

We have to introduce an absolute entropy density S° in the free energy function Ψ_0 . Otherwise the definition of the entropy density $S_0 = -D_\theta \Psi_0$ would only represent the change of the entropy in the system and this would lead to internal material forces \mathbf{B}_t^{int} which depend on the reference temperature θ_0 . Because we restrict our analysis in this section to materials with constant specific heat capacity c_0 the change of the temperature has to be moderate. Otherwise we have to address the temperature dependency of the heat capacity.

3.4.1 Bi-material bar

As a first example we consider a bi-material bar under tension with plane strain constraint. The material parameters of the left half of the bar corresponds roughly to steel and are given in the following table.

| | | |
|--|----------------------|---|
| Young's modulus E | 205000 | $\left[\frac{\text{N}}{\text{mm}^2}\right]$ |
| Poisson's Ratio ν | 0.29 | |
| Density ρ_0 | $7.85 \cdot 10^{-3}$ | $\left[\frac{\text{g}}{\text{mm}^3}\right]$ |
| Thermal Expansion Coefficient α | $11.5 \cdot 10^{-6}$ | $\left[\frac{1}{\text{K}}\right]$ |
| Thermal Conductivity K_0 | 0.0498 | $\left[\frac{\text{N}}{\text{msecK}}\right]$ |
| Heat Capacity c_0 | 3.8151 | $\left[\frac{\text{N}}{\text{mm}^2\text{K}}\right]$ |
| Reference Temperature θ_0 | 298 | [K] |
| Absolute Entropy S_{Fe}° | 3.8374 | $\left[\frac{\text{N}}{\text{mm}^2\text{K}}\right]$ |

Whereas the material parameters of the right half corresponds roughly to an Aluminium alloy, which are given below.

| | | |
|--|----------------------|---|
| Young's modulus E | 72000 | $\left[\frac{\text{N}}{\text{mm}^2}\right]$ |
| Poisson's Ratio ν | 0.33 | |
| Density ρ_0 | $2.81 \cdot 10^{-3}$ | $\left[\frac{\text{g}}{\text{mm}^3}\right]$ |
| Thermal Expansion Coefficient α | $23.6 \cdot 10^{-6}$ | $\left[\frac{1}{\text{K}}\right]$ |
| Thermal Conductivity K_0 | 0.130 | $\left[\frac{\text{N}}{\text{msecK}}\right]$ |
| Heat Capacity c_0 | 2.6976 | $\left[\frac{\text{N}}{\text{mm}^2\text{K}}\right]$ |
| Reference Temperature θ_0 | 298 | [K] |
| Absolute Entropy S_{Al}° | 2.9473 | $\left[\frac{\text{N}}{\text{mm}^2\text{K}}\right]$ |

The specimen is discretized by bi-linear Q1-elements. A constant elongation is applied at the left and right end of the bar within a very short first time step $\Delta t = 0.01$ and afterwards the elongation is kept constant. Due to the volatile change of the material

parameters at the interface an inhomogeneous temperature field is induced by the external mechanical load. This results in a heat flux which equalizes the temperature differences within the bar over the time.

To point out the evolution of the material volume forces \mathbf{B}_t we split the discrete material node point (surface) forces \mathfrak{F}_{sur}^h , given by Eq. 3.43, into an internal part

$$\mathfrak{F}_{intI}^{\Phi h} = \mathbf{A} \int_{\mathcal{B}_t^e} \nabla_x N_{\Phi}^i \cdot \boldsymbol{\pi}_{n+1} dv \quad (3.49)$$

and a volume part

$$\mathfrak{F}_{volI}^{\Phi h} = \mathbf{A} \int_{\mathcal{B}_t^e} N_{\Phi}^i \mathbf{B}_{tn+1} dv. \quad (3.50)$$

The computed discrete material node point (surface) forces 'SUR', the internal part 'INT' and the volume part 'VOL' in the vicinity of the interface are depicted in Fig. 3.3 for 3 different times $t = 0.01, 1, 100$. Furthermore the distribution of the relative temperature $\Delta\theta$ is given as contour plots.

After the mechanical load is applied within the first time step ($t = 0.01$) relatively large temperature gradients $\nabla_X \theta_{n+1}$ are observed in the vicinity of the interface which causes material node point volume forces 'VOL'. These vanishes over the time due to the heat flux so that the resulting discrete material node point (surface) forces 'SUR' are dominated by their internal part 'INT'.

3.4.2 Specimen with crack

As a second example we want to discuss a single edged tension specimen typically used in fracture mechanics. The height to width ratio is set to $H/W = 3$ and the ratio of crack length to width is $a/W = 0.5$. The specimen is discretized by bilinear Q1-elements and the mesh is heavily refined around the crack tip. The elements which are connected to the crack tip are P1-elements. The material is modeled with the parameter given in the previous section which roughly corresponds to an Aluminium alloy. A constant symmetric elongation of totally 0.1667% of the height W is applied at the top and bottom of the specimen within the first very short time step $\Delta t = 0.01$. The computed discrete material node point (surface) forces 'SUR', the internal part 'INT', the volume part 'VOL' and the temperature distribution $\Delta\Theta$ in the vicinity of the crack tip are shown in Fig. 3.4.2 at three different time states $t = 0.01, 1, 100$.

Similar to the interface problem we observe a steep temperature gradient $\nabla_X \theta$ after the load is applied within the first time step ($t = 0.01$). This results in large material node point volume forces 'VOL', which decrease over the time due to the heat flux with the specimen.

We now apply our improvement of the Material Force Method for the vectorial J -Integral evaluation, as proposed in [22], which essentially consists of the summation of the material

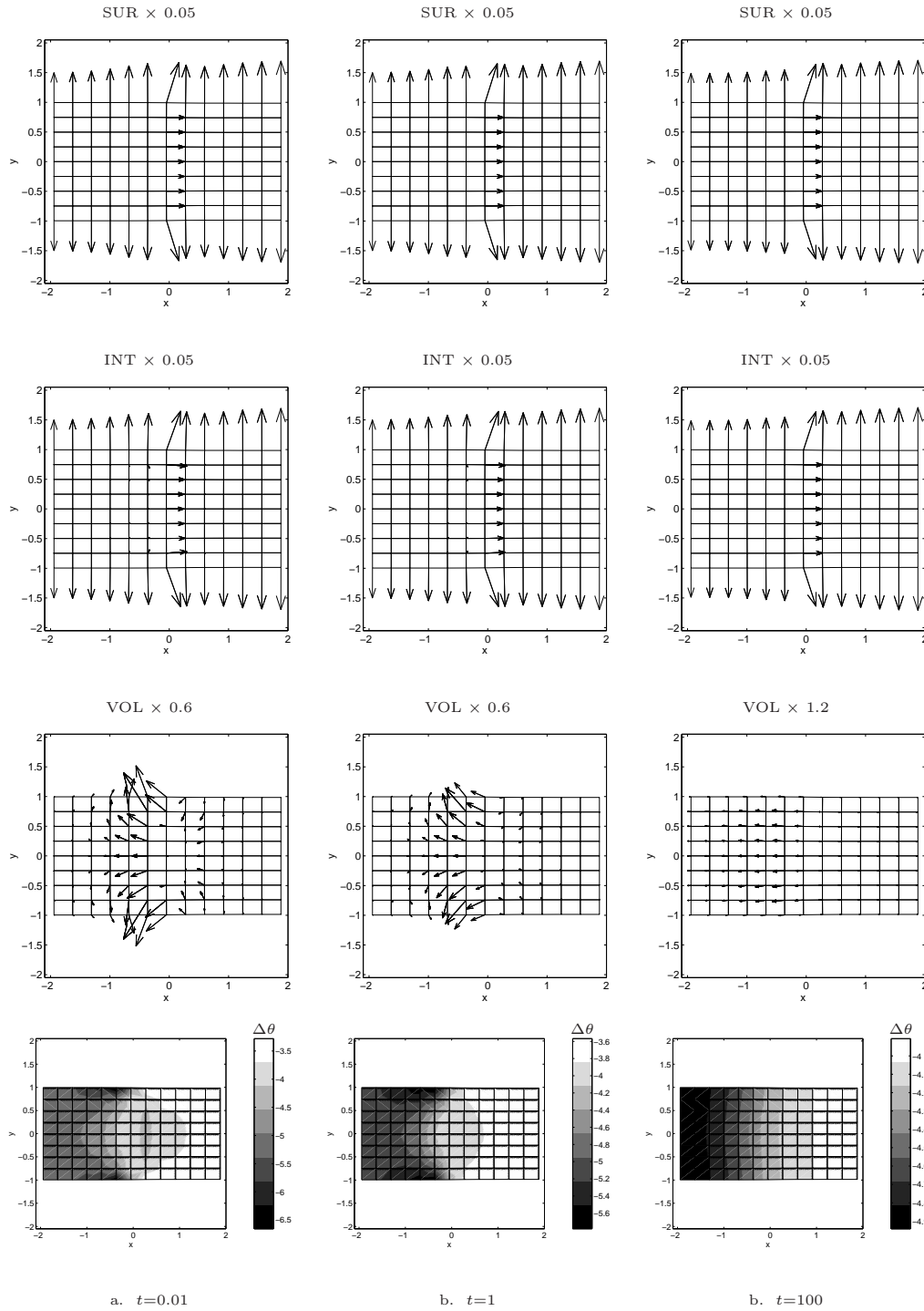


Figure 3.3. Discrete material node point surface, internal and volume forces and temperature distribution in the vicinity of the interface at times $t = 0.01, 1, 100$

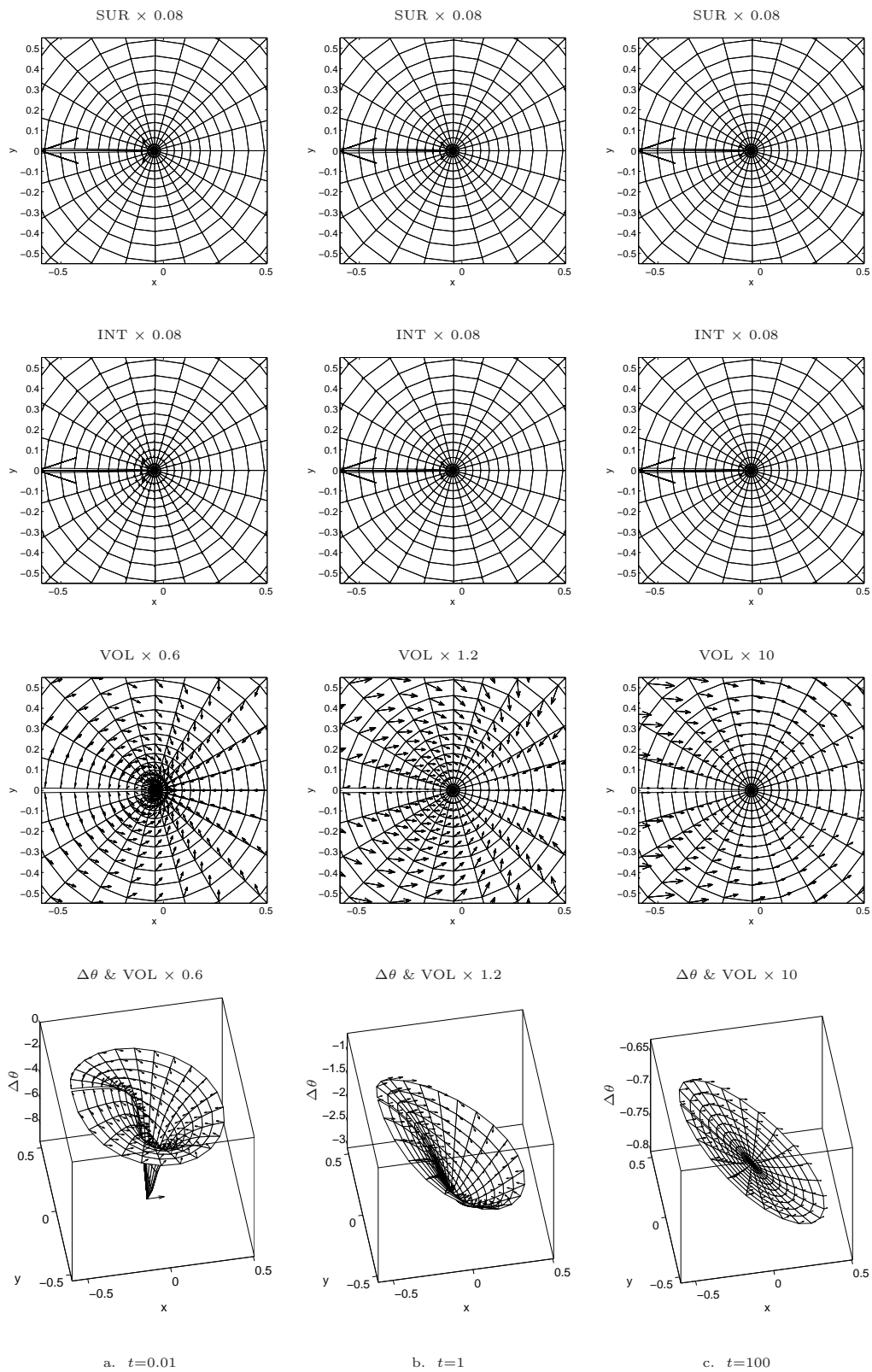


Figure 3.4. Discrete material node point surface, internal and volume forces and temperature distribution in the vicinity of the crack tip at times $t = 0.01, 1, 100$

forces over a given subdomain V_0 enclosing the crack tip, except those which are associated with the regular, i.e. non-singular, part of the boundary ∂V_0^r . This reads

$$-\mathbf{J} = \mathfrak{F}_{sur} = \sum_{i=1}^{\bar{n}_{np}} \mathbf{A}_{e=1}^{n_{el}} \int_{\mathcal{B}_t^e} \nabla_x N_{\phi}^i \cdot \boldsymbol{\pi}_{n+1} - N_{\phi}^i \mathbf{B}_{tn+1} dv. \quad (3.51)$$

where \bar{n}_{np} is the number of all nodes lying in the subdomain $V_0 \setminus \partial V_0^r$.

We also introduce the split of the discrete material node point (surface) force \mathfrak{F}_{sur} into an internal part \mathfrak{F}_{int} and a volume part \mathfrak{F}_{vol} in this case analogous to Eqn. 3.49 and 3.50. As given subdomains for Eq. 3.51 we simply use those subdomains defined by different number of element rings in the vicinity of the crack tip. The resulting material forces for three different times $t = 0.01, 1, 100$ are shown in Fig. 3.5.

Although the internal part \mathfrak{F}_{int} and the volume part \mathfrak{F}_{vol} of the material surface force are domain dependent due to the temperature gradient $\nabla_x \theta$ the resulting material surface force \mathfrak{F}_{sur} behaves domain independent.

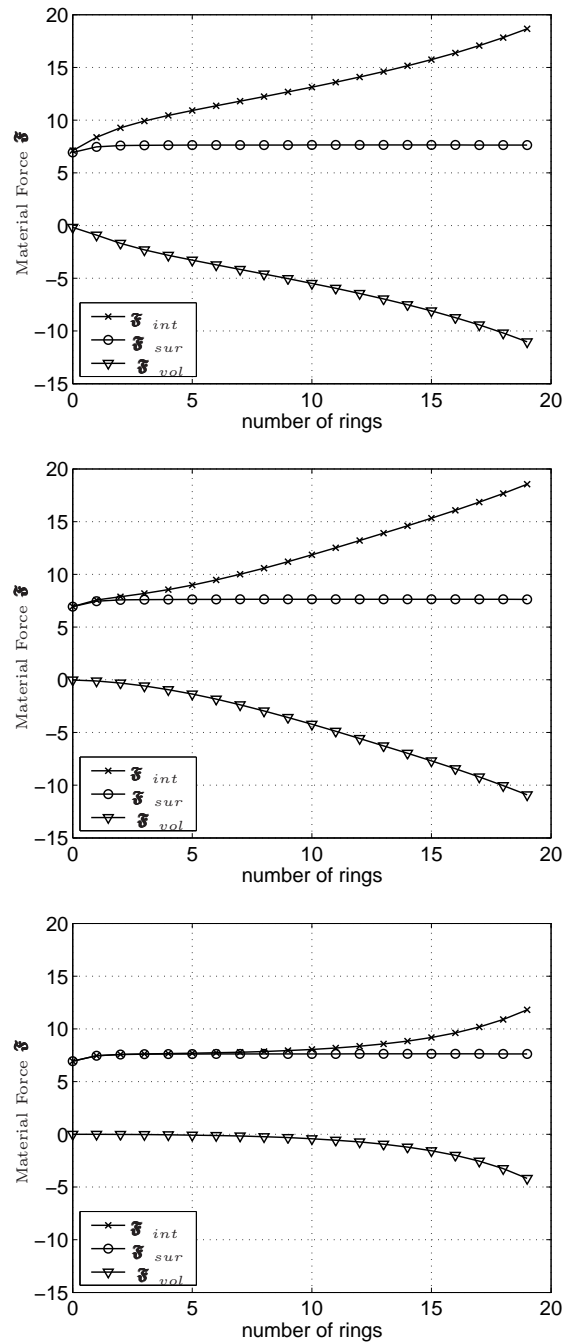


Figure 3.5. Material Forces at different time states $t = 0.01, 1, 100$

Chapter 4

Hyperelasticity Coupled with Damage

For the kinematics and the quasi-static balance of momentum of spatial and material motion problem we refer to chapter 2 and also to our work in [49].

4.1 Hyperelasticity coupled to isotropic damage

In this chapter we present a particular free energy density modelling a hyperelastic constitutive response coupled to isotropic damage. Thereby isotropic damage is characterized by a degradation measure in terms of a scalar damage variable $0 \leq d \leq 1$ that acts as a reduction factor of the local stored energy density of the virgin material $W_0 = JW_t$ per unit volume in \mathcal{B}_0 (or $W_t = jW_0$ per unit volume in \mathcal{B}_t , respectively), which is supposed to be an objective and isotropic function in \mathbf{F} (or \mathbf{f} , respectively). Observe that the familiar constitutive relations of the spatial motion problem are formally dual to the presentation of the appropriate constitutive relations of the material motion problem, see Shield [84], Chadwick [15] and Ericksen [26] for the case of hyperelasticity.

4.1.1 Spatial motion problem

In the case of the spatial motion problem with hyperelasticity coupled to isotropic damage the free energy density ψ_0 is a function of the deformation gradient \mathbf{F} and the internal variable representing damage $\alpha = d(\mathbf{X})$ with possible explicit dependence on the material placement \mathbf{X}

$$\psi_0 = \psi_0(d, \mathbf{F}; \mathbf{X}) = [1 - d]W_0(\mathbf{F}; \mathbf{X}) \quad (4.1)$$

Then, exploiting the Clausius-Duhem inequality $\mathbf{\Pi}^t : D_t \mathbf{F} - D_t \psi_0 \geq 0$ with $D_t \{\bullet\}$ denoting the material time derivative of $\{\bullet\}$, i.e. the time derivative at fixed \mathbf{X} , and assuming the appropriate invariance requirements under superposed spatial rigid body motion being fulfilled, the familiar constitutive equations for the material motion stresses

in \mathcal{B}_0 are given as

$$\mathbf{\Pi}^t = [1 - d] \frac{\partial W_0}{\partial \mathbf{F}} \quad \Longrightarrow \quad \boldsymbol{\sigma}^t = j \mathbf{\Pi}^t \cdot \mathbf{F}^t = [1 - d] \left[W_t \mathbf{I} - \mathbf{f}^t \cdot \frac{\partial W_t}{\partial \mathbf{f}} \right] \quad (4.2)$$

Note that the given format of the spatial motion Cauchy stress $\boldsymbol{\sigma}^t$ is formally comparable to the energy-momentum tensor of Eshelby [29]. Recall that, $W_t = jW_0$ denotes the energy density per unit volume in \mathcal{B}_t . In the case of spatial objectivity, i.e. W_0 is invariant under superposition of spatial rigid body motions, the spatial motion Cauchy stress turns out to be symmetric $\boldsymbol{\sigma}^t = \boldsymbol{\sigma}$.

Furthermore, we introduce the local damage energy release rate Y_0 per unit volume in \mathcal{B}_0 as thermodynamically conjugated to d

$$Y_0 = -\frac{\partial \Psi_0}{\partial d} = W_0 \quad (4.3)$$

Thus it turns out that W_0 is conjugated to the evolution of the independent damage field d . The reduced dissipation inequality reads consequently $\mathcal{D}_0 = Y_0 D_t d \geq 0$. Thus a damage condition is readily motivated as

$$\Phi(Y_0; d) = \phi(Y_0) - d \leq 0 \quad (4.4)$$

with $\phi(\bullet)$ a monotonic function of its argument, see e.g. [90] for the small strain case. Then, based on the postulate of maximum dissipation, an associated damage evolution law is given in terms of a Lagrange multiplier κ

$$D_t d = D_t \kappa \partial_{Y_0} \Phi \quad (4.5)$$

This is complemented by the set of Karush-Kuhn-Tucker loading/unloading conditions

$$\Phi(Y_0; d) \leq 0 \quad \text{and} \quad D_t \kappa \geq 0 \quad \text{and} \quad D_t \kappa \Phi(Y_0; d) = 0 \quad (4.6)$$

Moreover, the consistency condition in the case of loading characterized by $\Phi = 0$ and $D_t \kappa > 0$ allows for the closed form update for the damage parameter

$$D_t \Phi(Y_0; d) = 0 \quad \longrightarrow \quad D_t Y_0 = D_t \kappa \geq 0 \quad \longrightarrow \quad d = \phi(\kappa) \quad (4.7)$$

whereby κ is computed with κ_0 the initial damage threshold from

$$\kappa = \max_{-\infty < s < t} (Y_0(s), \kappa_0) \quad (4.8)$$

Finally, based on the inversion of $\phi(\bullet)$, the damage condition and the Karush-Kuhn-Tucker complementary conditions may be expressed in an alternative format as

$$\varphi(Y_0; \kappa) = Y_0 - \kappa \leq 0 \quad \text{and} \quad D_t d \geq 0 \quad \text{and} \quad D_t d \varphi(Y_0; \kappa) = 0 \quad (4.9)$$

The complementary condition $D_t d \varphi = 0$ may be alternatively stated by decomposition of the total solution domain \mathcal{B}_0 into an inactive elastic and an active damaging domain

$$\mathcal{B}_0^e = \{\mathbf{X} \in \mathcal{B}_0 | \varphi \leq 0, D_t d = 0\} \quad \text{and} \quad \mathcal{B}_0^d = \{\mathbf{X} \in \mathcal{B}_0 | \varphi = 0, D_t d > 0\} \quad (4.10)$$

with the additional completeness and non-overlapping requirements for the solution subdomains

$$\mathcal{B}_0 = \mathcal{B}_0^e \cup \mathcal{B}_0^d \quad \text{and} \quad \emptyset = \mathcal{B}_0^e \cap \mathcal{B}_0^d \quad (4.11)$$

4.1.2 Material motion problem

In the case of the material motion problem with hyperelasticity coupled to isotropic gradient damage the free energy ψ_t is considered as a function of the deformation gradient \mathbf{f} and the damage variable $\alpha = d(\mathbf{x}) = d(\mathbf{X}) \circ \Phi(\mathbf{x})$, whereby the explicit dependence on the material placement is captured by the field $\mathbf{X} = \Phi(\mathbf{x})$

$$\psi_t = \psi_t(d, \mathbf{f}, \Phi(\mathbf{x})) = [1 - d]W_t(\mathbf{f}, \Phi(\mathbf{x})) \quad (4.12)$$

Then, assuming again the appropriate invariance requirements under superposed spatial rigid body motion being fulfilled, the familiar constitutive equations for the macroscopic material stresses in \mathcal{B}_t are given as

$$\Sigma^t = j\pi^t \cdot \mathbf{f}^t = [1 - d] \left[W_0 \mathbf{I} - \mathbf{F}^t \cdot \frac{\partial W_0}{\partial \mathbf{F}} \right] \iff \pi^t = [1 - d] \frac{\partial W_t}{\partial \mathbf{f}} \quad (4.13)$$

Clearly, Σ^t is the so-called Eshelby stress involved in many problems of defect mechanics. Observe carefully that only in the case of material objectivity or rather isotropy, i.e. W_t is invariant under superposition of material rigid body motions, the material motion Cauchy stress turns out to be symmetric $\Sigma^t = \Sigma$.

Here, $W_0 = JW_t$ denotes the energy density per unit volume in \mathcal{B}_0 . The thermodynamic stress of the material motion problem conjugated to the damage variable, corresponds trivially via the Jacobian J to the one of the spatial motion problem, i.e. $Y_t = W_t$ with $Y_0 = JY_t$.

Note that the distributed volume forces as derived in Eq. 4.19 take now the following particular format with respect to the incorporation of damage

$$\mathbf{B}_0 = Y_0 \nabla_X d - \partial_X \psi_0 - \mathbf{F}^t \cdot \mathbf{b}_0 \quad (4.14)$$

4.1.3 Spatial versus material motion problem

Starting from the spatial balance of momentum $\mathbf{o} = \text{Div} \mathbf{\Pi}^t + \mathbf{b}_0$ we perform a covariant pullback to the material manifold. To this end we consider the following identity

$$\mathbf{F}^t \cdot \text{Div} \mathbf{\Pi}^t = \text{Div}(\mathbf{F}^t \cdot \mathbf{\Pi}^t) - \nabla_X \mathbf{F}^t : \mathbf{\Pi}^t. \quad (4.15)$$

Then we assume sufficient smoothness, and recall the integrability conditions for \mathbf{F} , i.e. $\nabla_X \mathbf{F}^t : \mathbf{\Pi}^t = \mathbf{\Pi}^t : \nabla_X \mathbf{F}$. Next by choosing a general internal variable based constitutive assumption for the free energy density per unit volume in \mathcal{B}_0 as

$$\psi_0 = \psi_0(\mathbf{F}, \alpha; \mathbf{X}) \quad (4.16)$$

whereby α denotes an internal variable to be specified together with its conjugated counterpart $A = -\partial_\alpha \psi_0$, the total material gradient in terms of the free energy can be written as

$$\nabla_X \psi_0 = \text{Div}(\psi_0 \mathbf{I}) = \mathbf{\Pi}^t : \nabla_X \mathbf{F} - A \nabla_X \alpha + \partial_{\mathbf{X}} \psi_0 \quad (4.17)$$

With $\partial_{\mathbf{X}} \psi_0$ denoting the explicit material gradient due to material inhomogeneities. Hence assembling terms the following energy-momentum format of the material motion Cauchy-stress (in the sense of Eshelby [29]) holds

$$\mathbf{\Sigma}^t = \psi_0 \mathbf{I} - \mathbf{F}^t \cdot \mathbf{\Pi}^t = \psi_0 \mathbf{I} - \mathbf{M}^t \quad (4.18)$$

Moreover distributed volume forces \mathbf{B}_0 per unit volume \mathcal{B}_0 can be retrieved from relation (4.17) in the following manner

$$\mathbf{B}_0 = A \nabla_X \alpha - \partial_{\mathbf{X}} \psi_0 - \mathbf{F}^t \cdot \mathbf{b}_0 \quad (4.19)$$

Summarizing, the material motion balance of momentum is obtained as

$$\mathbf{o} = \mathbf{F}^t \cdot [\text{Div} \mathbf{\Pi}^t + \mathbf{b}_0] \quad \longrightarrow \quad \mathbf{o} = \text{Div} \mathbf{\Sigma}^t + \mathbf{B}_0 \quad (4.20)$$

4.2 Weak Form

As a prerequisite for a finite element discretization the nonlinear boundary value problem has to be reformulated in weak or rather variational form. Again, the duality of the spatial and material point of view is elaborated.

4.2.1 Spatial motion problem

Firstly, the pointwise statement of the spatial balance of momentum $-\text{div} \boldsymbol{\sigma}^t = \mathbf{b}_t$ is tested by spatial virtual displacements $\delta \boldsymbol{\varphi} = \mathbf{w}$ under the necessary smoothness and boundary assumptions to render the virtual work expression

$$\underbrace{\int_{\partial \mathcal{B}_t} \mathbf{w} \cdot \boldsymbol{\sigma}^t \cdot \mathbf{n} \, da}_{\mathfrak{w}^{sur}} = \underbrace{\int_{\mathcal{B}_t} \nabla_x \mathbf{w} : \boldsymbol{\sigma}^t \, dv}_{\mathfrak{w}^{int}} - \underbrace{\int_{\mathcal{B}_t} \mathbf{w} \cdot \mathbf{b}_t \, dv}_{\mathfrak{w}^{vol}} \quad \forall \mathbf{w} \quad (4.21)$$

For a conservative system the different energetic terms \mathfrak{w}^{sur} , \mathfrak{w}^{int} and \mathfrak{w}^{vol} may be interpreted by considering the spatial variation at fixed \mathbf{X} of the free energy density ψ_0 . As

a result, the contribution \mathfrak{w}^{sur} denotes the spatial variation of ψ_0 due to its complete dependence on the spatial position, whereas the contributions \mathfrak{w}^{int} and \mathfrak{w}^{vol} denote the spatial variations of ψ_0 due to its implicit and explicit dependence on the spatial position, respectively.

Secondly, we propose the weak form of the constitutive subproblem in order to cope with the damage field. As shown in chapter 4.1.2 the distributed volume forces require the gradient w.r.t. to the damage variable. Thus it becomes necessary to separately discretize d as an additional field. Therefore we advocate a constitutive subproblem represented by the variational format of the Karush-Kuhn-Tucker complementary conditions $\varphi \leq 0$ and $D_t d \geq 0$ which are tested by δd with $\delta d > 0$ and by $\delta \varphi$ with $\delta \varphi > 0$, respectively, to render the global statements

$$\mathfrak{w}^\varphi = \int_{\mathcal{B}_0} \delta d [Y_0 - \kappa] dV \leq 0 \quad \text{and} \quad \mathfrak{w}^d = \int_{\mathcal{B}_0} \delta \varphi D_t d dV \geq 0 \quad (4.22)$$

Based on these statements, the decomposition of the solution domain \mathcal{B}_0 into an actively damaged and inactive elastic domain $\mathcal{B}_0 = \mathcal{B}_0^d \cup \mathcal{B}_0^e$ and $\emptyset = \mathcal{B}_0^e \cap \mathcal{B}_0^d$ follows implicitly as the support of those admissible test functions $\delta d, \delta \varphi$ which satisfy

$$\begin{aligned} \mathcal{B}_0^e &= \{ \mathbf{X} \in \mathcal{B}_0 \mid \mathfrak{w}^\varphi \leq 0, \mathfrak{w}^d = 0 \ \forall \delta d, \delta \varphi > 0 \ \text{in} \ \mathcal{B}_0^e \} \\ \mathcal{B}_0^d &= \{ \mathbf{X} \in \mathcal{B}_0 \mid \mathfrak{w}^\varphi = 0, \mathfrak{w}^d > 0 \ \forall \delta d, \delta \varphi > 0 \ \text{in} \ \mathcal{B}_0^d \} \end{aligned} \quad (4.23)$$

4.2.2 Material motion problem

Here, the pointwise statement of the material balance of momentum $-\text{Div} \boldsymbol{\Sigma}^t = \mathbf{B}_0$ is tested by material virtual displacements $\delta \boldsymbol{\Phi} = \mathbf{W}$ under the necessary smoothness and boundary assumptions to render the virtual work expression

$$\underbrace{\int_{\partial \mathcal{B}_0} \mathbf{W} \cdot \boldsymbol{\Sigma}^t \cdot \mathbf{N} dA}_{\mathfrak{W}^{sur}} = \underbrace{\int_{\mathcal{B}_0} \nabla_X \mathbf{W} : \boldsymbol{\Sigma}^t dV}_{\mathfrak{W}^{int}} - \underbrace{\int_{\mathcal{B}_0} \mathbf{W} \cdot \mathbf{B}_0 dV}_{\mathfrak{W}^{vol}} \quad \forall \mathbf{W} \quad (4.24)$$

Again for a conservative system the different energetic terms \mathfrak{W}^{sur} , \mathfrak{W}^{int} and \mathfrak{W}^{vol} may be interpreted by considering the material variation at fixed \mathbf{x} of the free energy density ψ_t . As a result, the contribution \mathfrak{W}^{sur} denotes the material variation of ψ_t due to its complete dependence on the material position, whereas the contributions \mathfrak{W}^{int} and \mathfrak{W}^{vol} denote the material variations of ψ_t due to its implicit and explicit dependence on the material position, respectively.

Remark Note that the two variational formulations in Eqs. 4.21 and 4.24 are connected by $\mathbf{w} = -\mathbf{W} \cdot \mathbf{F}^t$ and $\mathbf{W} = -\mathbf{w} \cdot \mathbf{f}^t$ for the relation between the spatial and material virtual displacements, see also Maugin & Trimarco [104]. Taking into account the relations derived in chapter 4.1.3, applying integration by parts and invoking the Gauss theorem

we may expand e.g. $\int_{\mathcal{B}_0} \mathbf{w} \cdot \text{Div} \mathbf{\Pi}^t \, dV$ into $\int_{\mathcal{B}_0} \mathbf{W} \cdot [\text{Div} \mathbf{\Sigma}^t + \mathbf{B}_0 + \mathbf{F}^t \cdot \mathbf{b}_0] \, dV$.¹

4.3 Discretization

The above variational set of quasi-static balances of momentum will be discretized by the standard Bubnov-Galerkin finite element method rendering discrete spatial and material node point (surface) forces.

4.3.1 Spatial motion problem

In addition to the discretization of the hyperelastic case as described in section 2.4 we now introduce an additional damage field d . The damage variable field d , together with its variation δd is expanded elementwise by independent shape functions N_d^k in terms of the nodal values d_k and δd_k

$$d^h|_{\mathcal{B}_0^e} = \sum_k N_d^k d_k \quad \text{and} \quad \delta d^h|_{\mathcal{B}_0^e} = \sum_k N_d^k \delta d_k \quad (4.25)$$

Lastly, based on the above discretization, the corresponding gradient $\nabla_X d$ take the elementwise format

$$\nabla_X d^h|_{\mathcal{B}_0^e} = \sum_k d_k \nabla_X N_d^k$$

Then, based on the spatial discretizations of the primary variables φ and d the discretized internal and volume contributions to the spatial virtual work follow as

$$\mathfrak{w}_h^{int} = \mathbf{A}_e \sum_k \mathbf{w}_k \cdot \int_{\mathcal{B}_0^e} \boldsymbol{\sigma}^t \cdot \nabla_x N_\varphi^k \, dv \quad (4.26)$$

$$\mathfrak{w}_h^{vol} = \mathbf{A}_e \sum_k \mathbf{w}_k \cdot \int_{\mathcal{B}_0^e} N_\varphi^k \mathbf{b}_t \, dv \quad (4.27)$$

Thus implying the arbitrariness of the spatial virtual node point displacements \mathbf{w}_k the discrete algorithmic spatial node point (surface) forces are obtained at global node K as follows

$$\mathfrak{f}_{sur,K}^h = \mathbf{A}_e \int_{\mathcal{B}_0^e} [\boldsymbol{\sigma}^t \cdot \nabla_x N_\varphi^k - N_\varphi^k \mathbf{b}_t]_{n+1} \, dv. \quad (4.28)$$

¹Convince yourself by considering the following derivation:

$$\begin{aligned} -\mathbf{W} \cdot \mathbf{F}^t \cdot \text{Div} \mathbf{\Pi}^t &= -\mathbf{W} \cdot \text{Div}(\mathbf{F}^t \cdot \mathbf{\Pi}^t) + \mathbf{W} \cdot \mathbf{\Pi}^t : \nabla_X \mathbf{F} \\ &= -\mathbf{W} \cdot \text{Div}(\mathbf{F}^t \cdot \mathbf{\Pi}^t) + \mathbf{W} \cdot [\text{Div}(\psi_0 \mathbf{I}) + A \nabla_X \alpha - \partial_X \psi_0] \\ &= \mathbf{W} \cdot [\text{Div} \mathbf{\Sigma}^t + \mathbf{B}_0 + \mathbf{F}^t \cdot \mathbf{b}_0] \end{aligned}$$

Here we assumed the implicit Euler backward method for the time discretization without loss of generalization. Thereby the temporal integration of the primary variables φ and d renders a discretized temporal update for the values φ_{n+1} and d_{n+1} .

Furthermore, the discrete algorithmic Karush-Kuhn-Tucker complementary conditions are obtained at global node K , whereby the first one represents the discrete algorithmic damage condition and the second one assures positive increments of the damage variable

$$\mathbf{r}_K^\varphi = \mathbf{A}_e \int_{\mathbb{B}_0} [N_d^k [Y_0 - \kappa]]_{n+1} dV \quad \text{and} \quad \mathbf{r}_K^d = \mathbf{A}_e \int_{\mathbb{B}_0} [N_d^k [d_{n+1}^h - d_n^h]] dV \quad (4.29)$$

whereby $[\bullet]_n$ and $[\bullet]_{n+1}$ denote successive time steps.

Moreover, the discrete algorithmic decomposition of the node point set with $\mathbb{B} = \mathbb{B}_{n+1}^d \cup \mathbb{B}_{n+1}^e$ and $\emptyset = \mathbb{B}_{n+1}^d \cap \mathbb{B}_{n+1}^e$ takes the following explicit format

$$\begin{aligned} \mathbb{B}_{n+1}^e &= \{K \in \mathbb{B} | \mathbf{r}_K^\varphi \leq 0, \mathbf{r}_K^d = 0\} \\ \mathbb{B}_{n+1}^d &= \{K \in \mathbb{B} | \mathbf{r}_K^\varphi = 0, \mathbf{r}_K^d > 0\}. \end{aligned} \quad (4.30)$$

The initially unknown decomposition of the discretization node point set into active and inactive subsets $\mathbb{B} = \mathbb{B}_{n+1}^d \cup \mathbb{B}_{n+1}^e$ at time step t_{n+1} is determined iteratively by an active set search. Thereby, the strategy is borrowed from convex nonlinear programming, see Luenberger [54] as is frequently used e.g. in multi-surface and crystal plasticity. For a detailed solution strategy w.r.t. the geometrically linear gradient damage case we refer to Liebe et al. [52], see also Liebe and Steinmann [51] in the case of geometrically linear gradient plasticity .

4.3.2 Material motion problem

Following the ideas of section 2.4 the discrete algorithmic material node point (surface) forces at global node point K are obtained as follows

$$\mathfrak{F}_{sur,K}^h = \mathbf{A}_e \int_{\mathbb{B}_0^e} [\boldsymbol{\Sigma}^t \cdot \nabla_X N^k - N_\phi^k \mathbf{B}_0]_{n+1} dV, \quad (4.31)$$

whereby we denote the material surface forces $\mathfrak{F}_{sur,K}^h$ by 'SUR' in the diagrams later in the example section. Furthermore we separate on the one hand

$$\mathfrak{F}_{int,K}^h = \mathbf{A}_e \int_{\mathbb{B}_0^e} [\boldsymbol{\Sigma}^t \cdot \nabla_X N^k]_{n+1} dV \quad (4.32)$$

the internal part of the discrete algorithmic material node point (surface) forces denoted by 'INT' and on the other hand

$$\mathfrak{F}_{vol,K}^h = \mathbf{A}_e \int_{\mathbb{B}_0^e} [N_\phi^k \mathbf{B}_0]_{n+1} dV \quad (4.33)$$

the volume part of the discrete algorithmic material node point (surface) forces denoted by 'VOL' for later use in the example section. Thus we have in summary the obvious result

$$\mathfrak{F}_{sur,K}^h = \mathfrak{F}_{int,K}^h - \mathfrak{F}_{vol,K}^h \quad (4.34)$$

Based on these results we advocate the Material Force Method with the notion of global discrete material node point (surface) forces, that (in the sense of Eshelby) are generated by variations relative to the ambient material at fixed spatial positions. Such forces corresponding to the material motion problem are trivially computable once the spatial motion problem has been solved. Moreover, due to the interpretation of material forces as being energetically conjugate to configurational changes, discrete material forces at the boundary may be considered as a measure of the geometrical shape sensitivity of a specimen.

4.3.3 Discretized format of J-integral: Material Force Method

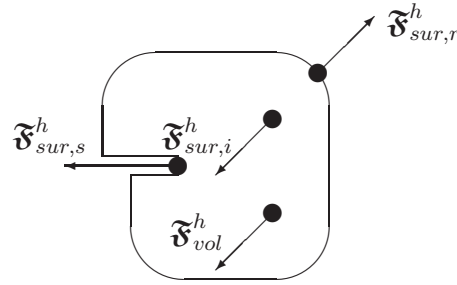


Figure 4.1. Balance of discrete material node point forces

Consider the resulting discrete material node point (surface) force $\mathfrak{F}_{sur,s}^h$ acting on a crack tip, see Fig. 4.1. In analogy to the continuum format of the quasi-static equilibrium of material forces the exact value $\mathfrak{F}_{sur,s}$ in Eq. 2.21 can be approximated by the discrete regular surface part $\mathfrak{F}_{sur,r}^h$ and the discrete volume part \mathfrak{F}_{vol}^h of the discrete material node point (surface) forces

$$\mathfrak{F}_{sur,s} \approx -\mathfrak{F}_{sur,r}^h - \mathfrak{F}_{vol}^h \quad (4.35)$$

These in turn are balanced by discrete singular material surface forces $\mathfrak{F}_{sur,s}^h$ and (spurious) discrete internal material surface forces $\mathfrak{F}_{sur,i}^h$, which stem from an insufficient discretization accuracy as follows

$$-\mathfrak{F}_{sur,r}^h - \mathfrak{F}_{vol}^h = \mathfrak{F}_{sur,s}^h + \mathfrak{F}_{sur,i}^h \quad (4.36)$$

Note thus, that the sum of all discrete algorithmic material node point surface forces

$\mathfrak{F}_{sur,K}^h$ corresponds according to Eq. 4.31 to the resulting value

$$\mathfrak{F}_{sur,s} \approx \sum_{K \in \mathcal{V}_0^h \setminus \partial \mathcal{V}_0^{r,h}} \mathfrak{F}_{sur,K}^h = \mathfrak{F}_{sur,s}^h + \mathfrak{F}_{sur,i}^h \quad (4.37)$$

Thus an improved value for $\mathfrak{F}_{sur,s}$ is obtained by summing up all discrete material node point surface forces in the vicinity of the crack tip, see also Denzer et al. [22]. Observe that the presence of spurious discrete internal material surface forces $\mathfrak{F}_{sur,i}^h$ as implied by Eq. 4.36 indicates that a change of the node point positions of the discretization renders an improved mesh with less potential energy content in the conservative case, see also the reasoning by Braun [12] and Maugin [62].

4.4 Numerical examples

In this section we focus on the computational performance and versatility of the proposed Material Force Method with the incorporation of isotropic damage. To this end we first study the results of a geometrically nonlinear computation obtained for a specimen with an elliptic hole with varying axis ratios under tension. Next we compare these results with a center cracked (CCT) fracture mechanics specimen in tension. Finally for validation purposes we pursue a convergence study of a 'Modified Boundary Layer'-formulation (MBL-formulation) of a straight, traction free crack.

4.4.1 Specimen with elliptic hole

First, we consider different specimen with an elliptic hole for varying axes ratios ranging from a full circle ($a/b = 1.0$) to a slender ellipse ($a/b = 0.1$), see Fig. 4.2 in tension with plane strain constraint. The height to width ratio is $H/W = 3$. The specimen is discretized by bi-linear $Q1$ -elements. The mesh is densified towards the hole boundary.

The virgin material is modeled based on a compressible Neo-Hookean formulation $W_0 = \mu [(I_1 - \ln J)/2 - 3] + \lambda \ln^2 J/2$ with the shear modulus $\mu = 27540$ MPa and the bulk modulus $K = \lambda + 2/3\mu = 59666$ MPa corresponding roughly to aluminum.

For the damage evolution law, we specify the function $\phi(\kappa)$ with $\kappa_0 = 0.01$ MPa the assumed initial damage threshold and $h = 0.1$ a material parameter as $\phi(\kappa) = 1 - \exp(h[\kappa_0 - \kappa])$. Note that the particular choice of the supposed damage evolution may influence the overall behavior of the considered specimen. The corresponding damage evolution with an increasing internal variable $\kappa > \kappa_0$ is depicted in Fig. 4.3.

A constant elongation is applied incrementally by prescribed displacements at the top surface, the lateral movement of the nodes at the top and bottom surface are unconstrained. Firstly we depict the damage variable distribution within zooms of the typical scenario around the hole for varying axes ratios a/b . Thereby an evolving damage zone is shown ranging from the purely undamaged elastic state (Fig. 4.4a) to a state with completely

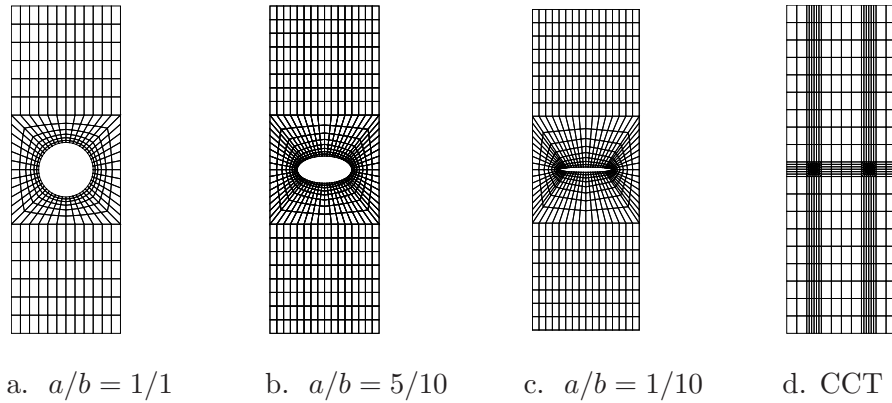


Figure 4.2. Specimen geometries

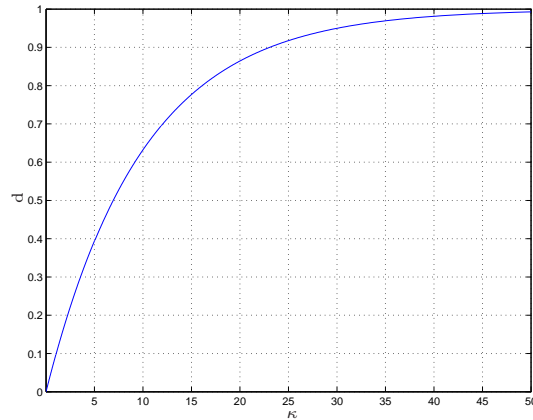


Figure 4.3. Damage evolution versus internal variable

damaged nodes (Fig. 4.4d). There are two intermediate states represented exhibiting the first appearance of damaged nodes (Fig. 4.4b) and a further advanced damage state of the first active nodes (Fig. 4.4c).

Then the computed discrete material node point surface forces are visualized in Fig. 4.5. Due to the fact that $\mathfrak{F}_{sur,K}^h = \mathfrak{F}_{int,K}^h - \mathfrak{F}_{vol,K}^h$ holds, we separately plot the internal part of the discrete material node point (surface) forces 'INT', see Fig. 4.6 and the (negative) volume part of the discrete material node point forces 'VOL', see Fig. 4.7. In all figures the contour lines representing the damage state are superposed for convenience. Thereby the discrete material node point surface forces 'SUR' point into the directions of an energy increase upon replacement of the material node point position. Thus the initiation of a crack in the direction opposite to the material (surface) force, in particular the replacement of the material position at the root of the notch node point, that enlarges the macro crack into the virgin material, corresponds to an energy release. Note in addition that the

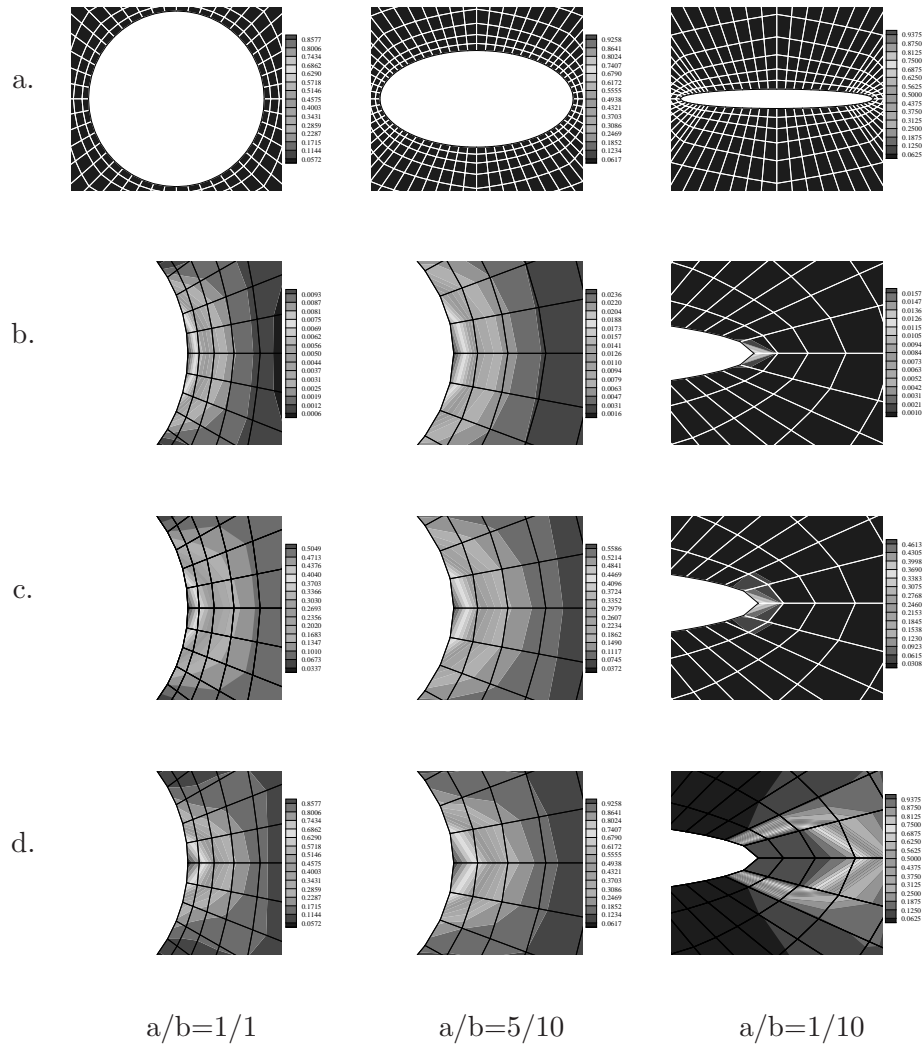


Figure 4.4. Damage variable evolution

(negative) volume part of the discrete material node point forces 'VOL' points along the (negative) gradient ∇d of the damage field, which appears to reduce the far-field material loading and hence the resulting material node point surface force at the root of the notch. Note that the (negative) volume part of the discrete material node point forces 'VOL' are of one order smaller in magnitude compared with the internal part of the discrete material node point (surface) forces 'INT', see Fig. 4.7.

Observe finally that the more slender the elliptic hole the more diverted the material node point (surface) forces 'SUR' become at the root of the notch with an increasing damage zone. This is due to the fact that the finite elements in the vicinity of notch get highly distorted for $a/b = 1/10$, see Fig. 4.5. Contrary it is notable that within a circular hole the material node point (surface) forces get aligned perpendicular to the load direction

corresponding to a possible horizontal line crack initiation, see Fig. 4.5. In order to cope with a real crack we next investigate a CCT-specimen, which is discretized in a suitable way to avoid highly distorted elements.

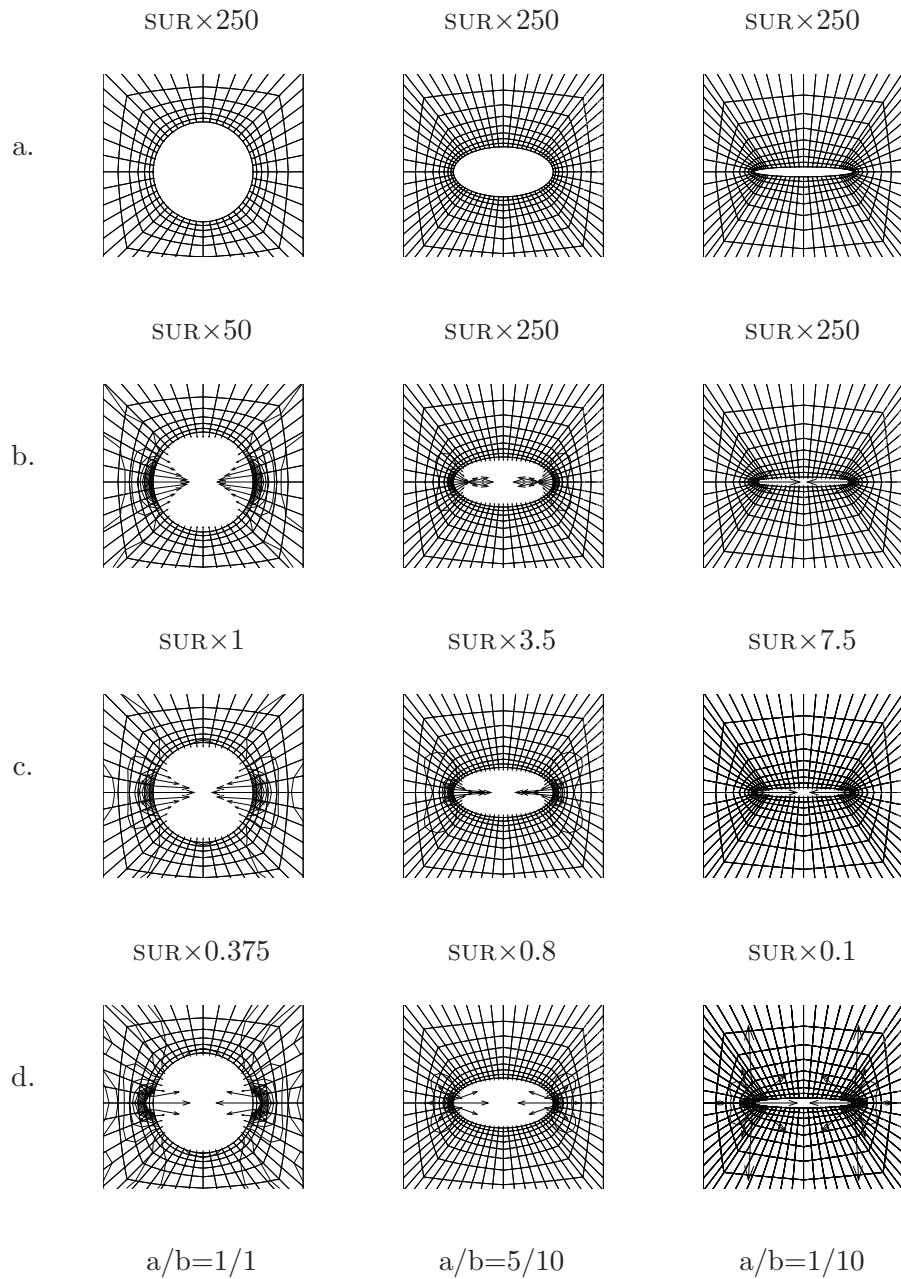


Figure 4.5. Discrete material node point (surface) forces 'SUR'

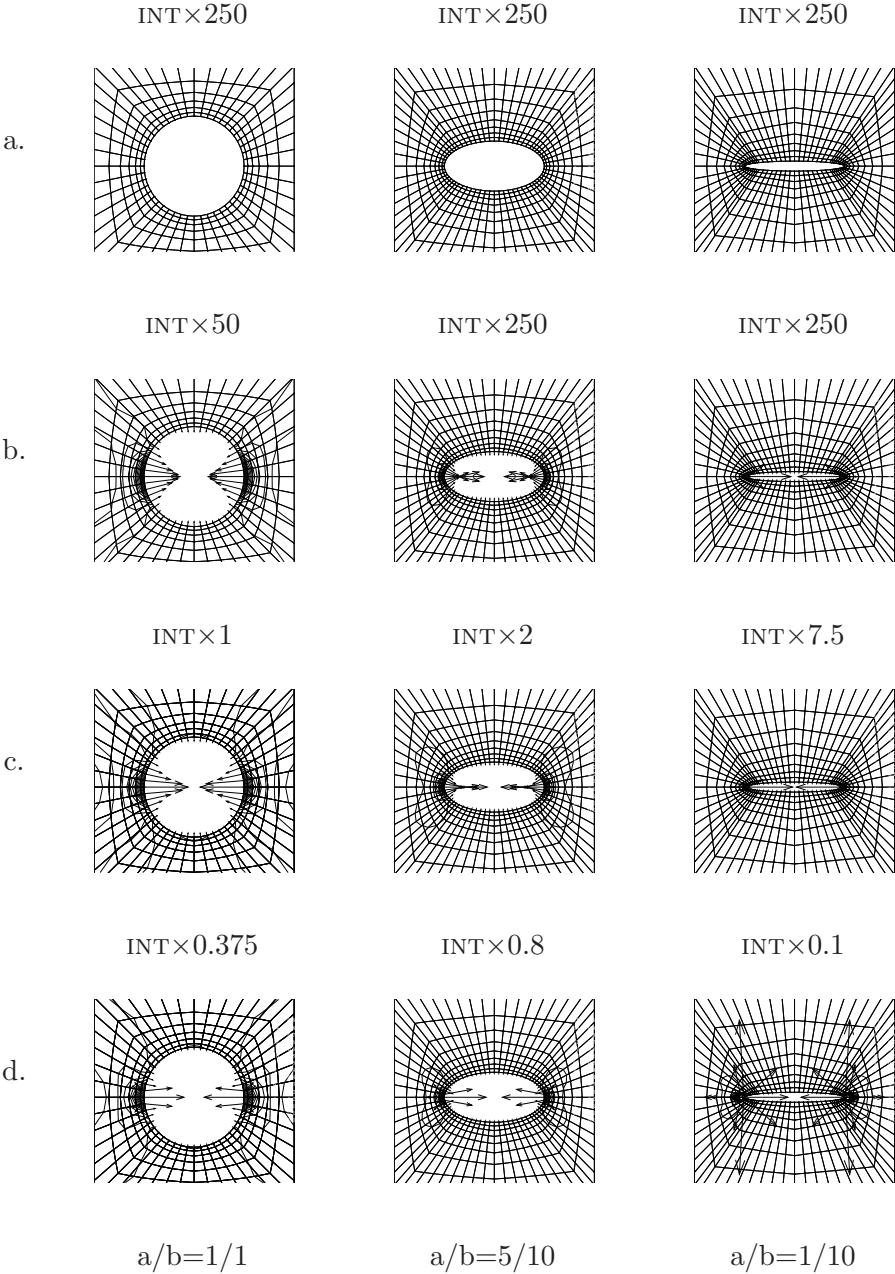


Figure 4.6. Discrete internal part of material node point forces 'INT'

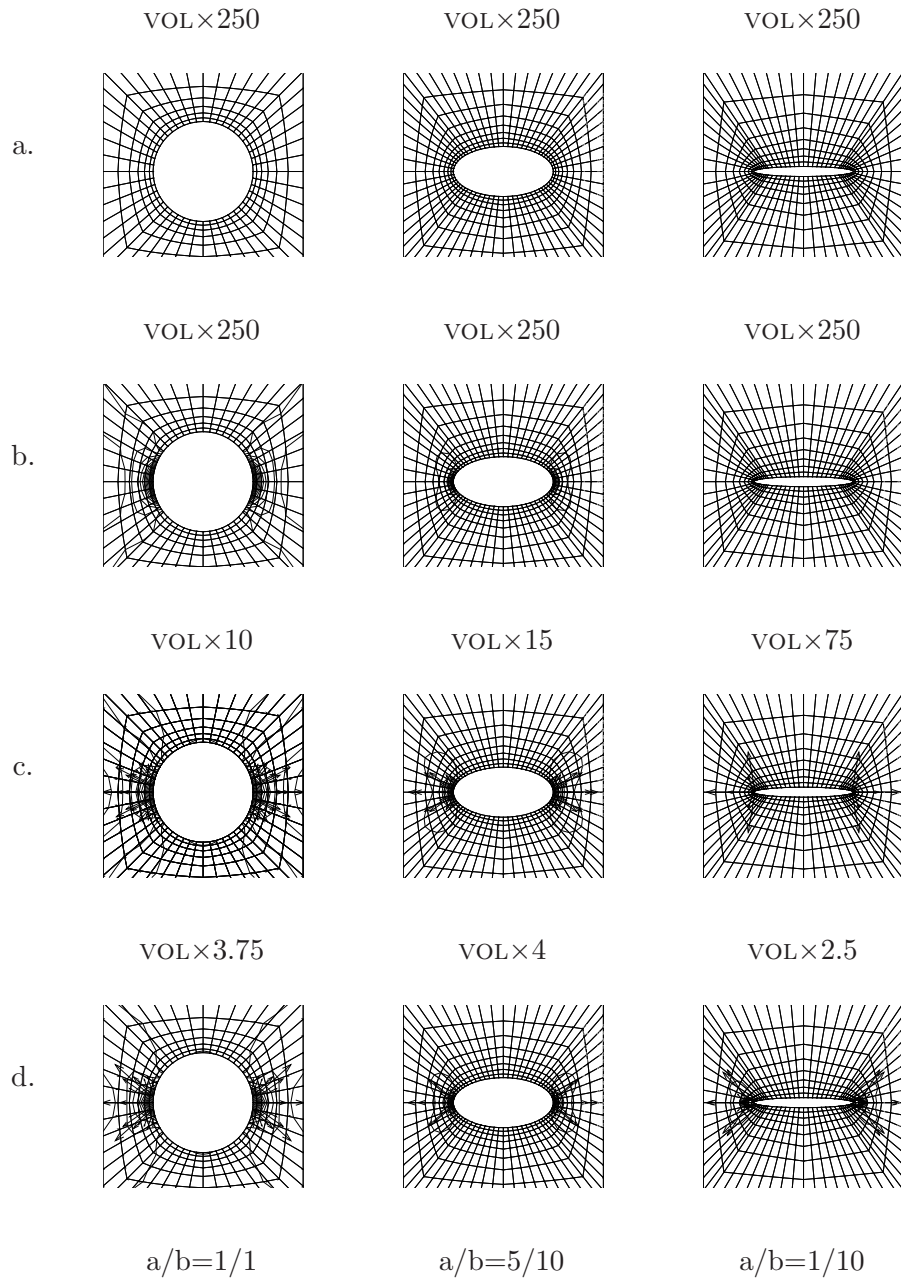


Figure 4.7. Discrete (negative) volume part of material node point forces 'VOL'

4.4.2 Specimen with center crack

Next we study the influence of a center cracked fracture specimen in tension with geometry and material model as in the previous example, see Fig. 4.2d. This time the mesh is discretized with bi-quadratic S^2 -serendipity elements and is heavily densified in the vicinity of the crack tip, whereas the elements connected to the crack tip node are standard $P2$ -triangular elements. A constant elongation is applied incrementally by prescribed displacements at the top surface, the lateral movement of the nodes at the top and bottom surface are unconstrained.

Here we consider the damage variable distribution for different damage states ranging from the purely undamaged elastic stage to the state where nodes around the crack tip are completely damaged, see zooms of the typical scenario at the crack tip, Fig. 4.8.

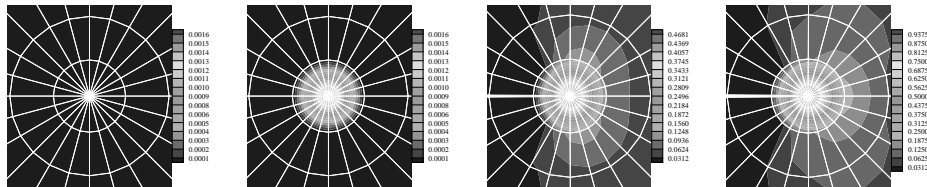


Figure 4.8. Damage distribution at crack tip for different damage states

The computed discrete material node point (surface) forces point again into the direction of an energy increase upon replacement of the material node point position. Thus the growth of the crack in the direction opposite to the material force, i.e. the replacement of the material position of the crack tip node point tries to proceed the crack tip further into the material, corresponds to an energy release. We observe the similar damage zone as for the case of the slender elliptic hole, compare with Fig. 4.4, i.e. it almost resembles the singular crack tip of the CCT-specimen investigated here. Due to better discretization of the crack vicinity of the CCT-specimen less diverted spurious material node point forces can be found along the crack tip. Instead we have essentially a single material node point (surface) force perpendicular to the load direction pointing into the crack, see Fig. 4.9. Therefore the spurious material forces act as a sensitive indicator for the mesh quality.

Once again the discrete (negative) volume part of the material node point forces points along the (negative) gradient of the damage field into the material surrounding the crack tip, see Fig. 4.11. Note that the volume part 'VOL' is of one order smaller in magnitude compared with the internal part 'INT'. Therefore the shielding effect against the external material loading is not very pronounced and in this example no significant difference between the total discrete material node point (surface) forces and the internal part can be found, see Fig. 4.10.

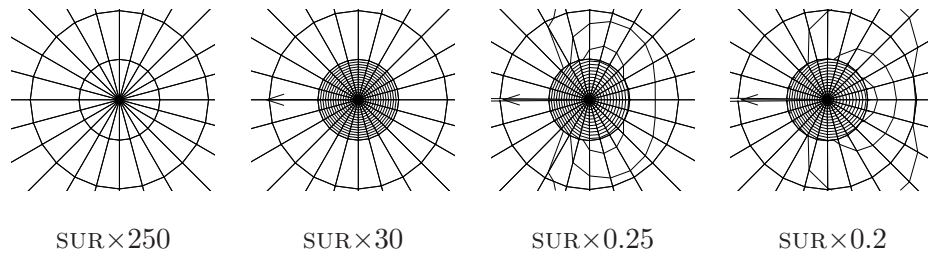


Figure 4.9. Discrete material node point (surface) forces for different damage states

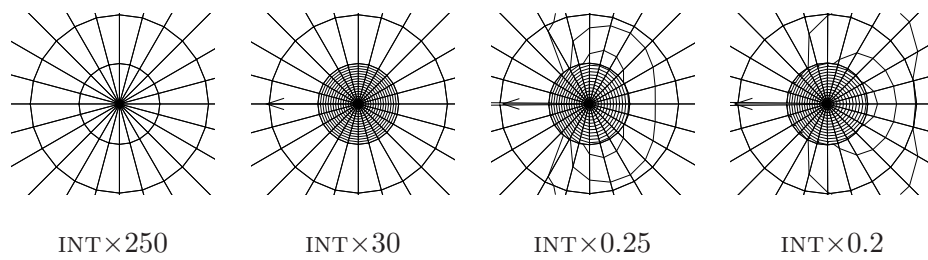


Figure 4.10. Discrete internal part of material node point forces for different damage states

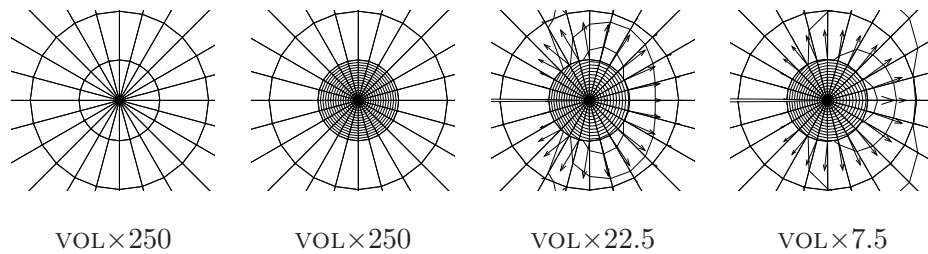


Figure 4.11. Discrete (negative) volume part of material node point forces for different damage states

4.4.3 MBL-specimen

For validation purposes, we consider finally a 'Modified Boundary Layer' formulation (MBL-formulation) [36, 82] of a straight, traction free crack. The discretization and the material model are the same as in the previous example. The MBL-formulation is based on an isolated treatment of the crack tip region which is independent of the surrounding specimen, see Fig. 4.12. Under 'Small Scale Damage' (SSD)² conditions this region is chosen in such a way that a small crack tip damage zone, dominated by the nonlinear part of the material formulation, is surrounded by a large elastic boundary layer mainly controlled by elastic material behavior. We define the damaged zone near the crack tip

²according to 'Small Scale Yielding' (SSY) conditions in classical fracture mechanics

by that region where the damage variable κ_0 is exceeded.

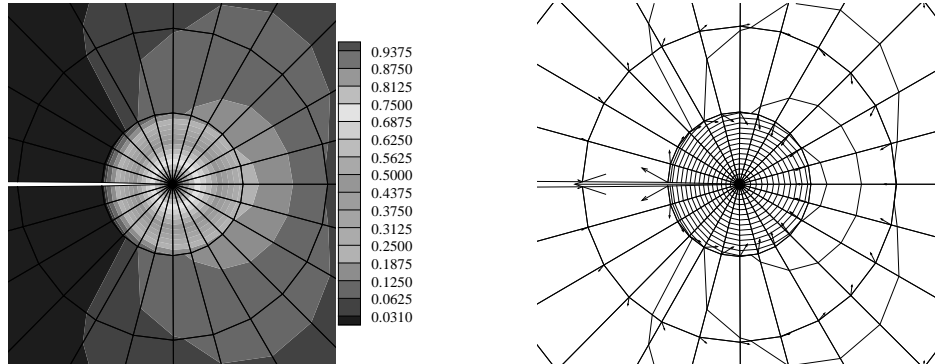


Figure 4.12. Contour plot of damage variable and discrete material surface node point forces

In this work we apply the first term of the asymptotic linear elastic stress series near a crack tip given by Williams [108] as $\boldsymbol{\sigma} = \frac{K_I}{\sqrt{2\pi r}} \mathbf{f}(\theta)$. Here K_I denotes the stress intensity factor and $\mathbf{f}(\theta)$ are given functions depending only on the angle θ measured counterclockwise from the positive x-axis. Under SSD-conditions, the linear elastic relation for the J-integral $J_{pre} = K_I^2/E'$ with $E' = E/[1 - \nu^2]$ for plane strain holds. To ensure SSD-conditions in the MBL-formulation we discretized a circular area around the crack tip with a radius R at least 1000 times larger than the maximum size of the damaged zone. In the following figures we depict the MBL-specimen with a damaged crack tip as a contour plot of the damage variable and a line contour plot of the damage variable together with the discrete material surface node point forces, see Fig. 4.12.

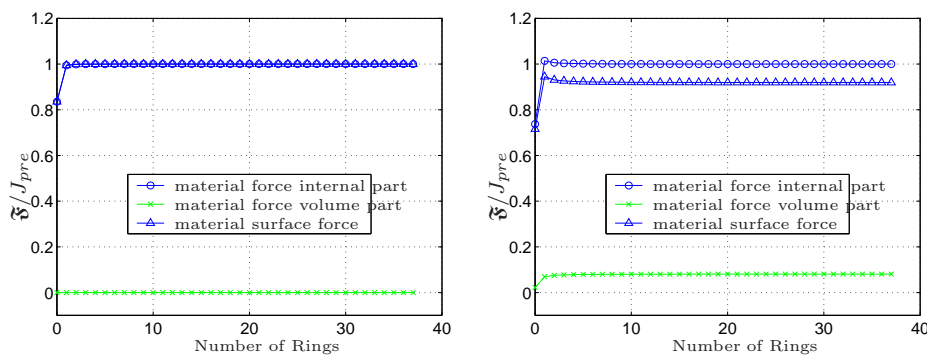


Figure 4.13. Purely elastic state vs. advanced damage state

Then we investigate the influence of the damage zone near the crack tip. Therefore we compare a purely elastic state and an advanced damaged state, see Fig. 4.13. According to Eqs. 4.36,4.37 the sum of all discrete algorithmic material node point surface forces renders an improved value for the material force at the crack tip. The sum is taken over a

varying number of rings of elements around the crack tip. After only a few number of rings the internal part of the material node point surface force is converged to the prescribed material load and remains constant. Due to the increasing damage zone around the crack tip the volume part of the discrete material node point forces increases accordingly with the gradient of the damage field. Therefore the discrete material node point surface force on the crack tip is decreased due to the evolving damage around the crack tip compared to the purely elastic state. Thus the crack tip might be considered as being shielded by the distributed damage field. This 'shield' is formed closely around the crack tip and converges after a few rings to a constant value.

Chapter 5

Plasticity

In the following sections we briefly elaborate the material format of the quasi-static balance of momentum of a geometrically nonlinear problem involving multiplicative elasto-plasticity. Our derivation is motivated by the work of Epstein and Maugin [23, 25, 24], Maugin [56] and Cleja-Tigoiu and Maugin [17].

5.1 Kinematics

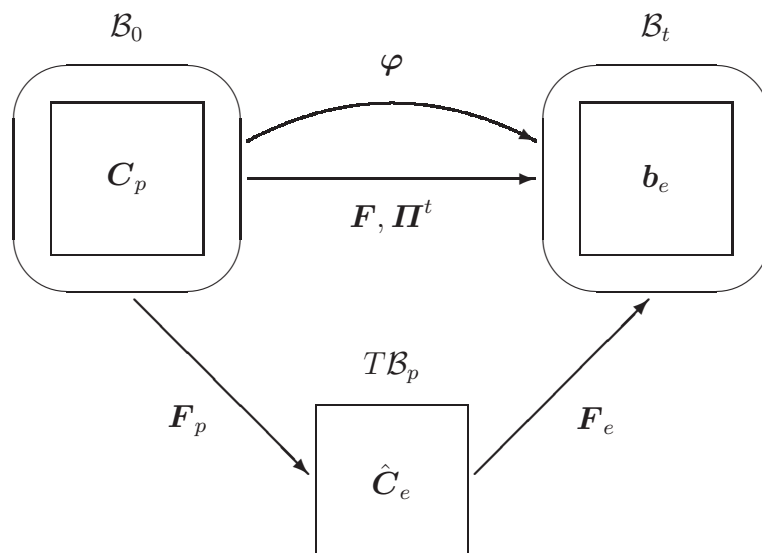


Figure 5.1. Kinematics of multiplicative elasto-plasticity

In the framework of multiplicative elastoplasticity an intermediate configuration \mathcal{B}_p is introduced, see fig. 5.1. This configuration is stress free and incompatible. We assume, that the total deformation gradient \mathbf{F} of the spatial motion problem is the result of a composition of a plastic distortion \mathbf{F}_p and an elastic distortion \mathbf{F}_e

$$\mathbf{F} = \mathbf{F}_e \cdot \mathbf{F}_p \quad (5.1)$$

Neither \mathbf{F}_e nor \mathbf{F}_p are generally representable as the gradient of a placement vector and therefore do not satisfy the conditions of compatibility.

5.2 Material motion balance of momentum

To derive the format of the material motion balance of momentum and thus the format of the Eshelby stress tensor $\boldsymbol{\Sigma}^t$ and the internal material volume force \mathbf{B}_0^{int} in the case of finite hyperelasto-plasticity we assume the existence of a free Helmholtz energy ψ_0 of the following format (see Epstein and Maugin [23])

$$\psi_0 = \psi_0(\mathbf{F}, \mathbf{F}_p, \kappa; \mathbf{X}) = J_p \psi_p(\mathbf{F} \cdot \mathbf{F}_p^{-1}, \kappa; \mathbf{X}) \quad \text{with} \quad J_p = \det(\mathbf{F}_p) \quad (5.2)$$

We start with the spatial motion balance of momentum

$$\text{Div} \boldsymbol{\Pi}^t + \mathbf{b}_0^{ext} = \mathbf{0} \quad (5.3)$$

and a covariant pull back leads to

$$\mathbf{F}^t \cdot \text{Div} \boldsymbol{\Pi}^t + \mathbf{F}^t \cdot \mathbf{b}_0 = \mathbf{0}. \quad (5.4)$$

in conjunction with the identity

$$\text{Div}(\mathbf{F}^t \cdot \boldsymbol{\Pi}^t) = \mathbf{F}^t \cdot \text{Div} \boldsymbol{\Pi}^t + \nabla_X \mathbf{F}^t : \boldsymbol{\Pi}^t \quad \text{or} \quad (5.5)$$

$$\mathbf{F}^t \cdot \text{Div} \boldsymbol{\Pi}^t = \text{Div}(\mathbf{F}^t \cdot \boldsymbol{\Pi}^t) - \nabla_X \mathbf{F}^t : \boldsymbol{\Pi}^t \quad (5.6)$$

we end up with

$$\text{Div}(\mathbf{F}^t \cdot \boldsymbol{\Pi}^t) - \nabla_X \mathbf{F}^t : \boldsymbol{\Pi}^t = \mathbf{0} + \mathbf{F}^t \cdot \mathbf{b}_0. \quad (5.7)$$

Using the compatibility condition for \mathbf{F} in the format

$$\nabla_X \mathbf{F}^t : \boldsymbol{\Pi}^t = \boldsymbol{\Pi}^t : \nabla_X \mathbf{F} \quad (5.8)$$

together with equation (5.7) results in

$$\text{Div}(\mathbf{F}^t \cdot \boldsymbol{\Pi}^t) - \boldsymbol{\Pi}^t : \nabla_X \mathbf{F} + \mathbf{F}^t \cdot \mathbf{b}_0 = \mathbf{0}. \quad (5.9)$$

Now we reformulate the expression $\boldsymbol{\Pi}^t : \nabla_X \mathbf{F}$ by analysing the identity

$$\text{Div}(\psi_0 \mathbf{I}) = \mathbf{I} \nabla_X \psi_0 + \psi_0 \text{Div} \mathbf{I} = \mathbf{I} \cdot \nabla_X \psi_0 = \nabla_X \psi_0 \quad (5.10)$$

where we took $\text{Div} \mathbf{I} = \mathbf{0}$ into account. The material gradient of ψ_0 is

$$\nabla_X \psi_0(\mathbf{F}, \mathbf{F}_p, \kappa) = \mathbf{D}_{\mathbf{F}} \psi_0 : \nabla_X \mathbf{F} + \mathbf{D}_{\mathbf{F}_p} \psi_0 : \nabla_X \mathbf{F}_p + \mathbf{D}_\kappa \psi_0 \nabla_X \kappa + \partial_X \psi_0 \quad (5.11)$$

with $\mathbf{\Pi}^t = \mathbf{D}_{\mathbf{F}} \psi_0$ and $\mathbf{\Pi}_p^t = \mathbf{D}_{\mathbf{F}_p} \psi_0$ we can rewrite this as

$$\nabla_X \psi_0(\mathbf{F}, \mathbf{F}_p, \kappa) = \mathbf{\Pi}^t : \nabla_X \mathbf{F} + \mathbf{\Pi}_p^t : \nabla_X \mathbf{F}_p + \mathbf{D}_\kappa \psi_0 \nabla_X \kappa + \partial_X \psi_0 \quad (5.12)$$

or by using the identity from equation (5.10) we encounter

$$\mathbf{\Pi}^t : \nabla_X \mathbf{F} = \text{Div}(\psi_0 \mathbf{I}) - \mathbf{\Pi}_p^t : \nabla_X \mathbf{F}_p - \mathbf{D}_\kappa \psi_0 \nabla_X \kappa - \partial_X \psi_0. \quad (5.13)$$

Now we want to analyze $\mathbf{\Pi}_p^t = \mathbf{D}_{\mathbf{F}_p} \psi_0$ a bit more. We need the expression

$$\mathbf{\Pi}^t = \mathbf{D}_{\mathbf{F}} \psi_0 = J_p \mathbf{D}_{\mathbf{F}} \psi_0 \quad (5.14)$$

and

$$\mathbf{D}_{\mathbf{F}_e} \psi_p = \mathbf{D}_{\mathbf{F}} \psi_p : \mathbf{D}_{\mathbf{F}_e} \mathbf{F} = \mathbf{D}_{\mathbf{F}} \psi_p \cdot \mathbf{F}_p^t \quad (5.15)$$

to get

$$\mathbf{\Pi}_p^t = \mathbf{D}_{\mathbf{F}_p} \psi_0 = \mathbf{D}_{\mathbf{F}_p} (J_p \psi_p) \quad (5.16)$$

$$= \psi_p \mathbf{D}_{\mathbf{F}_p} J_p + J_p \mathbf{D}_{\mathbf{F}_e} \psi_p : \mathbf{D}_{\mathbf{F}_p} \mathbf{F}_e \quad (5.17)$$

$$= \mathbf{F}_p^{-t} \cdot [\psi_0 \mathbf{I} - \mathbf{F}^t \cdot \mathbf{\Pi}^t] = \mathbf{F}_p \cdot \mathbf{\Sigma}^t \quad (5.18)$$

$$= \psi_0 \mathbf{F}_p^{-t} - \mathbf{F}_e^t \cdot \mathbf{\Pi}^t \quad (5.19)$$

With equation (5.9) we found the material motion balance of momentum with the following format

$$\text{Div}(\psi_0 \mathbf{I} - \mathbf{F}^t \cdot \mathbf{\Pi}^t) - \mathbf{\Pi}_p^t : \nabla_X \mathbf{F}_p - \mathbf{D}_\kappa \psi_0 \nabla_X \kappa - \partial_X \psi_0 = \mathbf{0} \quad (5.20)$$

where we identify the Eshelby stress tensor $\mathbf{\Sigma}^t$ as

$$\mathbf{\Sigma}^t = \psi_0 \mathbf{I} - \mathbf{F}^t \cdot \mathbf{\Pi}^t \quad (5.21)$$

and the material volume force density as $\mathbf{B}_0 = \mathbf{B}_0^{ext} + \mathbf{B}_0^{int}$ with

$$\mathbf{B}_0^{ext} = -\mathbf{F}^t \cdot \mathbf{b}_0^{ext} \quad (5.22)$$

$$\mathbf{B}_0^{int} = -\mathbf{\Pi}_p^t : \nabla_X \mathbf{F}_p - \mathbf{D}_\kappa \psi_0 \nabla_X \kappa - \partial_X \psi_0 \quad (5.23)$$

$$= \mathbf{\Sigma}^t : [\mathbf{F}_p^{-1} \cdot \nabla_X \mathbf{F}_p] - \mathbf{D}_\kappa \psi_0 \nabla_X \kappa - \partial_X \psi_0 \quad (5.24)$$

Thus, we end up with the common format of the material motion balance of momentum

$$\text{Div} \mathbf{\Sigma}^t + \mathbf{B}_0 = \mathbf{0} \quad (5.25)$$

With this at hand we can now proceed further through the weak form and the discretization as already established in the previous chapters. The essential difference in comparison to the thermo–hyperelastic or isotropic damage case is now, that our internal material volume force \mathbf{B}_0^{int} now depends on the gradient $\nabla_X \mathbf{F}_p$. As a consequence we need an evolution law for \mathbf{F}_p within a constitutive theory. To avoid these difficulties we restrict ourselves to the geometrically linear cases of single slip crystal plasticity and von Mises plasticity with isotropic hardening. Both problems and their numerical implementations are discussed in the following two sections.

5.3 Single Crystal Plasticity

In this section we discuss theoretical and numerical results of material forces in the case of geometrically linear crystal–plasticity which based on our work published in [63].

5.3.1 Essential kinematics of crystal–plasticity

Let the position of a material particle be denoted as $\mathbf{x} \in \mathcal{B}$ and the vector $\mathbf{u}(\mathbf{x}, t)$ characterize the corresponding displacement field whereby t represents time. Furthermore, we adopt the commonly assumed additive decomposition of the displacement gradient, i.e. the distortion, into elastic and plastic parts; $\nabla \mathbf{u} = \mathbf{h} \doteq \mathbf{h}^e + \mathbf{h}^p$. Based on this, the introduction of typical strain fields is straightforward, to be specific $\boldsymbol{\varepsilon} \doteq \boldsymbol{\varepsilon}^e + \boldsymbol{\varepsilon}^p$ with $\boldsymbol{\varepsilon}^e \doteq [\mathbf{h}^e]^{\text{sym}}$, $\boldsymbol{\varepsilon}^p \doteq [\mathbf{h}^p]^{\text{sym}}$ and $[\bullet]^{\text{sym}} = \frac{1}{2} [\bullet + \bullet^t]$ whereby the notation \bullet^t abbreviates transposition.

The remaining task consists in the setup of an appropriate evolution equation for \mathbf{h}^p or rather $\boldsymbol{\varepsilon}^p$, respectively, that accounts for the underlying crystal kinematics. In this context, we adopt standard notation and let $\{\mathbf{s}_I, \mathbf{m}_I\}$ denote the slip system $I \in 1, \dots, n_{\text{sl}}$ which is determined via the slip direction \mathbf{s}_I , the normal to the slip plane \mathbf{m}_I , with $\mathbf{s}_I \perp \mathbf{m}_I$ and $\|\mathbf{s}_I\| \doteq \|\mathbf{m}_I\| = 1$ without loss of generality, and a corresponding slip parameter γ_I that is restricted by loading – and unloading conditions. With these relations at hand, we obtain the evolution equation

$$\dot{\mathbf{h}}^p = \sum_{I \in \mathcal{J}} \dot{\gamma}_I \mathbf{s}_I \otimes \mathbf{m}_I \quad \text{with} \quad \mathcal{J} = \{I \in 1, \dots, n_{\text{sl}} \mid \Phi_I = 0 \text{ and } \dot{\gamma}_I \neq 0\} \quad (5.26)$$

whereby the functions Φ_I define a (convex) admissible domain for each slip system such that \mathcal{J} collects the set of active slip systems and the notation $(\dot{\bullet})$ abbreviates derivation with respect to time.

As an interesting side aspect, we consider the integrability of the displacement field, apply Stokes theorem and observe that the plastic distortion is directly related to the elastic distortion

$$\oint_c d\mathbf{u} = \oint_c \mathbf{h} \cdot d\mathbf{x} = \int_A [\nabla \times \mathbf{h}] \cdot \mathbf{n} \, da = \int_A \mathbf{b}^{\text{bur}} \, da \doteq \mathbf{0} \quad \rightarrow \quad \nabla \times \mathbf{h}^p = -\nabla \times \mathbf{h}^e \quad (5.27)$$

with \mathbf{b}^{bur} denoting the Burgers vector of the total compatible deformation. This relation motivates the introduction of a plastic dislocation density tensor which takes with respect to eq.(5.26) the following format

$$\boldsymbol{\alpha}^{\text{p}} \doteq \nabla \times \mathbf{h}^{\text{p}} = \sum_{I \in \mathcal{J}} [\nabla \gamma_I \times \mathbf{m}_I] \otimes \mathbf{s}_I \quad (5.28)$$

and apparently incorporates the spatial gradients of the active slip parameters.

5.3.2 Standard dissipative materials

We adopted in this section the framework of standard dissipative materials as advocated by Halphen and Nguyen [34] and assume that the free Helmholtz energy is additively decomposed into a purely elastic – and hardening contributions which are defined in terms of one single hardening parameter for each slip system,

$$\psi = \psi^{\text{mac}}(\boldsymbol{\varepsilon} - \boldsymbol{\varepsilon}^{\text{p}}; \mathbf{x}) + \sum_I^{n_{\text{sl}}} \psi^{\text{har}}(\kappa_I; \mathbf{x}). \quad (5.29)$$

Based on the (isothermal) dissipation inequality and the standard argumentation of rational mechanics, hyperelastic stress formats are introduced

$$\mathcal{D} = \boldsymbol{\sigma} : \dot{\boldsymbol{\varepsilon}} - \dot{\psi} \equiv \boldsymbol{\sigma} : \dot{\boldsymbol{\varepsilon}}^{\text{p}} - \sum_I^{n_{\text{sl}}} h_I \dot{\kappa}_I \geq 0 \quad (5.30)$$

$$\boldsymbol{\sigma} \doteq \partial_{\boldsymbol{\varepsilon}} \psi^{\text{mac}} = \partial_{\boldsymbol{\varepsilon}^{\text{e}}} \psi^{\text{mac}} = -\partial_{\boldsymbol{\varepsilon}^{\text{p}}} \psi^{\text{mac}} \quad h_I \doteq \partial_{\kappa_I} \psi^{\text{har}}. \quad (5.31)$$

Furthermore, let the admissible domain of each slip system be defined by the (convex) function Φ_I which is assumed to depend on the Schmid stress τ_I and the hardening stress h_I via

$$\Phi_I(\tau_I, h_I) = |\tau_I| - [Y_0 + h_I] \leq 0 \quad \text{with} \quad \tau_I = \mathbf{s}_I \cdot \boldsymbol{\sigma} \cdot \mathbf{m}_I \quad (5.32)$$

and $0 < Y_0 = \text{const.}$ Next, associated evolution equations are introduced

$$\dot{\boldsymbol{\varepsilon}}^{\text{p}} \doteq \sum_{I \in \mathcal{J}} \dot{\lambda}_I \partial_{\boldsymbol{\sigma}} \Phi_I = \sum_{I \in \mathcal{J}} \dot{\lambda}_I \text{sign}(\tau_I) [\mathbf{s}_I \otimes \mathbf{m}_I]^{\text{sym}} \quad \dot{\kappa}_I \doteq -\dot{\lambda}_I \partial_{h_I} \Phi_I = \dot{\lambda}_I \quad (5.33)$$

with $\dot{\lambda}_I$ taking the usual interpretation as Lagrange multipliers of the corresponding constrained optimization problem. We thereby observe that the plastic strain field $\boldsymbol{\varepsilon}^{\text{p}}$ evolves independently of the sign of the slip directions \mathbf{s}_I and slip plane normals \mathbf{m}_I , respectively, and furthermore that the comparison of eq.(5.26) with eq.(5.33) results in the relation $\dot{\gamma}_I = \text{sign}(\tau_I) \dot{\lambda}_I = \text{sign}(\tau_I) \dot{\kappa}_I$ which actually stems from the chosen format in eq.(5.32). The underlying Kuhn–Tucker conditions

$$\dot{\kappa}_I \geq 0 \quad \Phi_I \leq 0 \quad \dot{\kappa}_I \Phi_I = 0 \quad (5.34)$$

allow alternative representation via the following decomposition of the domain \mathcal{B} , occupied by the body B of interest, into elastic and plastic – or rather active and inactive subdomains

$$\mathcal{B}_I^e \cup \mathcal{B}_I^p = \mathcal{B} \quad \mathcal{B}_I^e \cap \mathcal{B}_I^p = \emptyset \quad \bigcup_{I=1}^{n_{sl}} \mathcal{B}_I^p = \mathcal{B}^p \quad \text{with} \quad (5.35)$$

$$\mathcal{B}_I^e = \{\mathbf{x} \in \mathcal{B} \mid \Phi_I \leq 0, \dot{\kappa}_I = 0\} \quad \mathcal{B}_I^p = \{\mathbf{x} \in \mathcal{B} \mid \Phi_I = 0, \dot{\kappa}_I > 0\}. \quad (5.36)$$

With these relations in hand, the corresponding Eshelby–type stress field and volume force read

$$\boldsymbol{\Sigma}^t = \psi \mathbf{I} - \mathbf{h}^t \cdot \boldsymbol{\sigma} \quad \mathbf{B} = \sum_I^{n_{sl}} [\tau_I \nabla \gamma_I - h_I \nabla \kappa_I] - \partial_{\mathbf{x}} \psi - \mathbf{h}^t \cdot \mathbf{b} \quad (5.37)$$

whereby the relation $-\partial_{\boldsymbol{\varepsilon}^p} \psi^{\text{mac}} : \nabla \boldsymbol{\varepsilon}^p = \boldsymbol{\sigma} : [\sum_I^{n_{sl}} \mathbf{s}_I \otimes \mathbf{m}_I \otimes \nabla \gamma_I] = \sum_I^{n_{sl}} \tau_I \nabla \gamma_I$ as well as the underlying compatibility condition have been incorporated and \mathbf{I} denotes the second order identity. Please note that \mathbf{B} depends on the spatial gradient of the slip and hardening parameters and, moreover, that for monotonic loading conditions the contributions $\tau_I \nabla \gamma_I - h_I \nabla \kappa_I$ to the Eshelby–type volume force boil down to $[|\tau_I| - h_I] \nabla \kappa_I$ which are additionally bounded by the yield function (5.32), namely $|\tau_I| - h_I \leq Y_0$.

5.3.3 Numerical solution strategies

While the introduction and computational treatment of the weak form (equality) of the balance of linear momentum is straightforward

$$G^u(\mathbf{u}, \kappa_I; \delta \mathbf{u}) = \int_{\partial \mathcal{B}^t} \delta \mathbf{u} \cdot \mathbf{t}^{\text{pr}} \, da + \int_{\mathcal{B}} \delta \mathbf{u} \cdot \mathbf{b} - \nabla \delta \mathbf{u} : \boldsymbol{\sigma} \, dv = 0 \quad \forall \delta \mathbf{u} \in H_0^1(\mathcal{B}) \quad (5.38)$$

the Kuhn–Tucker conditions can either be realized via the following weak form relations (inequalities)

$$G_I^\Phi(\mathbf{u}, \kappa_I; \delta \kappa_I) = \int_{\mathcal{B}} \delta \kappa_I [|\tau_I| - Y_0 - h_I] \, dv \leq 0 \quad \forall \delta \kappa_I > 0 \in L_2(\mathcal{B}) \quad (5.39)$$

$$\dot{G}_I^\kappa(\dot{\kappa}_I; \delta \Phi_I) = \int_{\mathcal{B}} \delta \Phi_I \dot{\kappa}_I \, dv \geq 0 \quad \forall \delta \Phi_I > 0 \in L_2(\mathcal{B}) \quad (5.40)$$

or within the standard internal variable approach. In analogy to eq.(5.36) the elastic and plastic subdomains allow the alternative representation

$$\mathcal{B}_I^e = \left\{ \mathbf{x} \in \mathcal{B} \mid G_I^\Phi \leq 0, \dot{G}_I^\kappa = 0 \quad \forall \delta \kappa_I, \delta \Phi_I > 0 \in L_2(\mathcal{B}_I^e) \right\}, \quad (5.41)$$

$$\mathcal{B}_I^p = \left\{ \mathbf{x} \in \mathcal{B} \mid G_I^\Phi = 0, \dot{G}_I^\kappa > 0 \quad \forall \delta \kappa_I, \delta \Phi_I > 0 \in L_2(\mathcal{B}_I^p) \right\}. \quad (5.42)$$

Please note that eqs.(5.39,5.40) constitute the weighted format of the yield function in eq.(5.32) and the evolution of the hardening parameters under the constraints imposed by the Kuhn–Tucker conditions as highlighted in eq.(5.34). The first approach (i.e. eqs.(5.39,5.40)), where the Kuhn–Tucker conditions are evaluated on the global finite element level, is denoted as node point based and the second framework, where the Kuhn–Tucker conditions are evaluated on a pointwise or rather local level, is classified as integration point based. Their particular properties are discussed below. For conceptual clarity we restrict ourselves to the specific case of single–slip crystal–plasticity in the progression of this work, i.e. $n_{sl} \doteq 1$ such that the index I can be dropped.

Node point based approach

After the temporal and spatial discretization of the weak forms in eqs.(5.38,5.39) are carried out one obtains the residua \mathbf{R}_K^u and $R_K^\phi \forall K \in \mathbb{B}$ whereby K denotes the index of a finite element node in the discretization domain \mathbb{B} , see appendix D.1 for a brief reiteration. The contribution from eq.(5.40), i.e. ΔR_K^κ is incorporated into the following active set search:

The initialization consists in the obvious choice that the active domain corresponds to those nodes where the (representation of the) yield function is violated and the initial – or rather trial step for the hardening parameter follows straightforward

$$\mathbb{B}_{\text{act}} = \{ K \in \mathbb{B} \mid R_K^\phi > 0 \} \quad \kappa_K^{\text{trial}} = \kappa_{K n} + \Delta \kappa_K \forall K \in \mathbb{B}_{\text{act}}. \quad (5.43)$$

Since the incremental field $\Delta \kappa_K$ might become negative, which is not admissible due to eqs.(5.34,5.40), we have to incorporate an additional projection to the admissible range of κ_K or rather restrict the evolution of κ_K via $\kappa_{K n+1} \doteq \max\{\kappa_K^{\text{trial}}, \kappa_{K n}\}$. The active working set is then defined by

$$\mathbb{B}_{\text{act}} = \mathbb{B}_{\text{act}}^\phi \cup \mathbb{B}_{\text{act}}^p \quad \mathbb{B}_{\text{act}}^\phi = \{ K \in \mathbb{B} \mid R_K^\phi > 0 \} \quad \mathbb{B}_{\text{act}}^p = \{ K \in \mathbb{B} \mid \Delta R_K^\kappa > 0 \} \quad (5.44)$$

and convergence is obtained for $\mathbb{B}_{\text{act}}^\phi = \emptyset$ such that $\mathbb{B}_{\text{act}} = \mathbb{B}_{\text{act}}^p \rightarrow \mathbb{B}_{n+1}^p$. Finally note that the computation of the spatial gradient of the hardening parameter is straightforward and performed on the element level via the spatial gradients of the shape functions N_κ^k , i.e. $\nabla \kappa^h = \sum_{k=1}^{n_{\text{en}}} \kappa_k \nabla N_\kappa^k$. Similarly, the update for the slip parameter γ reads $\gamma_{K n+1} = \gamma_{K n} + s_K \Delta \kappa_K$ and $s_K = \text{sign}(\mathbf{A}_{e=1}^{n_{\text{el}}} \int_{\mathcal{B}^e} N_\kappa^k \tau^h dv)$ such that with these nodal values at hand the computation of the corresponding spatial gradient results in $\nabla \gamma^h = \sum_{k=1}^{n_{\text{en}}} \gamma_k \nabla N_\kappa^k$.

Integration point based approach

For the integration point based – or rather standard internal variable approach the hardening variables and slip parameters are, by definition of the algorithm, only available at the integration points, see appendix D.2 for further details on the underlying formulation. We therefore have to apply a projection – or in other words smoothing algorithm to

the hardening variables and slip parameters in order to compute these fields at the node point level which then enables us to calculate their spatial gradients via the gradients of the shape functions. Adopting standard algorithms, the corresponding least square approximation yields

$$\int_{\mathcal{B}} \frac{1}{2} [\kappa^{\text{pro}} - \kappa^h]^2 dv \rightarrow \min \quad \int_{\mathcal{B}} \delta \kappa^{\text{pro}} [\kappa^{\text{pro}} - \kappa^h] dv = 0 \quad (5.45)$$

whereby $\kappa^{\text{pro}} = \sum_{l=1}^{n_{\text{en}}} N_{\kappa}^l \kappa_l^{\text{pro}}$ denotes the projected field and κ^h characterizes the field sampled at the integration points; apparently the identical scheme can be applied to the projection of the slip parameters γ . A straightforward interpolation technique which guarantees C^0 continuity is e.g.

$$\kappa_k^{\text{pro}} = \left[\mathbf{A}_{e=1}^{n_{\text{el}}} \int_{\mathcal{B}^e} N_{\kappa}^k N_{\kappa}^l dv \right]^{-1} \mathbf{A}_{e=1}^{n_{\text{el}}} \int_{\mathcal{B}^e} N_{\kappa}^l \kappa^h dv \quad (5.46)$$

with the notation $[\bullet]$ indicating a lumped matrix format and the identical scheme holding for γ_k^{pro} , respectively. The computation of the sought gradients follows in analogy to the node point based setting, namely $\nabla \kappa^h = \sum_{k=1}^{n_{\text{en}}} \kappa_k^{\text{pro}} \nabla N_{\kappa}^k$ and $\nabla \gamma^h = \sum_{k=1}^{n_{\text{en}}} \gamma_k^{\text{pro}} \nabla N_{\kappa}^k$.

5.3.4 Examples

The subsequent numerical examples are based on rather elementary constitutive functions, i.e. a quadratic format for the elastic and hardening contribution of the free Helmholtz energy is adopted

$$\psi^{\text{mac}}(\boldsymbol{\varepsilon}^e; \mathbf{x}) = \frac{1}{2} L [\boldsymbol{\varepsilon}^e : \mathbf{I}]^2 + G [\boldsymbol{\varepsilon}^e]^2 : \mathbf{I} \quad \psi^{\text{har}}(\kappa; \mathbf{x}) = \frac{1}{2} H \kappa^2. \quad (5.47)$$

Material parameters that reflect the behavior of (single-crystalline) elastoplastic metals are applied throughout; $E = 60000$ MPa, $\nu = 0.3$, $H = 6000$ MPa, $Y_0 = 60$ MPa with $L = \frac{E\nu}{[1+\nu][1-2\nu]}$ and $G = \frac{E}{2[1+\nu]}$ being obvious. For the definition of the slip system we choose $\mathbf{m} = -0.5 \mathbf{e}_1 + 0.866 \mathbf{e}_2$ such that $\angle(\mathbf{m}, \mathbf{e}_1) = 120^\circ$ whereby the base vectors \mathbf{e}_i represent a Cartesian frame. We discuss three different numerical examples under plane strain conditions in the sequel and thereby start with an inhomogeneous specimen represented by an elliptic inclusion, then switch to a specimen with an elliptic hole and finally consider a cracked specimen. The inhomogeneity due to the inclusion stems from a modified orientation of the slip system, namely $\mathbf{m}^{\text{inc}} = -0.866 \mathbf{e}_1 + 0.5 \mathbf{e}_2$ such that $\angle(\mathbf{m}^{\text{inc}}, \mathbf{e}_1) = 150^\circ$. Any assumption on plane strain or plane stress conditions is therefore not affected by the plastic strains, since $\mathbf{e}_3 \cdot \mathbf{s} = \mathbf{e}_3 \cdot \mathbf{m} = 0$, but solely reflected via the elastic portions.

For comparison reasons, similar finite element techniques are applied to the node – and integration point based approach. To be specific, for the first framework a C^0 , C^0 approximation of $Q1$, $Q1$ type for the displacement and hardening field \mathbf{u} , κ is chosen and consequently the latter framework is realized via a C^0 approximation of $Q1$ type for the displacement field \mathbf{u} .

Specimen with an elliptic inclusion

The initial state of the considered specimen is completely homogeneous since the inclusion possesses identical elastic properties as the ambient material. Taking a tension-type loading path into account (which is chosen to be displacement driven for the subsequent numerical example), we observe that the elastic status boils down to a one-dimensional setting as the transverse stretch is not constrained by the applied boundary conditions. For the particular choice of the orientations of the slip systems it turns out that the yield limit is achieved simultaneously in the entire body, and that the non-homogeneity occurs only for inelastic deformation processes. Apparently, this non-homogeneity stems from the application of varying material parameters in different domains (here the orientation of slip systems) as well as the formation of non-homogeneous contributions of the hardening field, which is often classified as the heterogeneity of the solution.

The geometry of the specimen is visualized in figure 5.2 and corresponds to the dimensions 60×20 . Moreover, the discretization is performed by 1152 elements whereby 384 elements are attached to the elliptic inclusion which is of dimension 5×10 . Apparently, the (longitudinal) load \vs (prescribed) displacement curves in figure 5.2 monitor, as far as the eye can catch, identical results for the node point based – and integration point based approach. Figures 5.3 and 5.4 highlight the contributions of the material internal –, volume – and surface forces $\mathbf{F}_{\text{int, vol, sur } K}^h$ as well as the hardening variable κ for a prescribed displacement of $u^{\text{Pr}} = 0.2$ at the ending of the specimen. It thereby turns out that the material internal forces and the material volume contributions, which obviously stem from the non-vanishing spatial gradient of the hardening variables and slip parameters, almost cancel out – except at the transition zone from the ambient body to the inclusion. Moreover, this inhomogeneity or rather heterogeneity of the material is also clearly monitored by the visualization of the hardening variable. Finally, we observe that figures 5.3 and 5.4 show only minor differences, i.e. the node point based – and integration point based approach end up with qualitatively similar results.

Specimen with an elliptic hole

In contrast to the previous setting it is now the incorporation of an elliptic hole which causes, even in the elastic range, an inhomogeneously deformed state. Due to the resulting stress intensities plastic zones start to develop in a symmetric arrangement but then further progress in a non-symmetric pattern since the slip system is not aligned with the longitudinal loading direction.

In analogy to section 5.3.4 we consider once more a specimen characterized by the same geometry (with identical boundary and loading conditions) whereby the discretization is realized via 48×16 elements, compare figure 5.5. Again, the (longitudinal) load \vs (prescribed) displacement curves for the node point based – and integration point based approach come up with (almost) identical results, see figure 5.5. Furthermore, the calculated material internal –, volume – and surface forces $\mathbf{F}_{\text{int, vol, sur } K}^h$ and the hardening

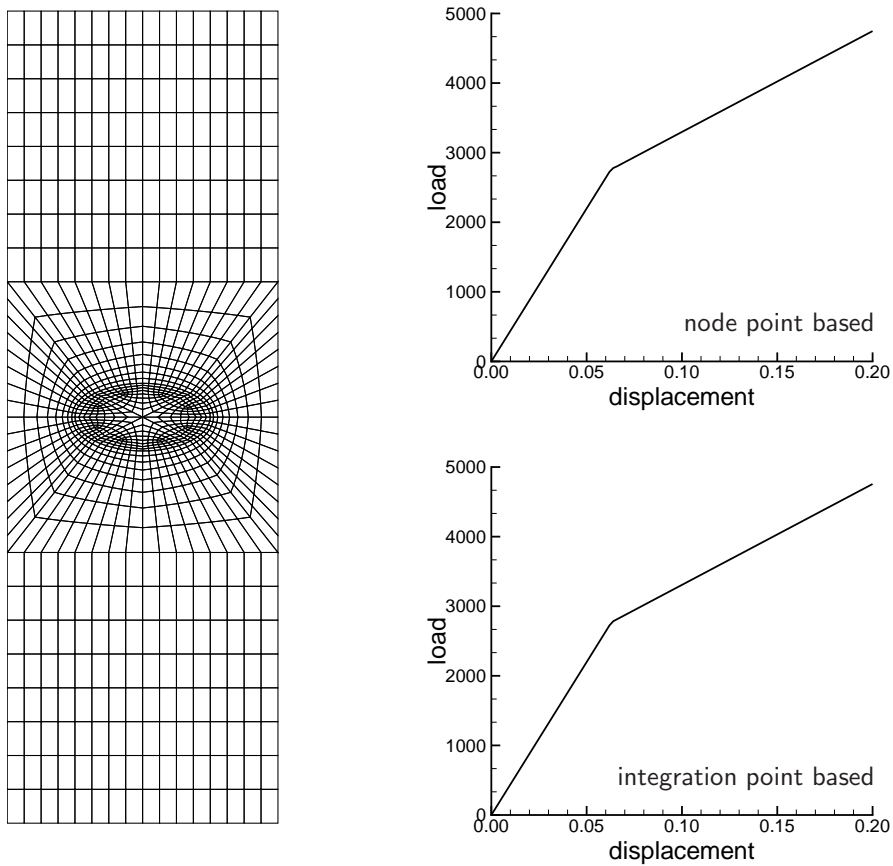


Figure 5.2. Specimen with an elliptic inclusion: Discretization and (longitudinal) load \vs (prescribed) displacement curves for the node point based – and integration point based approach.

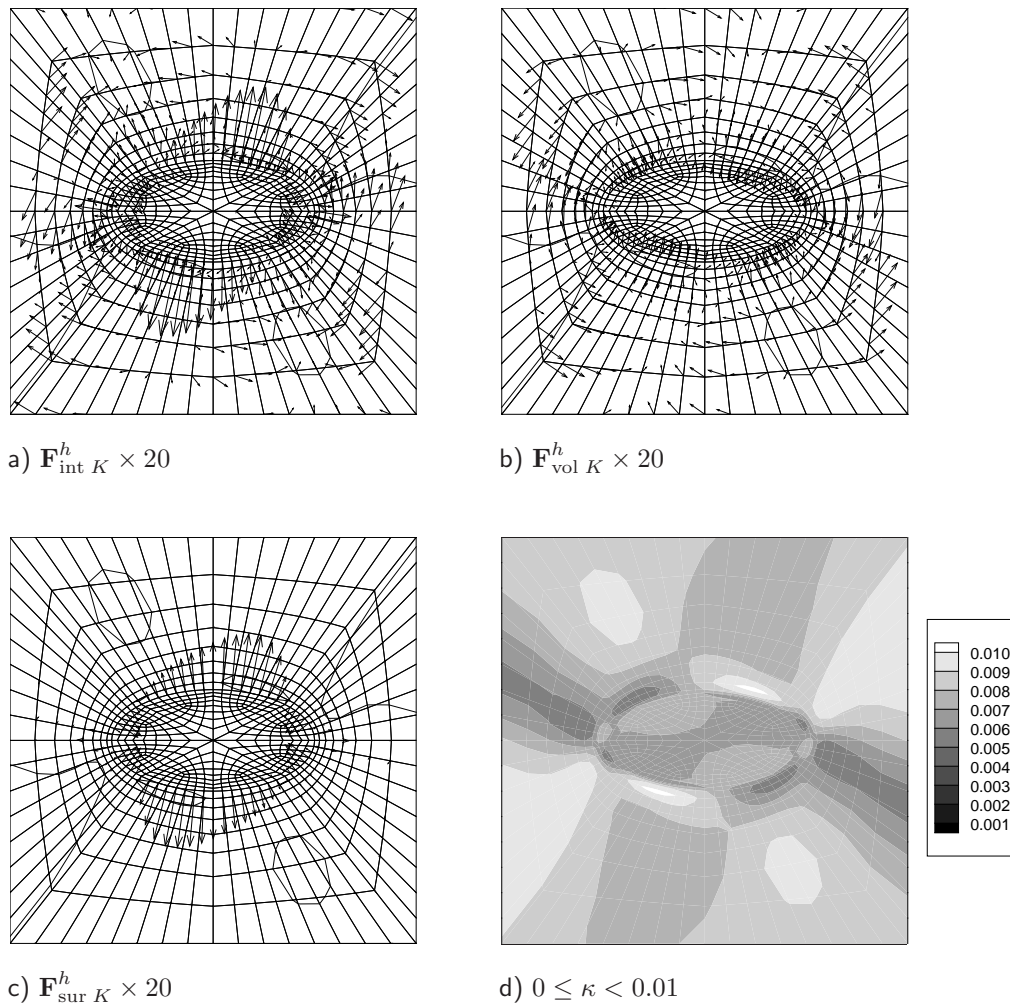


Figure 5.3. Specimen with an elliptic inclusion: a) $\mathbf{F}_{\text{int } K}^h$, b) $\mathbf{F}_{\text{vol } K}^h$, c) $\mathbf{F}_{\text{sur } K}^h$ and d) κ for the node point based approach ambient of the inclusion at $u^{\text{pr}} = 0.2$.

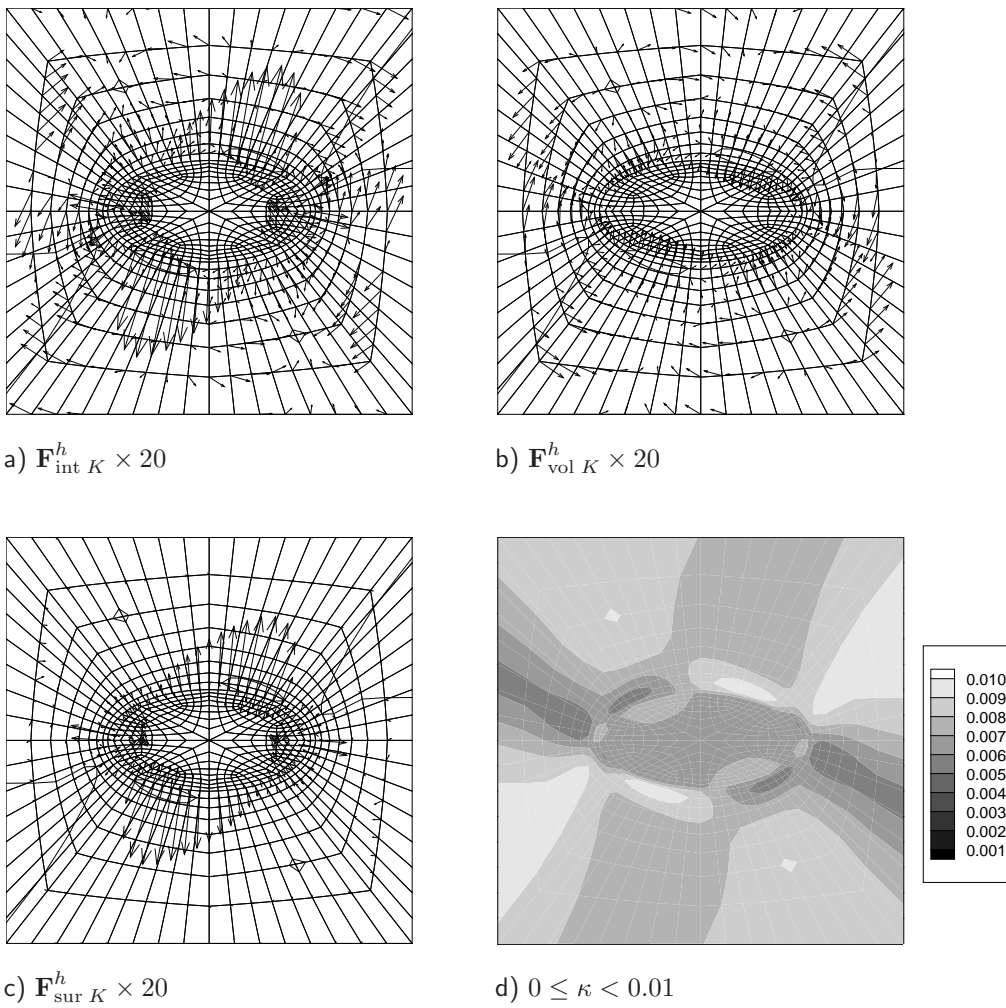


Figure 5.4. Specimen with an elliptic inclusion: a) $\mathbf{F}_{\text{int } K}^h$, b) $\mathbf{F}_{\text{vol } K}^h$, c) $\mathbf{F}_{\text{sur } K}^h$ and d) κ for the integration point based approach ambient of the inclusion at $u^{\text{pr}} = 0.2$.

variable κ are monitored in figures 5.6 and 5.7 at $u^{\text{pr}} = 0.2$. Apparently, similar results are obtained for the node point based – and integration point based approach. The overall anisotropic response is thereby clearly underlined by the plots of the hardening field.

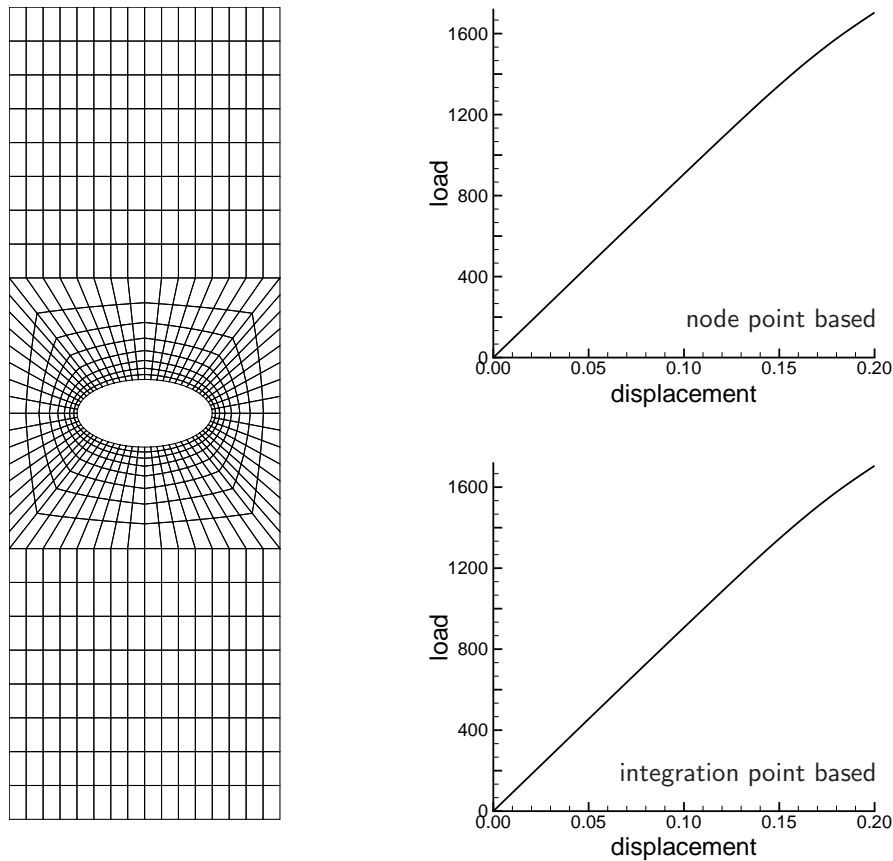


Figure 5.5. Specimen with an elliptic hole: Discretization and (longitudinal) load \vs (prescribed) displacement curves for the node point based – and integration point based approach.

Specimen with a crack

Finally, we consider a cracked specimen under mode I loading which is directly related to the well-known $r^{-1/2}$ singularity of an isotropic linear elastic setting. Due to this stress intensity the plastic zone starts to develop at the crack tip and then progresses in a non-symmetric pattern since the slip system is not aligned with the loading direction. To be specific, a circular subdomain, with radius $R = 150$ (and $H^{\text{crack}} = H \times 10^{-2}$), of the infinitely expanded body is taken into account and the discretization is performed with 38×24 elements, see e.g. figure 5.8. The 38 rings are thereby arranged (in radial direction) in a geometrical series and the ring at the crack tip consists of $P1$, $P1$ triangular elements for the approximation of the displacement – and hardening field, respectively.

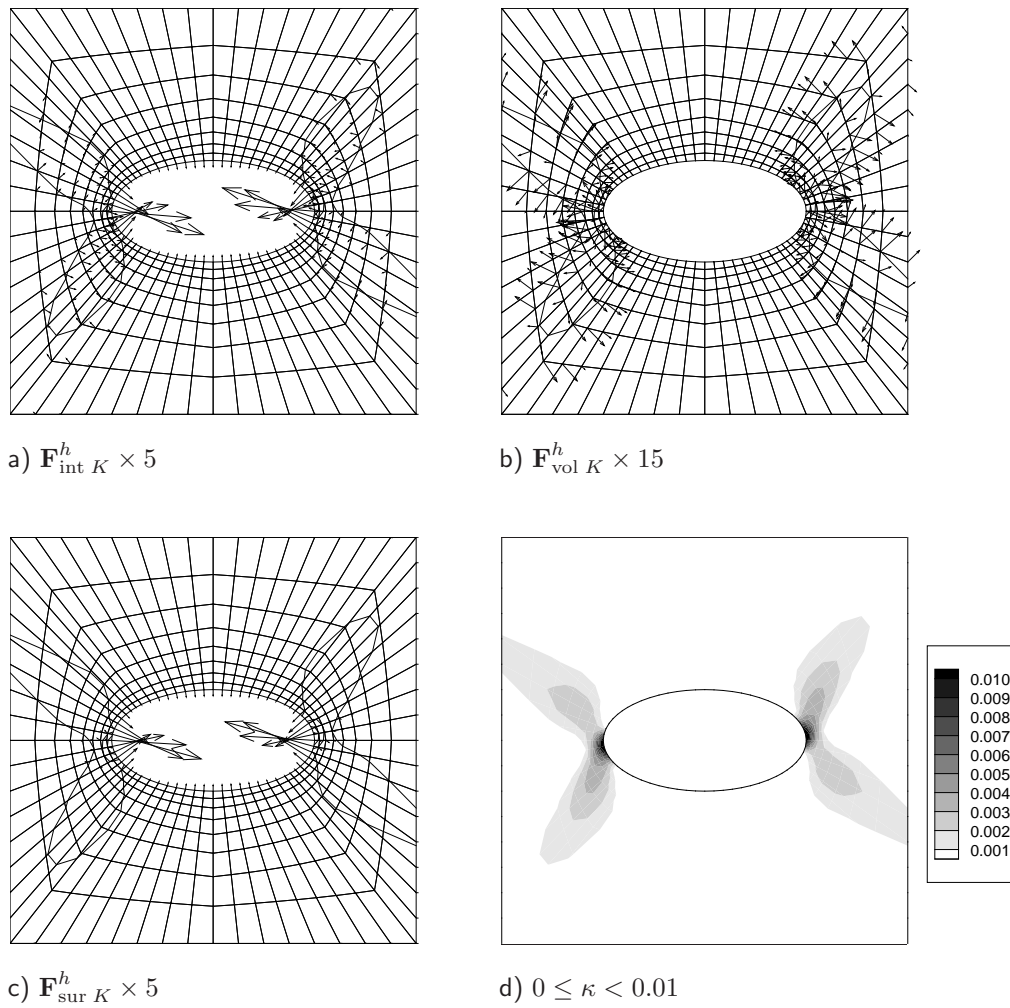


Figure 5.6. Specimen with an elliptic hole: a) $\mathbf{F}_{\text{int } K}^h$, b) $\mathbf{F}_{\text{vol } K}^h$, c) $\mathbf{F}_{\text{sur } K}^h$ and d) κ for the node point based approach ambient of the hole at $u^{\text{pr}} = 0.2$.

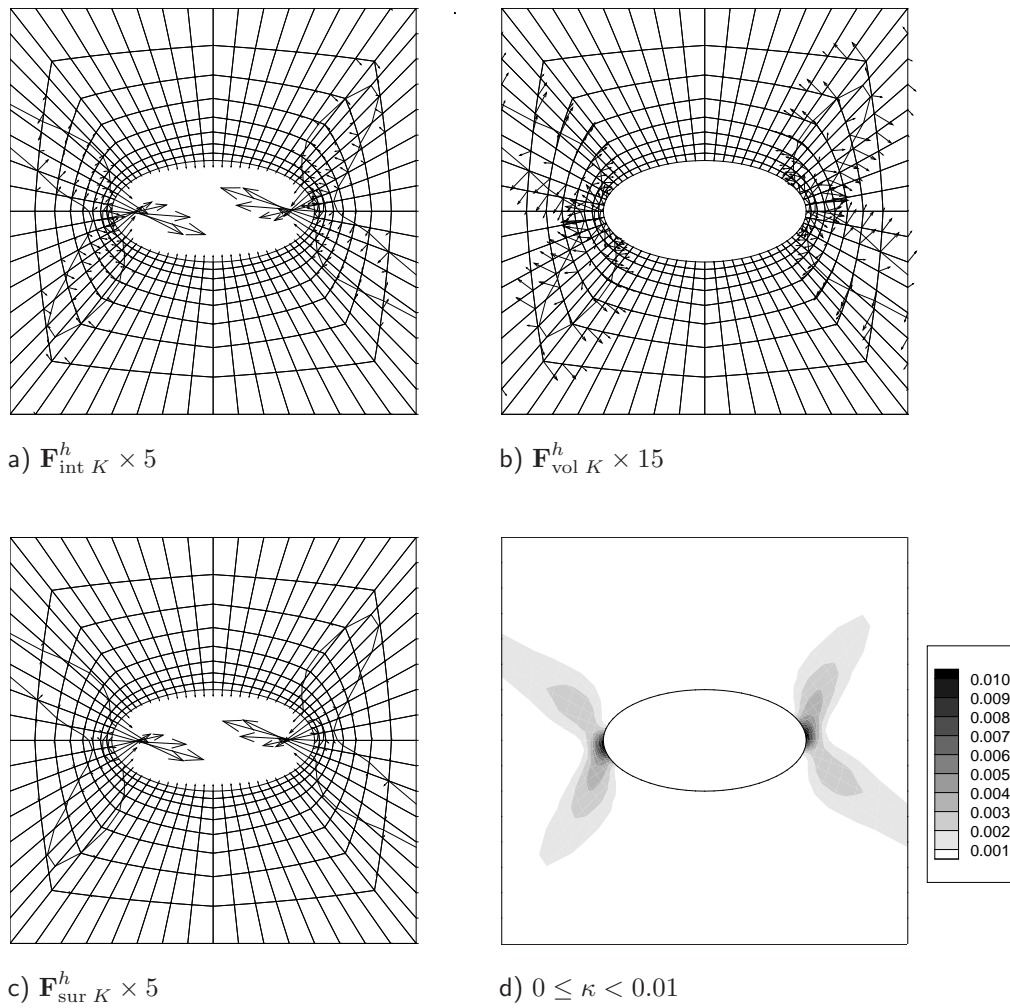


Figure 5.7. Specimen with an elliptic hole: a) $\mathbf{F}_{\text{int } K}^h$, b) $\mathbf{F}_{\text{vol } K}^h$, c) $\mathbf{F}_{\text{sur } K}^h$ and d) κ for the integration point based approach ambient of the hole at $u^{\text{PF}} = 0.2$.

Due to the plastic anisotropy of the material the vectorial J–integral is not entirely aligned with the crack direction, compare figures 5.9c) and 5.10c). However, in order to compare the computation of the vectorial J–integral, as based on the developed formulation, with the (analytical) solution for an isotropic linear elastic setting we highlight solely the component of \mathbf{J}^h in the direction of the crack. Consequently, the boundary conditions have to be chosen such that mode I loading is recovered, i.e. for a given J–integral with respect to an isotropic linear elastic setting, say J_e^{pr} , we obtain the related prescribed displacement field at the boundary of the outer ring; for a detailed outline the reader is referred to, e.g., Williams [108]. Moreover, the accuracy of the approximation of \mathbf{J}^h depends on the considered domain, which is highlighted in figure 5.8 for $J_e^{\text{pr}} = 0.49$. The obtained results are thereby normalized with respect to the corresponding (analytical) solution of the isotropic linear elastic setting which rests upon the idea that the plastic zone is relatively small compared to the considered domain. Furthermore, note that specialized finite elements at the crack tip, which are not in the focus of this work, would not considerably improve the solution of this inelastic setting. The computations based on the node point based – and integration point based approach however, once more end up with similar results, see again figure 5.8. In contrast to the example in section 5.3.4 and especially the one in section 5.3.4 we observe that the material volume forces are now less pronounced (as indicated by a higher scaling factor), see figures 5.9 and 5.10 where the material forces and the hardening field are highlighted for $J_e^{\text{pr}} = 0.49$ in analogy to the previous settings. Once more, the node point based – and integration point based approach render similar results with only minor differences.

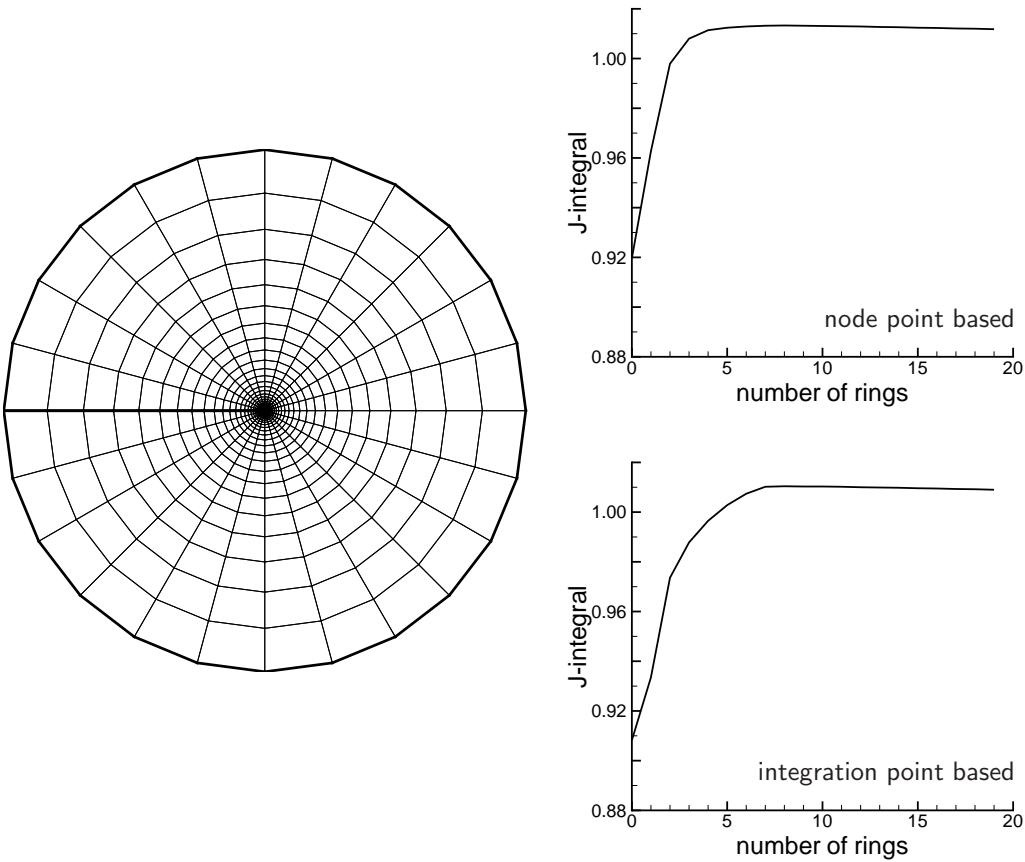


Figure 5.8. Specimen with a crack: Discretization and J-integral \vs number of rings for the node point based – and integration point based approach at $J_e^{Pr} = 0.49$.

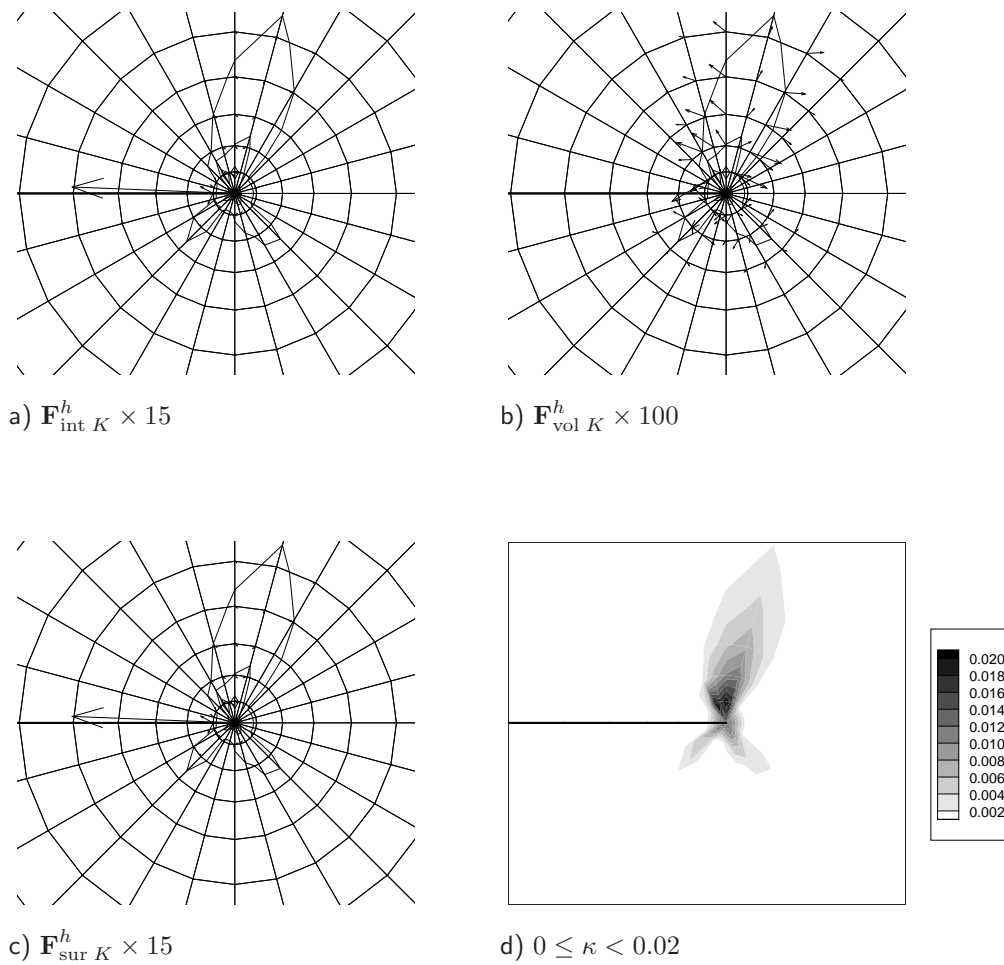


Figure 5.9. Specimen with a crack: a) $\mathbf{F}_{\text{int } K}^h$, b) $\mathbf{F}_{\text{vol } K}^h$, c) $\mathbf{F}_{\text{sur } K}^h$ and d) κ for the node point based approach ambient of the crack at $J_e^{\text{pr}} = 0.49$.

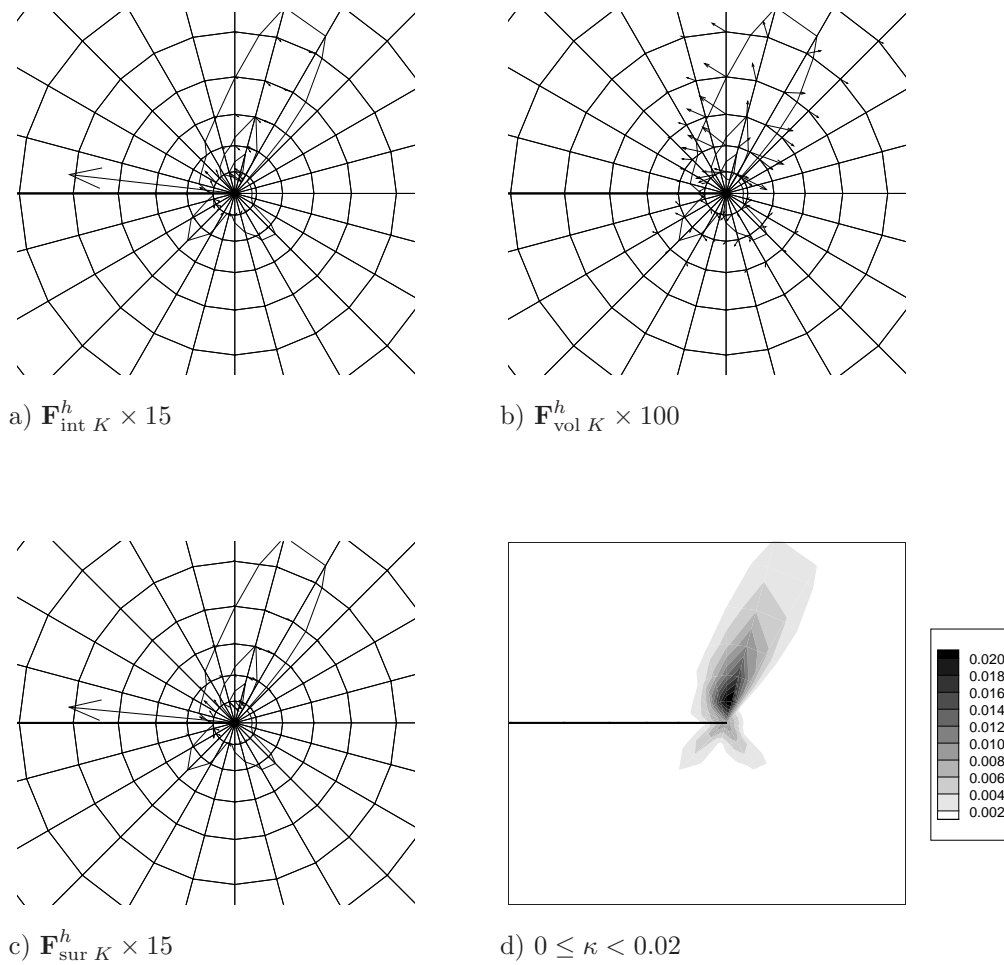


Figure 5.10. Specimen with a crack: a) $\mathbf{F}_{\text{int } K}^h$, b) $\mathbf{F}_{\text{vol } K}^h$, c) $\mathbf{F}_{\text{sur } K}^h$ and d) κ for the integration point based approach ambient of the crack at $J_e^{\text{PF}} = 0.49$.

5.4 Von Mises plasticity

Based on the theoretical results of the previous section we are able to formulate the material force method for geometrically linear von Mises type plasticity model. We restrict ourselves to a simple prototype model with linear isotropic hardening behaviour, as defined by the following free Helmholtz energy function

$$\psi^e(\boldsymbol{\varepsilon}^e) = \frac{1}{2} K [\boldsymbol{\varepsilon}^e : \mathbf{I}]^2 + G [\boldsymbol{\varepsilon}^{dev}]^2 : \mathbf{I} \quad \psi^{har}(\kappa) = \frac{1}{2} H \kappa^2 \quad (5.48)$$

Because we already discussed 'Standard dissipative materials' in section 5.3.2 we discuss the relevant equations only briefly in the sequel.

The (isothermal) dissipation inequality

$$\mathcal{D}^{red} = \boldsymbol{\sigma} : \dot{\boldsymbol{\varepsilon}}^p + R \dot{\kappa} \geq 0 \quad (5.49)$$

leads to the hyperelastic stress

$$\boldsymbol{\sigma} = \partial_{\boldsymbol{\varepsilon}^e} \psi^e = -\partial_{\boldsymbol{\varepsilon}^p} \psi^e. \quad (5.50)$$

We furthermore introduce a yield function and the hardening stress by

$$\Phi(\boldsymbol{\sigma}, R) = \|\boldsymbol{\sigma}^{dev}\| - \sqrt{2/3} [Y_0 - R] \leq 0 \quad \text{and} \quad R = -\partial_{\kappa} \psi \quad (5.51)$$

The postulate of maximum dissipation results in the associated evolution equation for the plastic strain

$$\dot{\boldsymbol{\varepsilon}}^p = \dot{\lambda} \mathbf{n} \quad \dot{\kappa} = \dot{\lambda} \sqrt{2/3} \quad \mathbf{n} = \boldsymbol{\sigma}^{dev} / \|\boldsymbol{\sigma}^{dev}\|. \quad (5.52)$$

and the Kuhn-Tucker loading and unloading conditions

$$\dot{\lambda} \geq 0 \quad \Phi \leq 0 \quad \dot{\lambda} \Phi = 0 \quad (5.53)$$

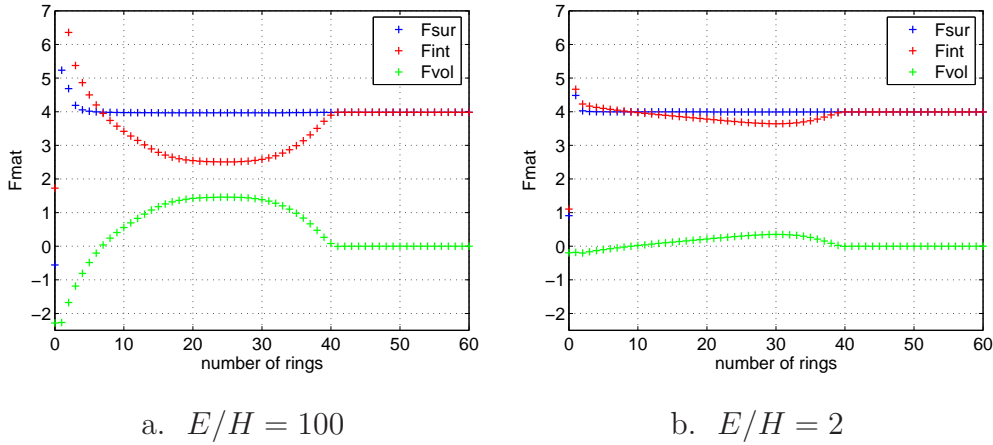
The numerical implementation of this model is described e.g. by Simo [91] and should not be discussed here.

Iterating through the equations in section 2.5, page 27, gives us the Eshelby stress tensor and the material volume force as

$$\boldsymbol{\Sigma}^t = \psi \mathbf{I} - \mathbf{h}^t \cdot \boldsymbol{\sigma} \quad (5.54)$$

$$\mathbf{B} = \boldsymbol{\sigma} : \nabla_x \boldsymbol{\varepsilon}^p - R \nabla_x \kappa - \partial_x \psi - \mathbf{h}^t \cdot \mathbf{b}. \quad (5.55)$$

We can split the material volume force in an external and an internal part $\mathbf{B} = \mathbf{B}^{ext} + \mathbf{B}^{int}$ with

Figure 5.11. Material forces for T -stress $\tau = -0.9$

$$\mathbf{B}^{ext} = -\mathbf{h}^t \cdot \mathbf{b} \quad (5.56)$$

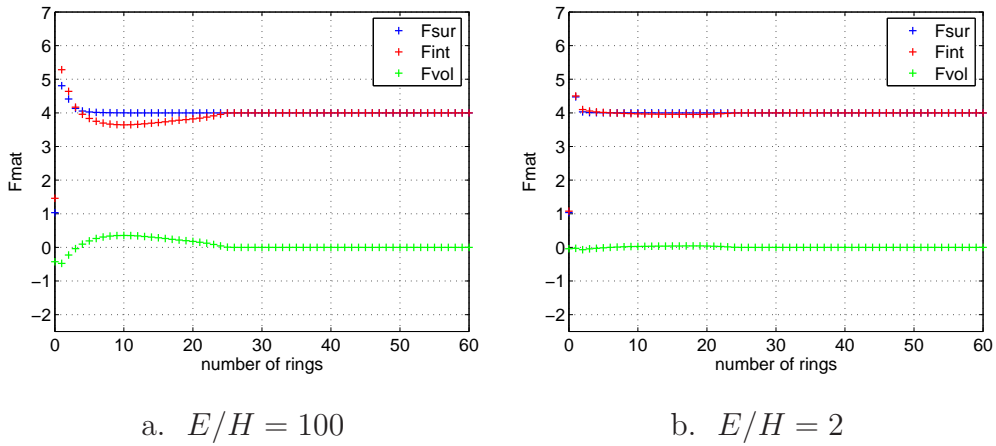
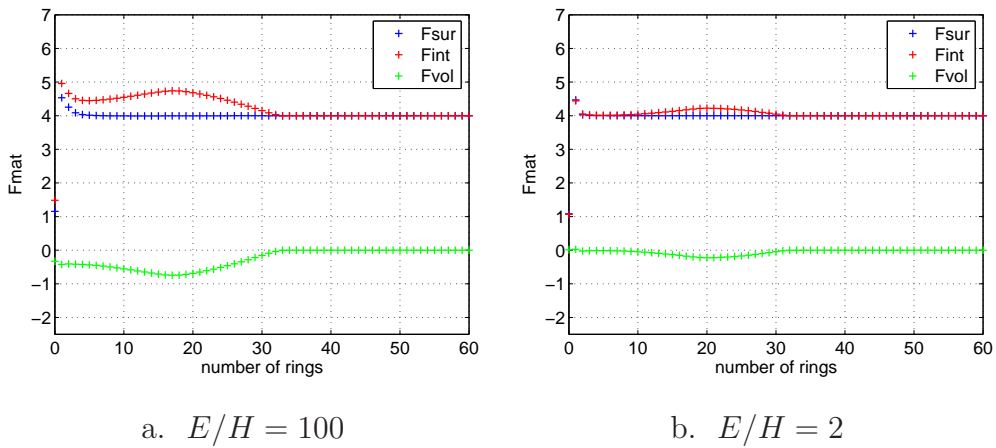
$$\mathbf{B}^{int} = \boldsymbol{\sigma} : \nabla_x \boldsymbol{\varepsilon}^p - R \nabla_x \kappa - \partial_x \psi. \quad (5.57)$$

The internal part of the material volume force \mathbf{B}^{int} is also called a 'dissipative' volume force, see Maugin [57]. To determine \mathbf{B}^{int} we need the gradients $\nabla_x \boldsymbol{\varepsilon}^p$ and $\nabla_x \kappa$. Both are calculated numerically by the integration point based method already outlined in the previous section 5.3.3 based on a L_2 -projection of the values $\boldsymbol{\varepsilon}^p$ and κ available at the integration points.

As a numerical example we study a 'Modified Boundary Layer'-formulation of a straight traction free crack in a von Mises plasticity type material. The example is similar to those given in section 2.6.1, page 28. We load the isolated crack tip region with a prescribed boundary condition which belongs to a prescribed J -integral value of $J_{pre} = 4$. This guarantees us 'Small Scale Yielding' (SSY) conditions based on the asymptotic linear elastic solution under mode I loading.

We varied the T -stress in the range of $\tau = T/Y_0 = -0.9, 0.0, 0.9$ and as a hardening modul we choose the ratio $E/H = 100$ and $E/H = 2$. The Young's modulus was set to $E = 72000$ MPa, the Poisson's ratio to $\nu = 0.3$ and the yield stress to $Y_0 = 317$ MPa. The resulting discrete material (surface) forces $\mathbf{F}_{sur K}^h$ and their internal and volume parts as well as the internal variable κ are shown in fig. 5.14 to 5.19.

To study the domain dependency of the J -integral we use our in eq. 2.41 proposed Material Force Method. In this case we increase our integration domain not starting at the crack tip node but at the outer boundary of the discretized region. That means due to the chosen SSY-condition we start our integration in the elastic region where we found the prescribed J -integral value with an error less than 0.1%. Thus the in fig. 5.11 to 5.13 depicted graphs should be read from right to left. Especially for large negative T -stress the influence of

Figure 5.12. Material forces for T -stress $\tau = 0.0$ Figure 5.13. Material forces for T -stress $\tau = 0.9$

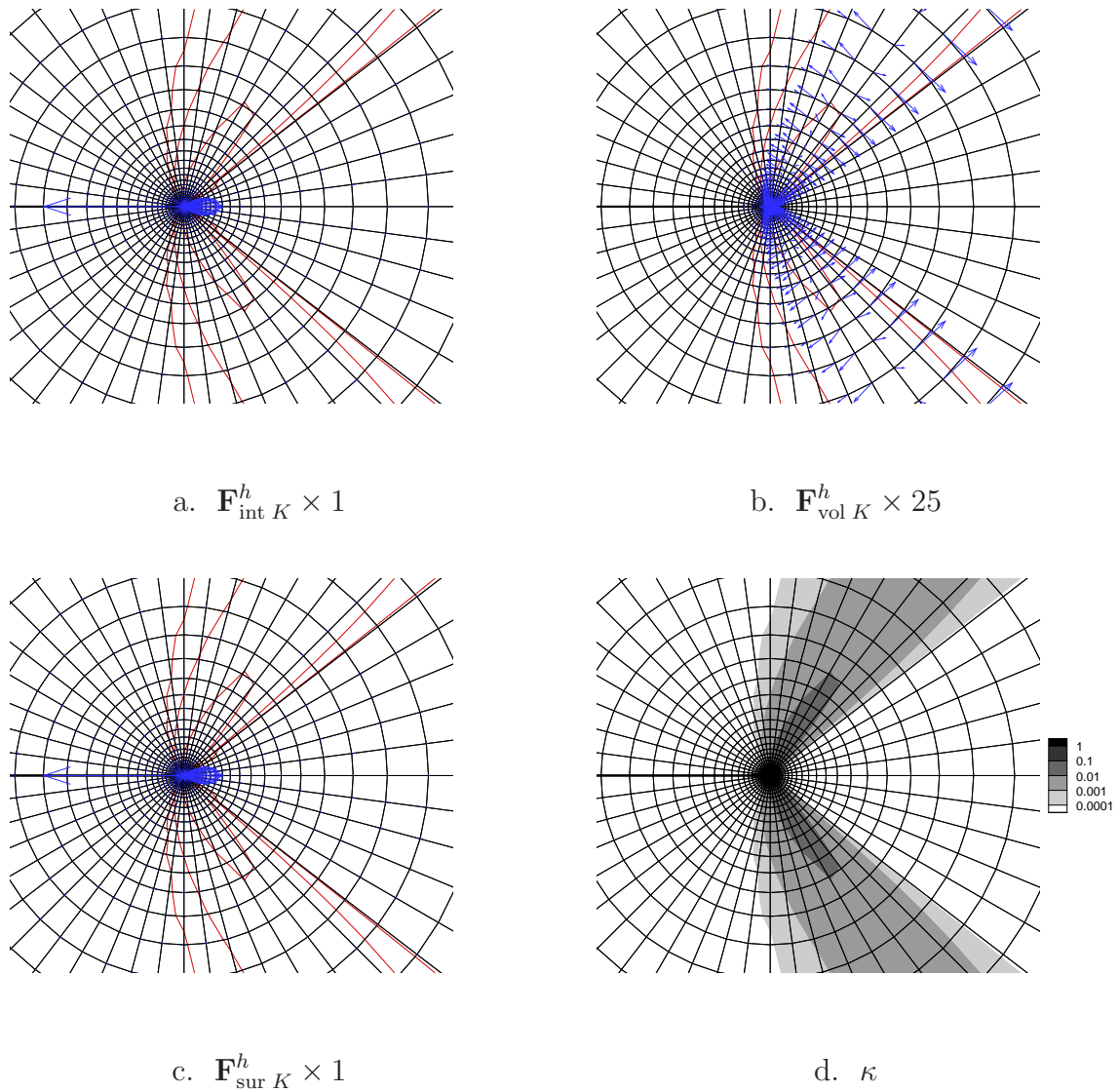
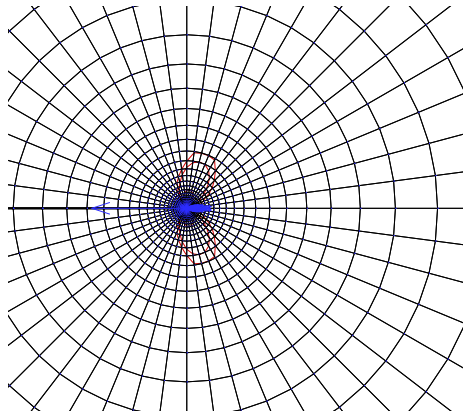
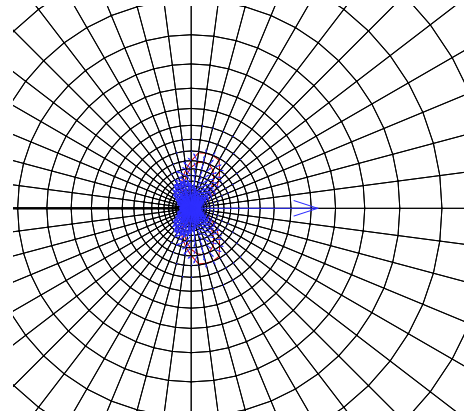
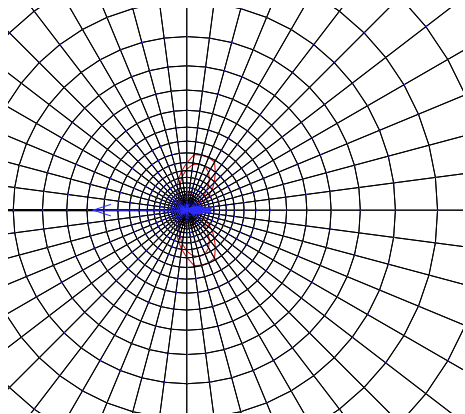
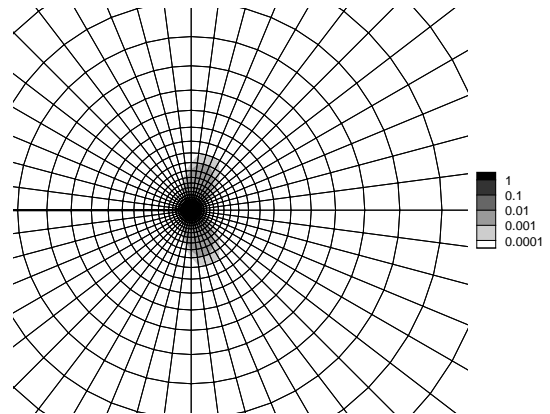


Figure 5.14. Material forces for T -stress $\tau = -0.9$ and $E/H = 100$

the 'dissipative' material volume forces are considerably strong, see fig. 5.14. Whereas in the case of vanishing or positive T -stresses we observe a much less influence. Additionally, we found that small hardening moduli H results in larger 'dissipative' material volume forces.

a. $\mathbf{F}_{\text{int}}^h K \times 1$ b. $\mathbf{F}_{\text{vol}}^h K \times 100$ c. $\mathbf{F}_{\text{sur}}^h K \times 1$ d. κ Figure 5.15. Material forces for T -stress $\tau = 0.0$ and $E/H = 100$

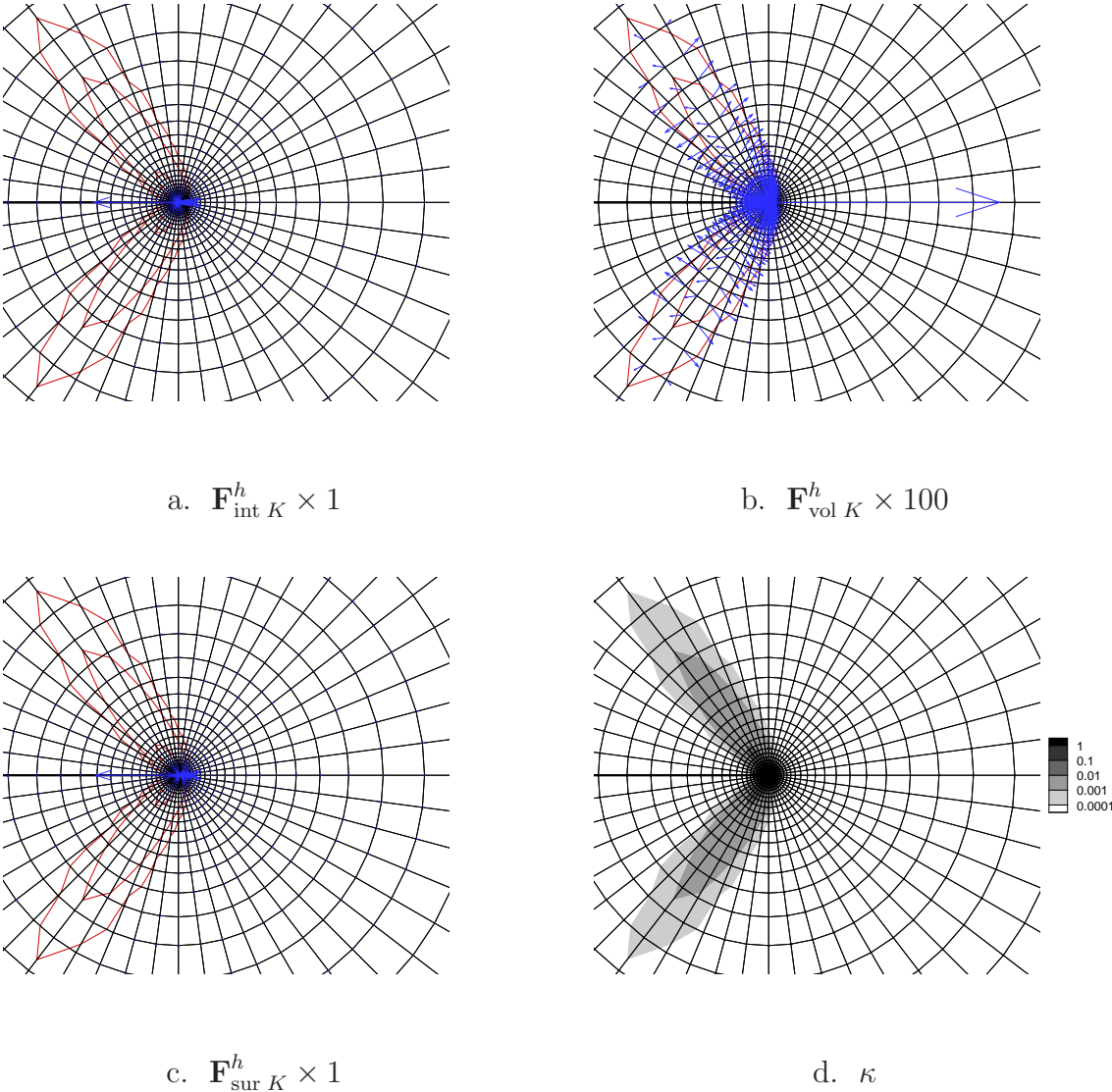
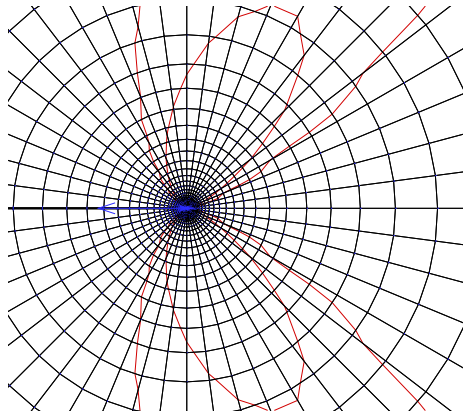
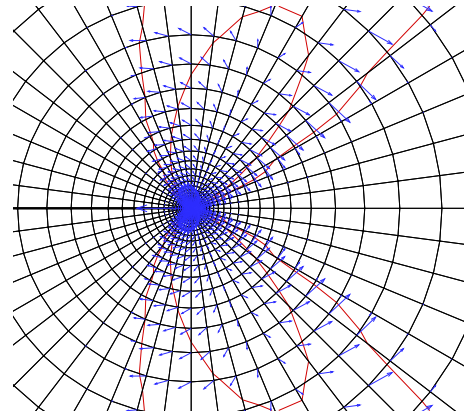
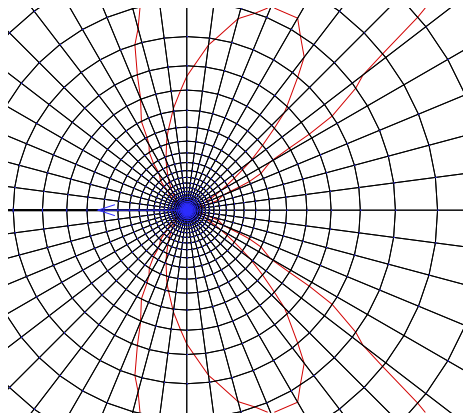
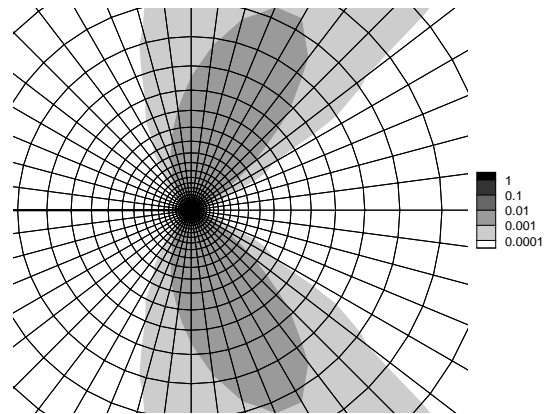


Figure 5.16. Material forces for T -stress $\tau = 0.0$ and $E/H = 100$

a. $\mathbf{F}_{\text{int } K}^h \times 1$ b. $\mathbf{F}_{\text{vol } K}^h \times 200$ c. $\mathbf{F}_{\text{sur } K}^h \times 1$ d. κ Figure 5.17. Material forces for T -stress $\tau = -0.9$ and $E/H = 2$

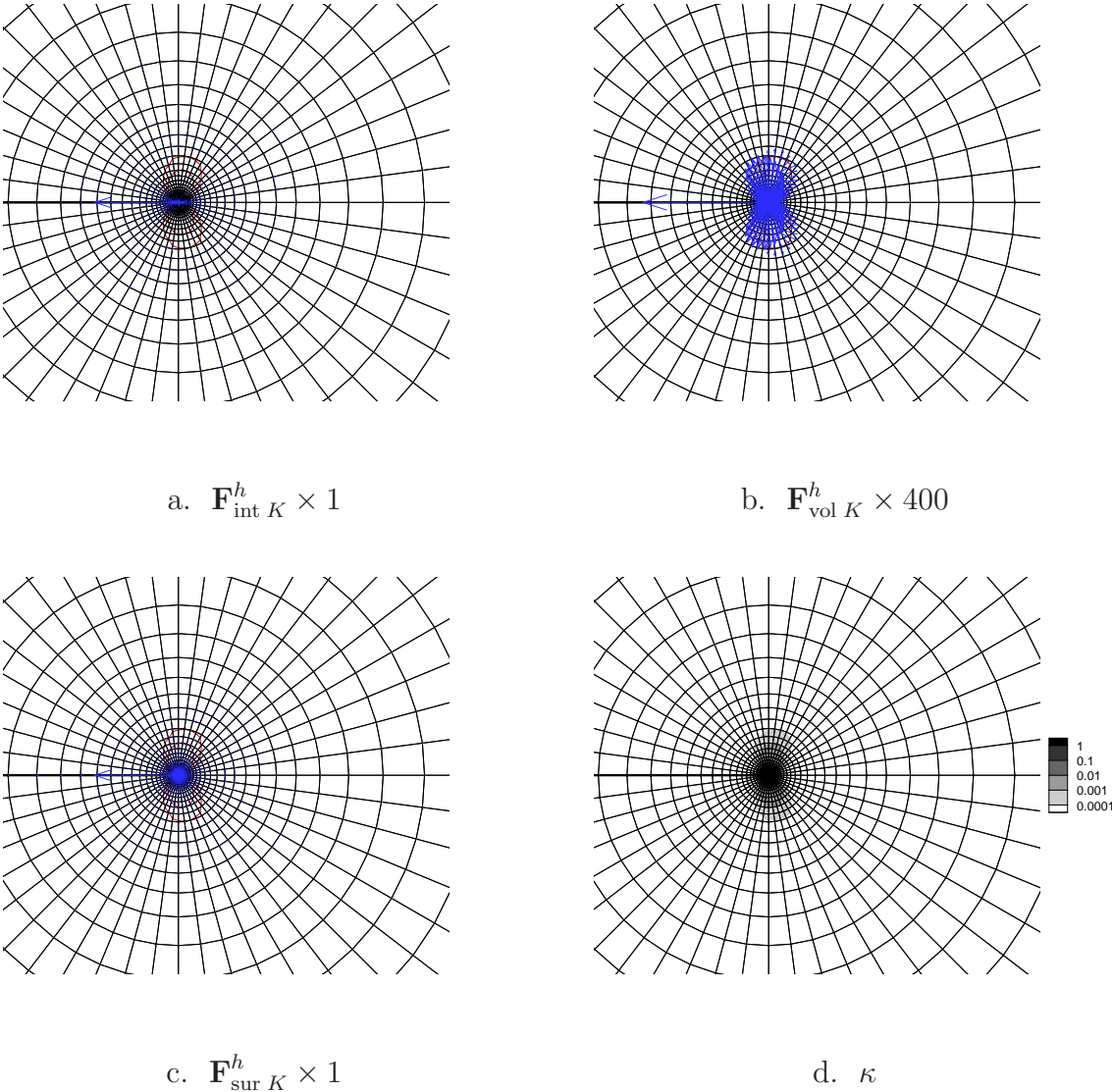
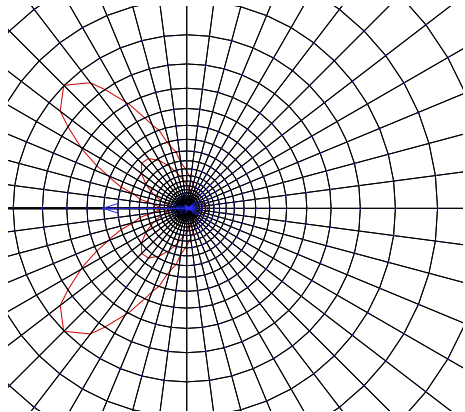
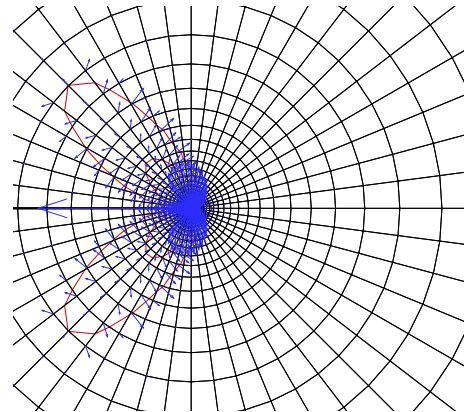
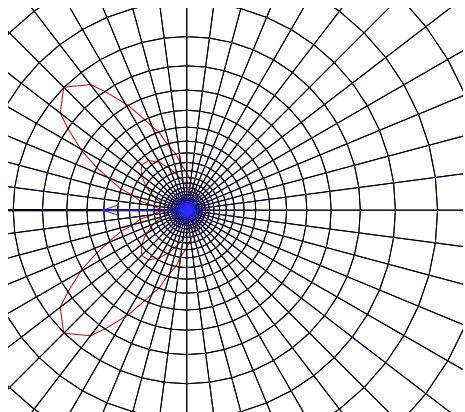
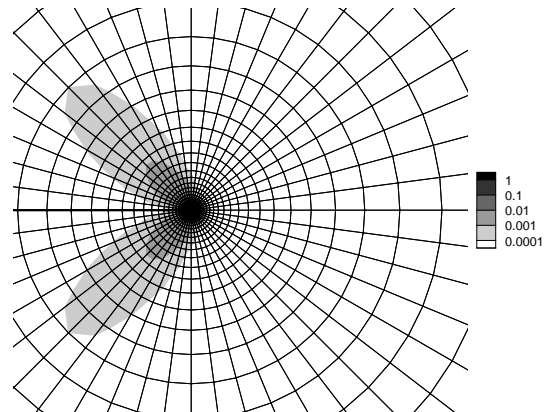


Figure 5.18. Material forces for T -stress $\tau = 0.0$ and $E/H = 2$

a. $\mathbf{F}_{\text{int}}^h K \times 1$ b. $\mathbf{F}_{\text{vol}}^h K \times 400$ c. $\mathbf{F}_{\text{sur}}^h K \times 1$ d. κ Figure 5.19. Material forces for T -stress $\tau = 0.0$ and $E/H = 2$

Chapter 6

Outlook

There are several problems which must be discussed in the future. One is the problem of calculating accurately the single material force acting at the crack tip as a driving force in the case of dissipative materials. In this case the J -integral is path-dependent and thus the single material force must be calculated by the inaccurate approximation of the stress and strain fields in the vicinity of the crack tip. The inaccurate approximation is caused by the singular behaviour of the solution at the crack tip but the type of the singularity is not known in common.

Another field of ongoing work should be the theory and numerics of material forces in the case of geometrically nonlinear hyperelasto–plasticity. The theory of geometrically nonlinear hyperelasto–plasticity is still in discussion, whereby the format of material motion balance of momentum seems fruitfully stimulate this discussion, as shown by e.g. Epstein and Maugin [23, 25, 24].

A third field should be the kinetics of defects. This could be crack propagation, phase transitions and the growth of materials whereby the material forces play the role of a driving force.

Appendix A

Notation

We denote scalar quantities by nonbold symbols c , vectors and second order tensors by bold symbols \mathbf{a} and \mathbf{b} or \mathbf{A} and \mathbf{B} . Fourth order tensors are indicated by nonserif bold fonts \mathbf{E} . In the following the frequently used calculation rules and their notations are summarized. For the sake of simplicity we only denoted the rules in cartesian coordinates.

| | | |
|-------------|--|--------------------------|
| contraction | $c = \mathbf{a} \cdot \mathbf{b}$ | $c = a_i b_i$ |
| | $\mathbf{a} = \mathbf{A} \cdot \mathbf{b}$ | $a_i = A_{ij} b_j$ |
| | $\mathbf{A} = \mathbf{B} \cdot \mathbf{C}$ | $A_{ij} = B_{ik} C_{kj}$ |

| | | |
|--------------------|--|----------------------------|
| double contraction | $c = \mathbf{A} : \mathbf{B}$ | $c = A_{ij} B_{ij}$ |
| | $\mathbf{A} = \mathbf{E} : \mathbf{B}$ | $A_{ij} = E_{ijkl} B_{kl}$ |

| | | |
|----------------|--|----------------------------|
| dyadic product | $\mathbf{A} = \mathbf{a} \otimes \mathbf{b}$ | $A_{ij} = a_i b_j$ |
| | $\mathbf{E} = \mathbf{A} \otimes \mathbf{B}$ | $E_{ijkl} = A_{ij} B_{kl}$ |

| | | |
|-----------------------------|--|----------------------------|
| nonstandard dyadic products | $\mathbf{E} = \mathbf{A} \overline{\otimes} \mathbf{B}$ | $E_{ijkl} = A_{ik} B_{jl}$ |
| | $\mathbf{E} = \mathbf{A} \underline{\otimes} \mathbf{B}$ | $E_{ijkl} = A_{il} B_{jk}$ |

The second order unit tensor \mathbf{I} is defined as $I_{ij} = \delta_{ij}$, the fourth order unit tensor \mathbf{I} is determined as $I_{ijkl} = \delta_{ij} \delta_{kl}$ and the symmetric the fourth order unit tensor \mathbf{I}^{sym} is $I_{ijkl}^{sym} = \frac{1}{2} [\delta_{ik} \delta_{jl} + \delta_{il} \delta_{jk}]$.

Appendix B

Ramberg-Osgood Material – Linearization

The implementation of the Ramberg-Osgood material law for 3d or 2d plane strain condition is epitomized in the sequel.

The 3d generalization of Eq. 2.52 is given by

$$\boldsymbol{\epsilon}^{vol} = \frac{1}{K} \boldsymbol{\sigma}^{vol} \quad (\text{A1})$$

$$\boldsymbol{\epsilon}^{dev} = \frac{1}{2G} \boldsymbol{\sigma}^{dev} + \frac{3}{2} \frac{\alpha}{E} \left[\frac{\sigma_v}{\sigma_0} \right]^{n-1} \boldsymbol{\sigma}^{dev} \quad (\text{A2})$$

where K is the bulk modulus, E is the Young's modulus and G is the shear modulus. $\boldsymbol{\epsilon}^{vol}$, $\boldsymbol{\epsilon}^{dev}$, $\boldsymbol{\sigma}^{vol}$, $\boldsymbol{\sigma}^{dev}$ are the volumetric and deviatoric strains and stresses, respectively, which are defined by

$$\begin{aligned} \boldsymbol{\epsilon}^{vol} &= \frac{1}{3} [\boldsymbol{\epsilon} : \mathbf{I}] \mathbf{I} & \boldsymbol{\sigma}^{vol} &= \frac{1}{3} [\boldsymbol{\sigma} : \mathbf{I}] \mathbf{I} \\ \boldsymbol{\epsilon}^{dev} &= \boldsymbol{\epsilon} - \boldsymbol{\epsilon}^{vol} & \boldsymbol{\sigma}^{dev} &= \boldsymbol{\sigma} - \boldsymbol{\sigma}^{vol} \end{aligned} \quad (\text{A3})$$

By introducing the equivalent von Mises stress σ_v and the equivalent deviatoric strain e_v it follows from Eq. A2

$$e_v = \frac{2}{3} \frac{1}{2G} \sigma_v + \frac{\alpha}{E} \left[\frac{\sigma_v}{\sigma_0} \right]^{n-1} \sigma_v \quad (\text{A4})$$

with

$$\begin{aligned} \sigma_v &= \sqrt{\frac{3}{2} \boldsymbol{\sigma}^{dev} : \boldsymbol{\sigma}^{dev}} \\ e_v &= \sqrt{\frac{2}{3} \boldsymbol{\epsilon}^{dev} : \boldsymbol{\epsilon}^{dev}} \end{aligned}$$

Now the von Mises stress σ_v could be solved by a standard Newton iteration from Eq. A4 and with the use of Eq. A2 the deviatoric part of the stress tensor is computable

$$\boldsymbol{\sigma}^{dev} = \frac{2\sigma_v}{3e_v} \boldsymbol{\epsilon}^{dev}. \quad (\text{A5})$$

The volumetric part of the stress tensor is obtained directly from Eq. A1. The algorithmic implementation is given in Tab. B.1

Table B.1. 3d Ramberg-Osgood material

| |
|---|
| <p>Given: strain of the actual step $m + 1$</p> ${}_{m+1}\boldsymbol{\epsilon} = {}_{m+1}\boldsymbol{\epsilon}^{dev} + {}_{m+1}\boldsymbol{\epsilon}^{vol}$ <p>Step 1: trial von Mises stress</p> ${}_{m+1}e_v = \sqrt{\frac{2}{3} {}_{m+1}\boldsymbol{\epsilon}^{dev} : {}_{m+1}\boldsymbol{\epsilon}^{dev}}$ ${}_{m+1}^{trial}\sigma_v = \begin{cases} 3G {}_{m+1}e_v & \text{if } 3G {}_{m+1}e_v \leq \sigma_0 \\ \left[\frac{\sigma_0^{n-1} E {}_{m+1}e_v}{\alpha} \right]^{1/n} & \text{if } 3G {}_{m+1}e_v > \sigma_0 \end{cases}$ <p>Step 2: Newton iteration to solve Eq. A4</p> $k = 0$ $\sigma_v^k = {}_{m+1}^{trial}\sigma_v$ $f(\sigma_v^k) = \frac{2}{3} \frac{1}{2G} \sigma_v^k + \frac{\alpha}{E} \left[\frac{\sigma_v^k}{\sigma_0} \right]^{n-1} \sigma_v^k - {}_{m+1}e_v$ <p>while ($f \geq tol$)</p> $f'(\sigma_v^k) = \frac{2}{3} \frac{1}{2G} + \frac{\alpha}{E} \frac{n}{n-1} \left[\frac{\sigma_v^k}{\sigma_0} \right]^{n-1}$ $\sigma_v^{k+1} = \sigma_v^k - f(\sigma_v^k) / f'(\sigma_v^k)$ $k \leftarrow k + 1$ $f(\sigma_v^k) = \frac{2}{3} \frac{1}{2G} \sigma_v^k + \frac{\alpha}{E} \left[\frac{\sigma_v^k}{\sigma_0} \right]^{n-1} \sigma_v^k - {}_{m+1}e_v$ <p>end</p> ${}_{m+1}\sigma_v = \sigma_v^k$ <p>Step 3: obtain stress tensor</p> ${}_{m+1}\boldsymbol{\sigma}^{dev} = \frac{2}{3} \frac{{}_{m+1}\sigma_v}{{}_{m+1}e_v} {}_{m+1}\boldsymbol{\epsilon}^{dev}$ ${}_{m+1}\boldsymbol{\sigma}^{vol} = K {}_{m+1}\boldsymbol{\epsilon}^{vol}$ ${}_{m+1}\boldsymbol{\sigma} = {}_{m+1}\boldsymbol{\sigma}^{dev} + {}_{m+1}\boldsymbol{\sigma}^{vol}$ |
|---|

For the global solution by a Newton-type algorithms, we apply a consistent linearization. With tedious but straightforward manipulations we obtain the consistent tangent moduli

as

$$\frac{\partial \boldsymbol{\sigma}^{dev}}{\partial \boldsymbol{\epsilon}^{dev}} = \frac{2\sigma_v}{3e_v} \left[\mathbf{I}^{sym} - \left[\frac{2}{3e_v^2} - \frac{2}{3e_v^2 + 3e_v \left((n-1) \alpha \frac{\sigma_v}{\sigma_0} n^{-1} \frac{\sigma_v}{E} \right)} \right] \boldsymbol{\epsilon}^{dev} \otimes \boldsymbol{\epsilon}^{dev} \right] \quad (\text{A6})$$

Appendix C

Thermo-Hyperelasticity – Linearization

The discrete coupled nonlinear system of equations of the spatial motion problem is solved in a monolithic sense with the help of an incremental iterative Newton–Raphson solution strategy. The discrete balance of momentum (3.33)₁ and the discrete balance of energy (3.33)₂ are thus solved simultaneously at time t_{n+1} . Consequently, the $k + 1$ -th iterate of the Newton iteration can be expressed as

$$\begin{aligned} \mathbf{r}_{I\ n+1}^{\varphi\ k+1} &= \mathbf{r}_{I\ n+1}^{\varphi\ k} + d\mathbf{r}_I^{\varphi} \doteq \mathbf{0} & \forall \quad I = 1, n_{np} \\ \mathbf{r}_{J\ n+1}^{\theta\ k+1} &= \mathbf{r}_{J\ n+1}^{\theta\ k} + d\mathbf{r}_J^{\theta} \doteq \mathbf{0} & \forall \quad J = 1, n_{np} \end{aligned} \quad (\text{A1})$$

whereby $d\mathbf{r}_I^{\varphi}$ and $d\mathbf{r}_J^{\theta}$ denote the iterative residua which are based on the consistent linearization of the governing equations.

$$\begin{aligned} d\mathbf{r}_I^{\varphi} &= \sum_{K=1}^{n_{np}} \mathbf{K}_{IK}^{\varphi\varphi} \cdot d\boldsymbol{\varphi}_K + \sum_{L=1}^{n_{np}} \mathbf{K}_{IL}^{\varphi\theta} d\theta_L & \forall \quad I = 1, n_{np} \\ d\mathbf{r}_J^{\theta} &= \sum_{K=1}^{n_{np}} \mathbf{K}_{JK}^{\theta\varphi} \cdot d\boldsymbol{\varphi}_K + \sum_{L=1}^{n_{np}} \mathbf{K}_{JL}^{\theta\theta} d\theta_L & \forall \quad J = 1, n_{np} \end{aligned} \quad (\text{A2})$$

They can be expressed in terms of the iteration matrices $\mathbf{K}_{IK}^{\varphi\varphi}$, $\mathbf{K}_{IL}^{\varphi\theta}$, $\mathbf{K}_{JK}^{\theta\varphi}$, $\mathbf{K}_{JL}^{\theta\theta}$, and the incremental changes of the global vector of unknowns $d\boldsymbol{\varphi}_K$ and $d\theta_L$. For the problem at hand, these iteration matrices which can be interpreted as submatrices of the global

tangential stiffness matrix take the following format.

$$\begin{aligned}
\mathbf{K}_{IK}^{\varphi\varphi} &= \frac{\partial \mathbf{r}_I^\varphi}{\partial \varphi_K} = \mathbf{A} \int_{\mathcal{B}_0}^{n_{el}} N^i \rho_0 \frac{1}{\Delta t^2} \mathbf{I} N^k + \nabla_X N^i \cdot \mathbf{D}_{\mathbf{F}} \mathbf{I} \mathbf{I}^t \cdot \nabla_X N^k \, dV \\
\mathbf{K}_{IL}^{\varphi\theta} &= \frac{\partial \mathbf{r}_I^\varphi}{\partial \theta_L} = \mathbf{A} \int_{\mathcal{B}_0}^{n_{el}} \nabla_X N^i \cdot \mathbf{D}_\theta \mathbf{I} \mathbf{I}^t N^l \, dV \\
\mathbf{K}_{JK}^{\theta\varphi} &= \frac{\partial \mathbf{r}_J^\theta}{\partial \varphi_K} = \mathbf{A} \int_{\mathcal{B}_0}^{n_{el}} -N^j \mathbf{D}_{\mathbf{F}} \mathcal{Q}_0^{mech} \cdot \nabla_X N^k \, dV \\
\mathbf{K}_{JL}^{\theta\theta} &= \frac{\partial \mathbf{r}_J^\theta}{\partial \theta_L} = \mathbf{A} \int_{\mathcal{B}_0}^{n_{el}} N^j c_0 \frac{1}{\Delta t} N^l - N^j \mathbf{D}_\theta \mathcal{Q}_0^{mech} N^l + \nabla_X N^j \cdot \mathbf{D}_{\nabla_X \theta} \mathbf{Q} \cdot \nabla_X N^l \, dV
\end{aligned} \tag{A3}$$

Therein, the first terms of equations (A3)₁ and (A3)₄ illustrate the time-dependent nature of the problem. They represent the consistent mass and capacity matrix, respectively. The second term of (A3)₁ corresponds to the classical structural stiffness. Equation (A3)₂ reflects the thermal influence in the constitutive equation. The indirect influence of the changes in temperature on the deformation field and on the temperature field introduced through the Gough–Joule effect is reflected through equation (A3)₃ and the second term in (A3)₄. The last term in equation (A3)₄ accounts for heat convection. The above introduced derivatives of the momentum flux $\mathbf{I} \mathbf{I}^t$, the thermo-mechanical coupling term \mathcal{Q}_0^{mech} and the heat flux \mathbf{Q} with respect to the deformation gradient \mathbf{F} , the temperature θ and the temperature gradient $\nabla_X \theta$ depend on the choice of the individual constitutive equations. A particular exemplification is given in chapter 3.4. The solution of the linearized system of equations (A1) finally defines the iterative update for the increments of the global unknowns φ_I and θ_J .

$$\begin{aligned}
\Delta \varphi_I &= \Delta \varphi_I + d\varphi_I & \forall \quad I = 1, n_{np} \\
\Delta \theta_J &= \Delta \theta_J + d\theta_J & \forall \quad J = 1, n_{np}
\end{aligned} \tag{A4}$$

Remark: Transient terms in the linearized residual

Recall, that when considering the balance of momentum in the quasi-static sense, the term $N^I \rho_0 / \Delta t^2 \mathbf{I} N^K$ of equation (A3)₁ vanishes identically.

Appendix D

Single Crystal Plasticity – Numerical Solution Strategies

For convenience of the reader we briefly reiterate the applied discretization scheme in time and space in the sequel (with emphasis on a single-slip setting). The time interval of interest is thereby partitioned into finite subintervals, $T = \cup_{n=0}^N [t_n, t_{n+1}]$ with $\Delta t = t_{n+1} - t_n > 0$ being obvious, and the spatial domain is represented via an element wise discretization $\mathcal{B} = \cup_{e=1}^{n_{el}} \mathcal{B}^e$ within a standard finite element context.

D.1 Node point based approach

By carrying out the discretization in time we derive the algorithmic version of the weak forms and the decomposition into elastic and plastic domains as highlighted in eqs.(5.38–5.42)

$$G_{n+1}^u = \int_{\partial \mathcal{B}^t} \delta \mathbf{u} \cdot \mathbf{t}_{n+1}^{\text{pr}} \, da + \int_{\mathcal{B}} \delta \mathbf{u} \cdot \mathbf{b}_{n+1} - \nabla \delta \mathbf{u} : \boldsymbol{\sigma}_{n+1} \, dv = 0 \quad (\text{A1})$$

$$G_{n+1}^{\Phi} = \int_{\mathcal{B}} \delta \kappa [|\tau_{n+1}| - Y_0 - h_{n+1}] \, dv \leq 0 \quad (\text{A2})$$

$$\Delta G_{n+1}^{\kappa} = \int_{\mathcal{B}} \delta \Phi [\kappa_{n+1} - \kappa_n] \, dv \geq 0 \quad (\text{A3})$$

$$\mathcal{B}_{n+1}^e = \{ \mathbf{x} \in \mathcal{B} \mid G_{n+1}^{\Phi} \leq 0, \Delta G_{n+1}^{\kappa} = 0 \} \quad (\text{A4})$$

$$\mathcal{B}_{n+1}^p = \{ \mathbf{x} \in \mathcal{B} \mid G_{n+1}^{\Phi} = 0, \Delta G_{n+1}^{\kappa} > 0 \} \quad (\text{A5})$$

whereby the approximation $\dot{\kappa} \doteq [\kappa_{n+1} - \kappa_n]/\Delta t$ has been applied. Please note that eqs.(A4,A5) take the interpretation as the pointwise algorithmic format of the Kuhn–Tucker condition in eq.(5.34)₃, namely $[\kappa_{n+1} - \kappa_n] \Phi_{n+1} = 0$ (with $\Delta t > 0$).

Concerning the spatial discretization of \mathbf{u} and κ , we introduce the finite element domain

via

$$\mathbb{B} = \bigcup_{e=1}^{n_{\text{el}}} \mathbb{B}^e \quad \mathbb{B}^e = \{k \mid k = 1, \dots, n_{\text{en}}\} \quad \mathbb{B} = \{K \mid K = 1, \dots, n_{\text{np}}\} \quad (\text{A6})$$

such that k and K represent nodes on the element – and global level, respectively. In analogy to eqs.(A1–A5) one obtains the residua and domain decomposition as follows

$$\mathbf{R}_K^u = \mathbf{A}_{e=1}^{n_{\text{el}}} \int_{\partial \mathbb{B}^e \cap \partial \mathbb{B}^t} N_u^k \mathbf{t}_{n+1}^{\text{pr}} \, da + \int_{\mathbb{B}^e} N_u^k \mathbf{b}_{n+1} - \nabla N_u^k \cdot \boldsymbol{\sigma}_{n+1} \, dv = \mathbf{0} \quad (\text{A7})$$

$$R_K^\Phi = \mathbf{A}_{e=1}^{n_{\text{el}}} \int_{\mathbb{B}^e} N_\kappa^k [|\tau_{n+1}| - Y_0 - h_{n+1}] \, dv \leq 0 \quad (\text{A8})$$

$$\Delta R_K^\kappa = \mathbf{A}_{e=1}^{n_{\text{el}}} \int_{\mathbb{B}^e} N_\kappa^k [\kappa_{n+1}^h - \kappa_n^h] \, dv \geq 0 \quad (\text{A9})$$

$$\mathbb{B}_{n+1}^e = \{K \in \mathbb{B} \mid R_K^\Phi \leq 0, \Delta R_K^\kappa = 0\} \quad (\text{A10})$$

$$\mathbb{B}_{n+1}^p = \{K \in \mathbb{B} \mid R_K^\Phi = 0, \Delta R_K^\kappa > 0\} \quad (\text{A11})$$

whereby the displacement field (as well as the nodal positions) is approximated via N_u^k while the shape functions N_κ^k are applied to the hardening variable and $\delta\Phi$, respectively. The discrete algorithmic format of eq.(5.34)₃ is thereby represented via $\Delta R_K^\kappa R_K^\Phi = 0$. Now, standard incremental iteration schemes can be applied to solve the underlying system of nonlinear equations. Placing emphasis on a typical Newton algorithm we obtain the linearized residua as

$$\begin{aligned} -d\mathbf{R}_K^u &= \sum_{L \in \mathbb{B}} \left[\mathbf{A}_{e=1}^{n_{\text{el}}} \int_{\mathbb{B}^e} \nabla N_u^k \cdot \partial_{\boldsymbol{\varepsilon}_{n+1}} \boldsymbol{\sigma}_{n+1} \cdot \nabla N_u^l \, dv \right] \cdot d\mathbf{u}_L \\ &+ \sum_{L \in \mathbb{B}_{\text{act}}} \left[\mathbf{A}_{e=1}^{n_{\text{el}}} \int_{\mathbb{B}^e} \nabla N_u^k \cdot \partial_{\kappa_{n+1}} \boldsymbol{\sigma}_{n+1} N_\kappa^l \, dv \right] \cdot d\kappa_L \quad \forall K \in \mathbb{B} \end{aligned} \quad (\text{A12})$$

$$\begin{aligned} -dR_K^\Phi &= \sum_{L \in \mathbb{B}} \left[\mathbf{A}_{e=1}^{n_{\text{el}}} \int_{\mathbb{B}^e} N_\kappa^k \partial_{\boldsymbol{\varepsilon}_{n+1}} |\tau_{n+1}| \cdot \nabla N_u^l \, dv \right] \cdot d\mathbf{u}_L \\ &+ \sum_{L \in \mathbb{B}_{\text{act}}} \left[\mathbf{A}_{e=1}^{n_{\text{el}}} \int_{\mathbb{B}^e} N_\kappa^k \partial_{\kappa_{n+1}} [|\tau_{n+1}| - h_{n+1}] N_\kappa^l \, dv \right] \cdot d\kappa_L \quad \forall K \in \mathbb{B}_{\text{act}} \end{aligned} \quad (\text{A13})$$

and the incorporated derivatives take the following format for the problem at hand

$$\partial_{\boldsymbol{\varepsilon}_{n+1}} \boldsymbol{\sigma}_{n+1} = L \mathbf{i} \otimes \mathbf{i} + 2G \mathbf{i}^{\text{sym}} \quad \partial_{\kappa_{n+1}} \boldsymbol{\sigma}_{n+1} = -2G \text{sign}(\tau_{n+1}) \boldsymbol{\nu} \quad (\text{A14})$$

$$\partial_{\boldsymbol{\varepsilon}_{n+1}} |\tau_{n+1}| = 2G \text{sign}(\tau_{n+1}) \boldsymbol{\nu} \quad \partial_{\kappa_{n+1}} [|\tau_{n+1}| - h_{n+1}] = -G - H \quad (\text{A15})$$

with $\boldsymbol{\nu} = [\mathbf{s} \otimes \mathbf{m}]^{\text{sym}}$ and \mathbf{i}^{sym} denoting the fourth order symmetric identity; see also the following section D.2 where the underlying Euler backward integration is highlighted.

Please note that the obtained system of equations turns out to be symmetric if the residual R_K^Φ or rather eqs.(A8,A13,A15) is scaled by the factor -1 which moreover results in a positive definite element stiffness matrix (this change of sign is therefore adopted for the implementation of the developed formulation). Finally, eqs.(A14,A15) turn out to be independent of the sign of \mathbf{s} and \mathbf{m} , moreover, recall that the contributions in eqs.(A14,A15)₁ do not incorporate any (implicit) derivatives due to the Lagrange multiplier or rather the hardening variable since eqs.(A14,A15)₂ account for the calculation of this field.

D.2 Integration point based approach

The implementation of the integration point based approach is rather straightforward: Based on the evolution equation $\dot{\boldsymbol{\varepsilon}}^p = \dot{\lambda} \text{sign}(\tau) \boldsymbol{\nu}$, with $\boldsymbol{\nu} = [\mathbf{s} \otimes \mathbf{m}]^{\text{sym}}$, $\mathbf{s} \cdot \boldsymbol{\nu} \cdot \mathbf{m} = \frac{1}{2}$ and $\boldsymbol{\nu} : \mathbf{i} = 0$ since $\mathbf{s} \perp \mathbf{m}$, we obtain by application of the implicit Euler backward scheme

$$\boldsymbol{\varepsilon}_{n+1}^e = \boldsymbol{\varepsilon}^{\text{tri}} - \Delta\lambda \text{sign}(\tau_{n+1}) \boldsymbol{\nu} \quad \text{and} \quad \kappa_{n+1} = \kappa_n + \Delta\lambda \quad (\text{A16})$$

with $\boldsymbol{\varepsilon}^{\text{tri}} = \boldsymbol{\varepsilon}_{n+1} - \boldsymbol{\varepsilon}_n^p$, $\tau_{n+1} = \mathbf{s} \cdot \boldsymbol{\sigma}_{n+1} \cdot \mathbf{m}$ as well as $\Delta\lambda = \Delta t \dot{\lambda}$. Following standard concepts in computational inelasticity, the actual stress state reads $\boldsymbol{\sigma}_{n+1} = \boldsymbol{\sigma}^{\text{tri}} - 2G \Delta\lambda \text{sign}(\tau_{n+1}) \boldsymbol{\nu}$, compare eq.(5.47), and allows the Schmid stress to be represented as

$$\tau_{n+1} = \tau^{\text{tri}} - G \Delta\lambda \text{sign}(\tau_{n+1}) \quad (\text{A17})$$

$$\text{sign}(\tau_{n+1}) |\tau_{n+1}| = \text{sign}(\tau^{\text{tri}}) |\tau^{\text{tri}}| - G \Delta\lambda \text{sign}(\tau_{n+1}) \quad (\text{A18})$$

with $\tau^{\text{tri}} = \mathbf{s} \cdot \boldsymbol{\sigma}^{\text{tri}} \cdot \mathbf{m}$ being obvious. Based on this relation, we consequently observe from $G \Delta\lambda > 0$ that

$$\text{sign}(\tau_{n+1}) = \text{sign}(\tau^{\text{tri}}) \quad |\tau_{n+1}| = |\tau^{\text{tri}}| - G \Delta\lambda \quad (\text{A19})$$

holds throughout such that the slip parameters allow to be updated via

$$\gamma_{n+1} = \gamma_n + \text{sign}(\tau_{n+1}) \Delta\lambda = \gamma_n + \text{sign}(\tau^{\text{tri}}) \Delta\lambda \quad (\text{A20})$$

and the yield function takes the format

$$\Phi_{n+1} = |\tau^{\text{tri}}| - G \Delta\lambda - [Y_0 + H \kappa_n + H \Delta\lambda] \doteq \Phi^{\text{tri}} - \Delta\lambda [G + H]. \quad (\text{A21})$$

In case that the trial yield function is violated, $\Phi^{\text{tri}} > 0$, the Lagrange multiplier is determined via $\Delta\lambda = [G + H]^{-1} \Phi^{\text{tri}}$ in order to satisfy $\Phi_{n+1} = 0$. Finally, the computation of the (symmetric) algorithmic tangent operator results in

$$\mathbf{e}_{n+1}^{\text{alg}} = \partial_{\boldsymbol{\varepsilon}_{n+1}} \boldsymbol{\sigma}_{n+1} = L \mathbf{i} \otimes \mathbf{i} + 2G \mathbf{i}^{\text{sym}} - 4G^2 [G + H]^{-1} \boldsymbol{\nu} \otimes \boldsymbol{\nu} \quad (\text{A22})$$

and apparently assembles the contributions in eqs.(A14,A15).

Bibliography

- [1] A. Acharya and J.L. Bassani. Lattice incompatibility and the gradient theory of crystal plasticity. *J. Mech. Phys. Solids*, 48(8):1565–1595, 2000.
- [2] M. Adda-Bedia. Path prediction of kinked and branched cracks in plane situations. *Physical Review Letters*, 93:185502, 2004.
- [3] M. Amestoy and J. B. Leblond. Crack path in plane situations-ii. detailed form of the expansion of the stress intensity factors. *International Journal of Solids and Structures*, 29:465–501, 1992.
- [4] K.-H. Anthony and A. Azirhi. Dislocation dynamics by means of Lagrange formalism for irreversible processes – complex fields and deformation processes. *Int. J. Engng. Sci.*, 33(15):2137–2148, 1995.
- [5] F. Armero and J. C. Simo. A new unconditionally stable fractional step method for non-linear coupled thermo-mechanical problems. *International Journal for Numerical Methods in Engineering*, 35:737–766, 1992.
- [6] R. Asaro. Crystal plasticity. *ASME J. Appl. Mech.*, 50:921–934, 1983.
- [7] H. Askes, E. Kuhl, and P. Steinmann. An ale formulation based on spatial and material settings of continuum mechanics. part 2: Classification and applications. *Computer Methods in Applied Mechanics and Engineering*, 193:4223–4245, 2004.
- [8] R. S. Barsoum. Triangular quarter-point elements as elastic and perfectly-plastic crack tip elements. *International Journal for Numerical Methods in Engineering*, 11:85–98, 1977.
- [9] M.S. Bazaraa, H.D. Sherali, and C.M. Shetty. *Nonlinear Programming: Theory and Application*. Wiley–Interscience Series in Discrete Mathematics and Optimization. Wiley, 2nd edition, 1979.
- [10] D.P. Bertsekas. *Constrained Optimization and Lagrange Multiplier Methods*, volume 4 of *Athena Scientific Optimization and Computation Series*. Athena Scientific, 1996.
- [11] J.F. Besseling and E. van der Giessen. *Mathematical Modelling of Inelastic Deformation*, volume 5 of *Applied Mathematics and Mathematical Computations*. Chapman & Hall, 1994.

-
- [12] M. Braun. Configurational forces induced by finite-element discretization. *Proceedings of the Estonian Academy of Science. Physics, Mathematics*, 46(1/2):24–31, 1997.
- [13] P. Cermelli and M.E. Gurtin. On the characterization of geometrically necessary dislocations in finite plasticity. *J. Mech. Phys. Solids*, 49(7):1539–1568, 2001.
- [14] P. Cermelli and M.E. Gurtin. Geometrically necessary dislocations in viscoplasticity single crystals and bicrystals undergoing small deformations. *Int. J. Solids Struct.*, 39(7):6281–6309, 2002.
- [15] P. Chadwick. Applications of an energy-momentum tensor in non-linear elastostatics. *Journal of Elasticity*, 5:249–258, 1975.
- [16] G. P. Cherepanov. Crack propagation in continuous media. *Journal of Applied Mathematics and Mechanics*, 31:503–512, 1967.
- [17] S. Cleja-Tigou and G. A. Maugin. Eshelby’s stress tensor in finite elastoplasticity. *Acta Mechanica*, 139:231–249, 2000.
- [18] B.D. Coleman and W. Noll. The thermodynamics of elastic materials with heat conduction and viscosity. *Arch. Rational Mech. Anal.*, 13:167–178, 1963.
- [19] B. Cotterell and J.R. Rice. Slightly curved or kinked cracks. *International Journal of Fracture*, 16:155–169, 1980.
- [20] A.M. Cuitiño and M. Ortiz. Computational modelling of single crystals. *Modelling Simul. Mat. Sci. Engng.*, 1:225–263, 1992.
- [21] C. Davini. Some remarks on the continuum theory of defects. *Int. J. Solids Struct.*, 38:1169–1182, 2001.
- [22] R. Denzer, F. J. Barth, and P. Steinmann. Studies in elastic fracture mechanics based on the material force method. *International journal for numerical methods in engineering*, 58:1817–1835, 2003.
- [23] M. Epstein and G. A. Maugin. The energy-momentum tensor and material uniformity in finite elasticity. *Acta Mechanica*, 83:127–133, 1990.
- [24] M. Epstein and G. A. Maugin. Geometric material structure of finite-strain elasticity and anelasticity. *Zeitschrift für angewandte Mathematik und Mechanik*, 76(S4):125–128, 1996.
- [25] M. Epstein and G. A. Maugin. On the geometrical material structure of anelasticity. *Acta Mechanica*, 115:119–131, 1996.
- [26] J. L. Ericksen. On nonlinear elasticity theory for crystal defects. *International Journal of Plasticity*, 14:9–24, 1998.

-
- [27] J. D. Eshelby. The force on an elastic singularity. *Philosophical transactions of the Royal Society of London A*, 244:87–112, 1951.
- [28] J. D. Eshelby. The determination of the elastic field of an ellipsoidal inclusion and related problems. *Royal Society Burlington House London*, 241:376–397, 1957.
- [29] J. D. Eshelby. The elastic energy-momentum tensor. *Journal of Elasticity*, 5:321–335, 1975.
- [30] J. Florez-Lopez, A. Benallal, G. Geymonat, and R. Billardon. A two-field finite element formulation for elasticity coupled to damage. *Computer Methods in Applied Mechanics and Engeneering*, 114:193–212, 1994.
- [31] D. Gross and Th. Seelig. *Bruchmechanik: mit einer Einführung in die Mikromechanik*. Springer Verlag, 2001.
- [32] M. E. Gurtin. *Configurational Forces as Basic Concepts of Continuum Physics*. Springer Verlag, 2000.
- [33] M. E. Gurtin and P. Podio-Guidugli. Configurational forces and a constitutive theory for crack propagation that allows for kinking and curving. *Journal of the Mechanics and Physics of Solids*, 46(8):1343–1378, 1998.
- [34] B. Halphen and Q. S. Nguyen. Sur les matériaux standards généralisés. *Journal de Mécanique*, 14:39–95, 1975.
- [35] P. Haupt. *Continuum Mechanics and Theory of Materials*. Advanced Texts in Physics. Springer, 2000.
- [36] J. W. Hutchinson. Plastic stress and strain fields at a crack tip. *Journal of the Mechanics and Physics of Solids*, 16:337–347, 1968.
- [37] A. Ibrahimbebovic, L. Chorfi, and F. Gharzeddine. Thermomechanical coupling at finite elastic strain: covariant formulation and numerical implementation. *Commun. Num. Methods Engrg.*, 17:275–289, 2001.
- [38] R. Kienzler and G. Herrmann. *Mechanics in Material Space with Application to Defect and Fracture Mechanics*. Springer Verlag, 2000.
- [39] S. Kolling, H. Baaser, and D. Gross. Material forces due to crack–inclusion interaction. *International Journal of Fracture*, 118:229–238, 2002.
- [40] A.M. Kosevich. Crystal dislocations and the theory of elasticity. In F.R.N. Nabarro, editor, *Dislocations in Solids (The Elastic Theory)*, volume 1, pages 33–141. North–Holland Publishing Company, 1979.
- [41] E. Kröner. Allgemeine Kontinuumstheorie der Versetzungen und Eigenspannungen. *Arch. Rational Mech. Anal.*, 4:273–334, 1960.

-
- [42] E. Kuhl, H. Askes, and P. Steinmann. An ale formulation based on spatial and material settings of continuum mechanics. part 1: Generic hyperelastic formulation. *Computer Methods in Applied Mechanics and Engineering*, 193:4207–4222, 2004.
- [43] E. Kuhl, R. Denzer, F. J. Barth, and P. Steinmann. Application of the material force method to thermo-hyperelasticity. *Computer Methods in Applied Mechanics and Engineering*, 193:3303–3325, 2004.
- [44] E. Kuhl, A. Menzel, and P. Steinmann. Computational modeling of growth – A critical review, a classification of concepts and two new consistent approaches. *Comput. Mech.*, 2003. accepted for publication.
- [45] E. Kuhl and P. Steinmann. On spatial and material settings of thermo-hyperelastodynamics for open systems. *Acta Mechanica*, 160:179–217, 2003.
- [46] E. Kuhl and P. Steinmann. Material forces in open system mechanics. *Computer Methods in Applied Mechanics and Engineering*, 32:2357–2381, 2004.
- [47] J. B. Leblond. Crack path in plane situations-i. general form of the expansion of the stress intensity factors. *International Journal of Solids and Structures*, 25(11):1311–1325, 1989.
- [48] F. Z. Li, C. F. Shih, and A. Needleman. A comparison of methods for calculating energy release rates. *Engineering Fracture Mechanics*, 21(2):405–421, 1985.
- [49] T. Liebe, R. Denzer, and P. Steinmann. Application of the material force method to isotropic continuum damage. *Computational Mechanics*, 30:171–184, 2003.
- [50] T. Liebe, A. Menzel, and P. Steinmann. Theory and numerics of a thermodynamically consistent framework for geometrically non-linear gradient plasticity. *Int. J. Engng. Sci.*, 41:1603–1629, 2003.
- [51] T. Liebe and P. Steinmann. Theory and numerics of a thermodynamically consistent framework for geometrically linear gradient plasticity. *International Journal for Numerical Methods in Engineering*, 51:1437–1467, 2001.
- [52] T. Liebe, P. Steinmann, and A. Benallal. Theoretical and computational aspects of a thermodynamically consistent framework for geometrically linear gradient damage. *Computer Methods in Applied Mechanics and Engineering*, 190:6555–6576, 2001.
- [53] I.-S. Liu. *Continuum Mechanics*. Advanced Texts in Physics. Springer, 2002.
- [54] D. Luenberger. *Introduction to linear and nonlinear programming*. Addison-Wesley Pub., 1973.
- [55] D.G. Luenberger. *Nonlinear Programming*. Addison–Wesley, 2nd edition, 1984.
- [56] G. A. Maugin. *Material Inhomogeneities in Elasticity*. Chapman&Hall, 1993.

-
- [57] G. A. Maugin. Eshelby stress in elastoplasticity and ductile fracture. *International Journal of Plasticity*, 10(4):393–408, 1994.
- [58] G. A. Maugin. Material forces: Concepts and applications. *Applied Mechanics Reviews*, 48:213–245, 1995.
- [59] G. A. Maugin. Canonical momentum and energy in elastic systems with additional state variables. *C. R. Acad. Sci. Paris*, 323IIb:407–412, 1996.
- [60] G. A. Maugin. Thermomechanics of inhomogeneous-heterogeneous systems: Application to the irreversible progress of two- and three-dimensional defects. *ARI*, 50:41–56, 1997.
- [61] G.A. Maugin. *The Thermodynamics of Nonlinear Irreversible Behaviors*, volume 27 of *World Scientific Series on Nonlinear Science: Series A*. World Scientific Publishing, 1999.
- [62] G.A. Maugin. On the universality of thermomechanics of forces driving singular sets. *Archive of Applied Mechanics*, 70:31–45, 2000.
- [63] A. Menzel, R. Denzer, and P. Steinmann. On the comparison of two approaches to compute material forces for inelastic materials. application to single-slip crystal plasticity. *Computer Methods in Applied Mechanics and Engineering*, 193:5411–5428, 2004.
- [64] A. Menzel and P. Steinmann. On the continuum formulation of higher gradient plasticity for single and polycrystals. *J. Mech. Phys. Solids*, 48(8):1777–1796, 2000. Erratum 49(5):1179–1180, 2001.
- [65] C. Miehe. Zur numerischen behandlung thermomechanischer prozesse. *Dissertation, Institut für Baumechanik und Numerische Mechanik, Universität Hannover, Bericht-Nr. 88/6*, 1988.
- [66] C. Miehe. Kanonische modelle multiplikativer elasto-plastizität–thermodynamische formulierung und numerische implementierung. *Habilitationsschrift, Institut für Baumechanik und Numerische Mechanik, Universität Hannover, Bericht-Nr. 93/1*, 1993.
- [67] C. Miehe. Discontinuous and continuous damage evolution in Ogden–type large–strain elastic materials. *Euro. J. Mech. A/Solids*, 14(5):697–720, 1995.
- [68] C. Miehe. Entropic thermoelasticity at finite strains. aspects of the formulation and numerical implementation. *Computer Methods in Applied Mechanics and Engineering*, 120:243–269, 1995.
- [69] C. Miehe. Exponential map algorithm for stress updates in anisotropic multiplicative elastoplasticity for single crystals. *Int. J. Numer. Methods Engng.*, 39:3367–3390, 1996.

- [70] C. Miehe. Multisurface thermoplasticity for single crystals at large strains in terms of Eulerian vector updates. *Int. J. Solids Struct.*, 33(20–22):3103–3130, 1996.
- [71] C. Miehe and J. Schröder. A comparative study of stress update algorithms for rate-independent and rate-dependent crystal plasticity. *Int. J. Numer. Methods Engng.*, 50:273–298, 2001.
- [72] R. Müller, S. Kolling, and D. Gross. On configurational forces in the context of the finite element method. *International Journal of Numerical Methods in Engineering*, 53:1557–1574, 2002.
- [73] R. Müller and G. A. Maugin. On material forces and finite element discretization. *Computational Mechanics*, 29:52–60, 2002.
- [74] J. T. Oden. *Finite Elements of Nonlinear Continua*. McGraw-Hill, 1972.
- [75] R. Phillips. *Crystals, Defects and Microstructures – Modeling Across Scales*. Cambridge University Press, 2001.
- [76] P. M. Pinsky. A finite element formulation for elastoplasticity based on a three-field variational equation. *Computer Methods in Applied Mechanics and Engineering*, 61:41–60, 1986.
- [77] S. Reese. Thermomechanische modellierung gummiartiger polymerstrukturen. *Habilitationsschrift, Institut für Baumechanik und Numerische Mechanik, Universität Hannover, Bericht-Nr. F01/4*, 2001.
- [78] S. Reese and S. Govindjee. Theoretical and numerical aspects in the thermo-viscoelastic material behavior of rubber-like polymers. *Mech. Time-dependent Mater.*, 1:357–396, 1998.
- [79] S. Reese and P. Wriggers. Thermo-viscoelastic material behaviour at finite deformations with temperatur-dependent material parameters. *Zeitschrift für angewandte Mathematik und Mechanik*, 78:S157–S160, 1998.
- [80] J. R. Rice. A path independent integral and the approximate analysis of strain concentration by notches and cracks. *Journal of Applied Mechanics*, 35:379–386, 1968.
- [81] J. R. Rice. Limitations to the small scale yielding approximation for crack tip plasticity. *Journal of the Mechanics and Physics of Solids*, 22:17–26, 1974.
- [82] J. R. Rice and G. F. Rosengren. Plane strain deformation near a crack tip in a power-law hardening material. *Journal of the Mechanics and Physics of Solids*, 16:1–16, 1968.
- [83] H.-A. Richard. *Bruchvorhersagen bei überlagerter Normal- und Schubbeanspruchung von Rissen*. VDI Forschungsheft 631/1985. VDI-Verlag, Düsseldorf, 1985.

- [84] R. T. Shield. Inverse deformation results in finite elasticity. *ZAMP*, 18:490–500, 1967.
- [85] C. F. Shih, B. Moran, and T. Nakamura. Energy release rate along a three-dimensional front in a thermally stressed body. *International Journal of Fracture*, 30:79–102, 1986.
- [86] C. F. Shih and A. Needleman. Fully plastic crack problems. part 1: Solution by a penalty method. *Journal of Applied Mechanics*, 51:48–56, 1984.
- [87] C. F. Shih and A. Needleman. Fully plastic crack problems. part 2: Application of consistency checks. *Journal of Applied Mechanics*, 51:57–64, 1984.
- [88] M. Šilhavý. *The Mechanics and Thermomechanics of Continuous Media*. Texts and Monographs in Physics. Springer, 1997.
- [89] C. Simo, J. G. Kennedy, and R. L. Raylor. Complementary mixed finite element formulations for elastoplasticity. *Computer Methods in Applied Mechanics and Engineering*, 74:177–206, 1989.
- [90] J. C. Simo and J. Ju. Strain- and stress-based continuum damage models: I. formulation. *International Journal of Solids and Structures*, 23:821–840, 1987.
- [91] J.C. Simo. Numerical analysis and simulation of plasticity. In P.G. Ciarlet and J.L. Lions, editors, *Numerical Methods for Solids (Part 3)*, volume VI of *Handbook of Numerical Analysis*, pages 183–499. North-Holland, 1998.
- [92] J.C. Simo and C. Miehe. Associated coupled thermoplasticity at finite strains: Formulation, numerical analysis and implementation. *Comput. Methods Appl. Mech. Engrg.*, 98:41–104, 1992.
- [93] P. Steinmann. Views on multiplicative elastoplasticity and the continuum theory of dislocations. *Int. J. Engng. Sci.*, 34(15):1717–1735, 1996.
- [94] P. Steinmann. Application of material forces to hyperelastostatic fracture mechanics. i. continuum mechanical setting. *International Journal of Solids and Structures*, 37:7371–7391, 2000.
- [95] P. Steinmann. A view on the theory and computation of hyperelastic defect mechanics. In *Proceedings of the European Conference on Computational Mechanics (ECCM)*, Cracow, Poland, 2001.
- [96] P. Steinmann. On spatial and material setting of hyperelastodynamics. *Acta Mechanica*, 156:193–218, 2002.
- [97] P. Steinmann. On spatial and material setting of thermo-hyperelastodynamics. *Journal of Elasticity*, 66:109–157, 2002.
- [98] P. Steinmann. On spatial and material settings of hyperelastostatic crystal defects. *Journal of the Mechanics and Physics of Solids*, 50:1743–1766, 2002.

-
- [99] P. Steinmann, D. Ackermann, and F. J. Barth. Application of material forces to hyperelastostatic fracture mechanics. ii. computational setting. *International Journal of Solids and Structures*, 38:5509–5526, 2001.
- [100] P. Steinmann and E. Stein. On the numerical treatment and analysis of finite deformation ductile single crystal plasticity. *Comput. Methods Appl. Mech. Engrg.*, 129:235–254, 1996.
- [101] T. Svedberg. *On the Modelling and Numerics of Gradient-Regularized Plasticity Coupled to Damage*. PhD thesis, Chalmers University of Technology, Department of Solid Mechanics, Göteborg, Sweden, 1999.
- [102] B. Svendsen. Continuum thermodynamic models for crystal plasticity including the effects of geometrically-necessary dislocations. *J. Mech. Phys. Solids*, 50(6):1297–1330, 2002.
- [103] D. M. Tracy. Finite element solutions for crack tip behaviour in small-scale yielding. *Journal of Engineering Materials and Technology*, 98:146–151, 1976.
- [104] C. Trimarco and G. A. Maugin. Pseudomomentum and material forces in nonlinear elasticity: Variational formulations and application to brittle fracture. *Acta Mechanica*, 94:1–28, 1992.
- [105] C. Truesdell and W. Noll. *The Non-Linear Field Theories of Mechanics*. Springer, 2nd edition, 1992.
- [106] C. Truesdell and R.A. Toupin. The classical field theories. In S. Flügge, editor, *Encyclopedia of Physics*, volume III/1, pages 226–793. Springer, 1960.
- [107] S. Vidoli and G. Sciarra. A model for crystal plasticity based on micro-slip descriptors. *Continuum Mech. Thermodyn.*, 14:425–435, 2002.
- [108] M. L. Williams. On the stress distribution at the base of a stationary crack. *Journal of Applied Mechanics*, 24:109–114, 1957.
- [109] O.C. Zienkiewicz and R.L. Taylor. *The Finite Element Method*, volume 1, The Basics. Butterworth-Heinemann, 5th edition, 2000.

Lebenslauf

Name: Ralf Philipp Denzer
Geburtsdatum: 09.06.1967
Geburtsort: Kaiserslautern
Anschrift: 67663 Kaiserslautern, Erfurter Straße 93
Familienstand: ledig

Schulbildung: 1973-1977 Grundschule Olsbrücken
1977-1986 Albert-Schweitzer-Gymnasium, Kaiserslautern
1986 Hochschulreife

Hochschulbildung: 1987-1994 Studium Maschinenbau, TU Kaiserslautern
1994 Diplom, Maschinenbau, TU Kaiserslautern,
Vertiefungsrichtung *Theoretische Grundlagen*
1994-2000 Wissenschaftlicher Mitarbeiter,
Institut für Verbundwerkstoffe GmbH,
TU Kaiserslautern
seit 2001 Wissenschaftlicher Mitarbeiter,
Lehrstuhl für Technische Mechanik,
TU Kaiserslautern

Grundwehrdienst: 1986-1987 Weingarten und Philippsburg